12-12-2022

Initial data generation and dynamical simulations of binary neutron star systems

Tanmayee Gupte
tmg9722@rit.edu

RIT | College of Science Astrophysical Sciences and Technology

Initial data generation and dynamical simulations of binary neutron star systems

By

Tanmayee Gupte

A Dissertation Submitted in Partial Fulfillment of the Requirements for the Degree of Doctor of Philosophy. in Astrophysical Sciences & Technology

School of Physics and Astronomy
College of Science
Rochester Institute of Technology
Rochester, NY

Date: December 12, 2022

Approved by:_____

Andrew Robinson, Ph.D Date
Director, Astrophysical Sciences and Technology

RIT | College of Science
Astrophysical Sciences and Technology

ROCHESTER, NEW YORK

CERTIFICATE OF APPROVAL

Ph.D. DEGREE DISSERTATION

The Ph.D. Degree Dissertation of *Tanmayee Gupte* has been examined and approved by the dissertation committee as satisfactory for the dissertation requirement for the Ph.D. degree in Astrophysical Sciences and Technology.

_____
Dr. Joshua Faber, Dissertation Advisor

_____
Dr. Nathaniel Barlow, Committee Chair

_____
Dr. Joel Kastner, Committee Member

_____
Dr. Scott Noble, External Member

Date _____

Acknowledgment

First and foremost I would like to thank my family for their never ending support. I must mention each of them individually starting with my mother who asked me about every test that I took these past 6 years and made sure I ate on time. My father helped me realize my love for stars by showing how important books can be. My brother shared the love for astronomy with me and taught me how important curiosity is. Last but not the least, Shefali understood how difficult writing a dissertation can be and calmed me every time I called her late at night.

I am extremely grateful to my advisor, Prof. Joshua Faber. His guidance has been invaluable professionally and personally. He taught me how to do research. I must express my genuine thanks for the knowledge he shared with me over these past years regarding neutron stars, black holes and of course books.

I am also very thankful to the collaborators in the Theoretical and Computational Astrophysics Network.

Finally, all the friends I have gained over these past years, I am going to cherish our bond for years to come. These past years have been difficult but I found a family in them and many moments of joy.

Computational Acknowledgement

I acknowledge the National Aeronautics and Space Administration for financial support from grant No. NNH17ZDA001N-TCAN-17-TCAN17-0018 80NSSC18K1488. Computational resources were provided by the NewHorizons and BlueSky Clusters at RIT, which were supported by NSF grants No. PHY0722703,No. DMS-0820923, No. AST-1028087 and No. PHY-1229173 and by FrontEra a NSF-funded petascale computing system at the Texas Advanced Computing Centerusing using NSF grant AST-20021. Lastly, I acknowledge the National Science Foundation (NSF) for financial support from Grants No. PHY-1659740 and No. PHY-1550436.

Abstract

The recent detection of gravitational waves (GWs) from a system of binary neutron stars (BNS) in coincidence with electromagnetic observations has launched a new era of multimessenger astrophysics. In light of the complementary knowledge to be gained through simultaneous observations, BNS mergers are one of the main targets for terrestrial GW interferometric detectors. These observations may prove critical in understanding the equation of state (EOS) of the nuclear matter inside the neutron star core, which is still poorly constrained given current observations. Understanding the neutron star (NS) EOS is critical for binary parameter estimation, and will hopefully aid in the prediction and detection of additional GW signals for systems with varying NS masses. While configurations of binary neutron stars having mass ratios far from unity are of great interest because of their potential observational signatures, generating accurate initial data for such systems has historically proven to be difficult, and relatively limited work has been done to date in simulating unequal-mass BNS because of a variety of numerical difficulties. In this work, we have modified the publicly available LORENE binary initial data code to advance our ability to construct unequal-mass BNS initial data, and used our results to initiate dynamical evolutions of BNS mergers performed using the Einstein Toolkit. We have investigated the quality of the initial data produced by our modified version of `LORENE` by evaluating a number of metrics, particularly the conservation of the Hamiltonian constraint when data are interpolated onto a grid for use in dynamical simulations.

Here we discuss the process by which we generate initial data and use it for launching dynamical simulations, as well as our analysis of the dynamics of the merger for varying mass ratios and different EOSs represented as simple polytropes and piecewise polytropes. In particular, we analyze the relationship between the BNS mass ratio, EOS, and the ejected mass during the merger, and classify the fate of the merger remnant produced in each case.

Contents

List of Figures

List of Tables

Chapter 1

Introduction

In August 2017, the first Binary Neutron Star (BNS) merger was detected by the Laser Interferometer Gravitational-Wave Observatory (LIGO) and the Virgo Gravitational Wave Observatory (VIRGO) [9]. The gravitational wave signal GW170817 was accompanied by observable electromagnetic signals from radio frequencies to γ-rays [10, 11]. This first joint gravitational and electromagnetic (EM) observation from a single source provided striking "multimessenger" data about the system progenitors, the merger process, and the merger's aftermath. Due to the availability of a wealth of varied observational probes, we hope to learn a great deal more about neutron star structure and astrophysics through these multiple channels. Over the next few years, we should be able to detect many more such events. As of 12^{th} April 2022, there have been two confirmed BNS merger events [12, 13] and many more probable and confirmed BHNS (black hole-neutron star) merger events as well – these latter ones marking the first time that a black hole-neutron star binary was confirmed to exist, as none have been conclusively observed through electromagnetic techniques.

Binary neutron star mergers have a rich and varied phenomenology when compared to binary black hole (BBH) mergers due to the presence of matter in neutron stars, and are consequently much more complex to model. In particular, while a BBH system can be fully described by the component masses and spins (and potentially the binary eccentricity, though this latter quantity is typically expected to be nearly zero [14, 15]), we are still working toward a proper

understanding of the fluid state describing the matter inside NS from the nuclear densities present in the core all the way to the crust at the surface [16].

At present, we possess only weak constraints on the equation of state (EOS) of nuclear matter inside the neutron star, from either gravitational wave (GW) observations of BNS systems or more traditional electromagnetic observations of pulsars [17]. The EOS, which describes the dependence of the pressure on the density and other parameters, will leave imprints on the BNS merger process and both the emitted GW and EM signals. As a result, BNS mergers can be used as an astrophysical laboratory to investigate the properties of nuclear matter in extreme conditions in a way largely inaccessible to other observational strategies.

In order to use multimessenger signals from BNS mergers for source parameter estimation, we need to compare the observed signals to theoretical GW templates and merger simulations that can predict the high-energy emission as a function of system parameters such as the total binary mass and mass ratio and the NS EOS. In both cases, full three-dimensional general relativistic numerical simulations of BNS are required to achieve quantitative accuracy. Among the sources of observational evidence that may aid us in probing the interiors of NS, the clearest signature may be provided by the timescale on which merger remnants collapse to BH, assuming that they do so at all. Numerical simulations are critical for determining under what circumstances the merged neutron star collapses immediately to a black hole, survives indefinitely as a hypermassive neutron star (HMNS), or lives for a brief time before a delayed collapse, as well as for helping us to understand the observational signatures characterizing each channel.

Given the importance of numerical simulations, one critical link in the process of generating a bank of numerical simulations is a corresponding bank of initial data models for NS with different masses and EOS, from which numerical simulations can be initiated. While NS masses are easily specified, it is critical that the EOS functional models be parameterized in ways that allow for comparison to observations by existing data analysis techniques.

Nearly all BNS initial data is generated under a similar set of assumptions. The binary is assumed to be in a quasi-equilibrium state, with a velocity field that permits a helical Killing

vector in time to describe the orbital motion [18]. Based on arguments about the weak viscosity present, the NS are assumed to be essentially irrotational [19, 20]; indeed, given the orbital period of 1-5 ms immediately prior to the merger, even relatively rapidly rotating pulsars can be treated as nearly irrotational. While magnetic fields are expected to be present, the field strengths yield only perturbative corrections to the overall pressure throughout a star and are typically ignored when constructing quasi-equilibrium configurations.

As a result, there are a limited number of physical parameters to vary to describe a BNS system prior to the merger. Besides the EOS, as discussed above, the most important parameters are simply the masses of the two NS. One challenge that we have faced here has been the fact that many of the leading numerical techniques struggle with binary mass ratios significantly different than unity (thus $q \equiv \frac{M_2}{M_1} < 1$). Such mergers are of particular interest to the community, since mass loss from a binary merger is expected to scale strongly with the mass ratio, based on previous numerical studies [21, 22, 23]

This dissertation has the following organization: Chapter 2 consists of the background material required to understand the astrophysics of neutron stars and numerical relativity. Chapter 3 has a description of the code `LORENE` used to produce initial data of the binary neutron star configurations. In chapter 4 we describe the various modifications we have done to the `LORENE` code in order to expand the parameter space of BNS configurations. In chapter 5 we present our results obtained from investigating the quality of initial data, along with the results from dynamical simulations of BNS configurations we conducted. Chapter 6 consists of a brief description of the conclusions obtained from conducting the research presented in this dissertation, and describes future steps anticipated for our publicly available binary neutron star initial data library.

Chapter 2

Background

To understand what we can learn by studying merging neutron star systems, it helps to explain what neutron stars are, the physics that describes them, and how they are produced astrophysically (Sec. 2.1). We also consider how they are produced in binaries via binary stellar evolution processes and the processes that take close binaries and drive them to coalescence and merger (Sec. 2.2). Since these mergers have long been considered a critical target for gravitational wave detectors like LIGO and VIRGO, we discuss how these systems produce gravitational radiation and how we interpret it via the signals we observe, and then turn our focus to how gravitational radiation and electromagnetic observations may be combined in this new era of "multimessenger astronomy" (Sec. 2.3; noting that neutrino observations may also lay claim to this latter name as well). Finally, we discuss the approach used by the `Lorene` code to construct binary neutron star initial data, the main topic of this thesis (Sec. 2.4).

2.1 Neutron Stars

A neutron star is a compact star with a radius between 9 - 15 km, a mass range between 1 - 3 $M_\odot$ and a central density of $n_0 = 0.16\text{fm}^{-3}$ [24]. Composed of matter at nuclear densities, they are one of the most dense objects in the universe. Neutron stars are made of neutrons, as the name suggests, but a fraction of protons, electrons and/or muons is also present to neutralize the matter. Held together by a strong gravitational field, inward forces cannot be

balanced solely by electron Fermi gas pressure [25], [26], like in a white dwarf; rather, repulsive strong nuclear forces are needed to balance the gravitational field inside neutron stars [27].

2.1.1 The final stages of stellar evolution

How do neutron stars form? The post-main sequence evolution of massive stars results in the star exhausting its supply of hydrogen and helium in its core, while it continues to fuse heavier elements such as carbon and oxygen there (and possibly these and lighter elements in surrounding shells), eventually forming an iron core. This terminates the fusion process, since iron is the most stable element in terms of binding energy. As the iron core becomes more massive, the star can no longer be supported by hydrostatic pressure and collapses under its own gravity. This process results in a supernova, a catastrophic explosion that can form either a neutron star or a black hole, depending on the initial mass of the star.

Numerical simulations of supernova explosions are computationally challenging as they include nuclear physics motivated equation of state, a detailed description of neutrino interactions and general relativity. Previous work of numerical simulations show that the mass of a newly formed NS depends mainly on the mass of the progenitor [28, 29]. Progenitors with an initial mass, $M \geq 10M_{\odot}$ form NS with an average mass of M_{NS} $1.4M_{\odot}$ and heavier mass NS $M > 1.6M_{\odot}$ are formed by progenitor having masses above $M > 20M_{\odot}$.

Given the potential variability in the detailed dynamics of the supernova process, the mass distribution of newly formed NS remains somewhat uncertain, and will be difficult to fully constrain using numerical simulations for quite some time into the future.

In the first phase during the collapse, a shock wave is generated as the central density of star reaches the nuclear equilibrium density. The star emits energy and angular momentum into neutrino radiation, the latter due to the presence of turbulence and hydrodynamical instabilities. The neutrino radiation is accompanied by electron captures, thus leaving behind a neutron-rich star:

$$p^{+} + e^{-} \rightarrow n + \nu_{e}, \tag{2.1.1}$$

In the second stage, the so-called “Kelvin-Helmholtz phase”, the proto-neutron star cools and

shrinks down, becoming transparent to neutrinos and thus forming a cool neutron star [30]. Neutron stars typically have strong magnetic fields, as the field embedded in the stellar material increases in strength by several orders of magnitude during the gravitational collapse because of flux conservation. A typical neutron star has a magnetic field of $10^8 - 10^{12}$ Gauss, but some neutron stars are even thought to have magnetic fields of up to 10^{15} Gauss. These latter ones form a special class of NS called magnetars. Several NS emit pulses of electromagnetic radiation, typically in the radio band and less frequently in the X-ray or gamma ray components of the electromagnetic spectrum, forming the population of pulsars we observe on Earth [1]. These pulses arise due to the misalignment of the rotational axis and the dipolar magnetic field. These pulses are visible from the earth when the star's radiation beam crosses the observer's line of sight. We are able to directly measure the rotational period of a pulsar as it is equal to the pulse period.

2.1.2 Equation of state

The nuclear matter equation of state, which states how the pressure behaves as a function of other physical parameters inside the NS, remains poorly constrained based on theoretical predictions and limited experimental evidence. Due to the extreme nature of the physical conditions (pressure, density, gravitational potential), we cannot reproduce the appropriate conditions stably through experiments on earth for longer than fleetingly brief timescales. Therefore, we cannot perform first-principles Quantum Chromodynamical calculations for the extreme parameter space required to describe NS [32]. In order to parameterize our uncertainty, different approximate EOS models are used widely throughout the numerical modeling community, with parameters that can be chosen to match specified theoretical EOS models to the desired accuracy. In this work, we have explored three different types of EOSs: simple polytropes (in which the pressure is related to the density by a simple power-law model), piecewise polytropes, and tabulated EOS. These are discussed in Sections 3.2.1, 3.2.2 and 5.2 respectively.

[1] There are 3,342 known pulsars listed in the database maintained by the Australian Telescope National Facility [31], of which 359 are in binaries (two of which form the only known pulsar-pulsar binary, PSR J0737-3039).

Given an EOS model, the neutron star structure, including its mass and radius, can be determined using the EOS and the Tolman-Oppenheimer-Volkov equations [26, 25]:

$$\frac{dP}{dr} = -\frac{1}{r^2}(\epsilon + P)(m + 4\pi r^3 P)\left(1 - \frac{2m}{r}\right)^{-1}, \tag{2.1.2}$$

$$\frac{dm}{dr} = 4\pi r^2 \epsilon \quad \Rightarrow \quad M = \int_0^R 4\pi r^2 \epsilon \, dr. \tag{2.1.3}$$

The only independent variable is r (radius) and all other variables are functions of radius. In the above equations, ϵ is the energy density and P is the pressure. The enclosed mass, $m(r)$, is the total mass contained between the center of the NS at $r = 0$, where $P = P_c$ and $\epsilon = \epsilon_c$, to a radius of r. The total NS mass M is calculated from the center to the surface of the star where $r = R$ and $P = 0$. The microscopic properties of the NS can be described by the (barotropic) equation of state of the matter, and we can derive the mass-radius relationship for cold NSs by solving the TOV equations for different values of the central density (or related quantities). Should we be able to place simultaneous constraints on the NS mass and radius, it should be useful for helping to constrain the properties of matter at nuclear densities.

2.2 Binary neutron star systems

There is a well-accepted evolutionary pathway that leads to the formation of close binary neutron stars (and BH-NS systems). While other options have been discussed, the standard channel described below and shown in Fig. 2.2 is favored by population synthesis calculations to produce the number of observed systems detected to date. In this channel, both the progenitor stars need to have masses $M \geq 8\ M_\odot$ to ensure a pair of supernovae [1, 33]. The more massive primary star evolves for over a million years along the main sequence before it enters the giant phase, the lifetime depending on the star's mass with heavier stars lasting for less time and smaller ones for more before exhausting their fuel supply and triggering the giant phase. Eventually, the primary undergoes a supernova, either a "Type Ib", "Type Ic", or "Type II" depending on the particular absorption spectra that would be observed from the

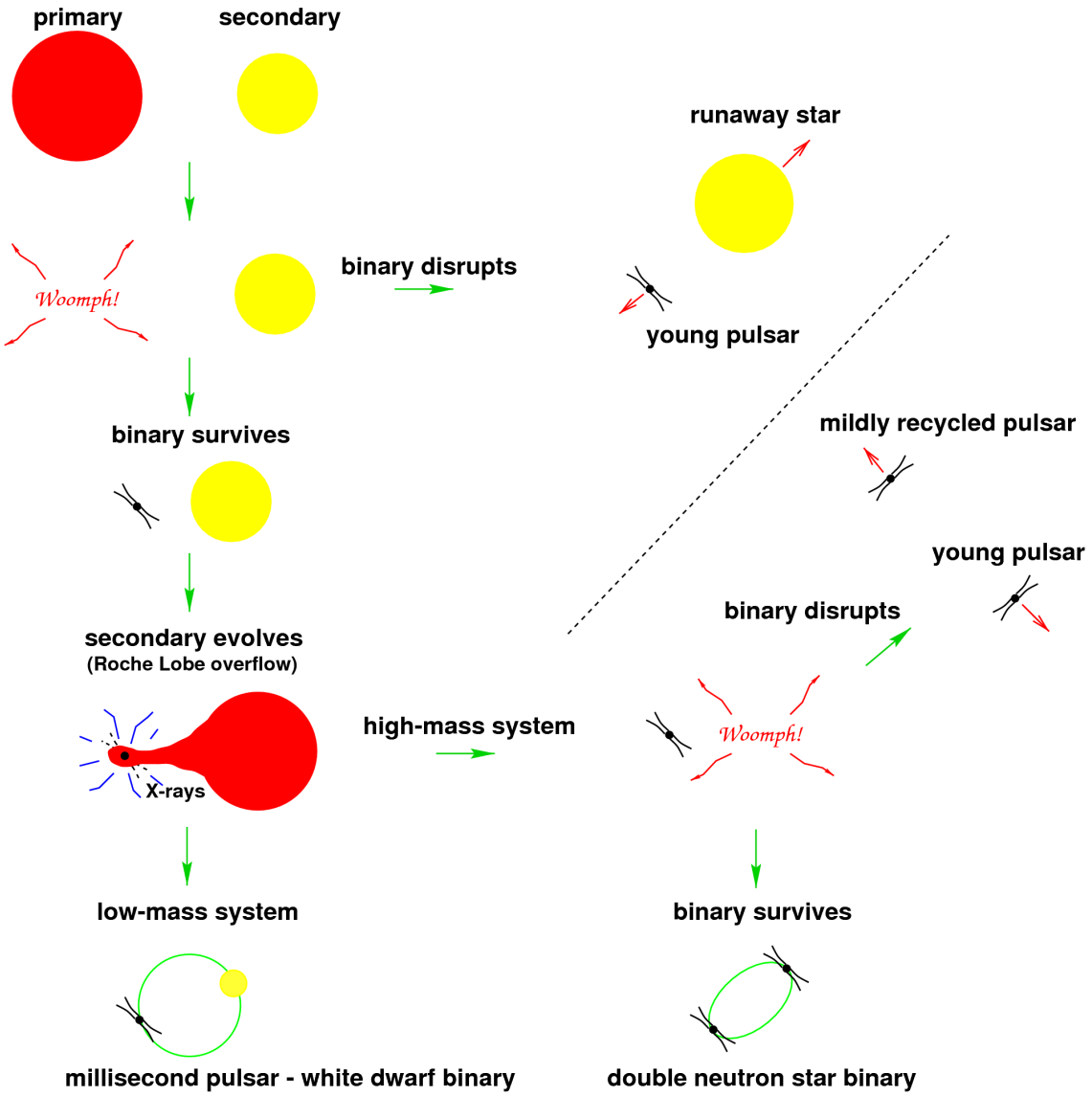

Figure 2.1: Cartoon showing the formation of binary neutron star system, taken from [1]

ejected material, leaving behind a compact object at its core.

The secondary, less massive star follows a slightly different evolutionary process. After the primary becomes a compact object, the secondary eventually leaves the main sequence in turn and enters the giant phase, which triggers the binary's evolution into a common envelope (CE) phase, as the secondary overflows its Roche lobe in an unstable process and expands while the primary plunges within the newly formed envelope. The separation between the stars decreases dramatically because of dynamical friction, releasing sufficient energy to eventually expel the

envelope. Without the decrease in the separation between the components, the stars would not merge through the emission of GWs within a Hubble time (i.e., the age of the universe, used as a standard heuristic timescale throughout astrophysics). Next, the helium rich core of the secondary undergoes a supernova explosion, after which the binary could either end up as an unbound system or as a tight binary, with the end result depending on the magnitude and orientation of the supernova kick.

The properties of binaries containing NS has been well-studied through a number of different channels, primarily by the study of X-ray binaries and pulsars in binaries. In [34], they extrapolate from a population of 15 known pulsars in binaries in the Milky Way to estimate a population of up to $\sim$ 1000 active pulsars in binaries in the galaxy – the vast majority of which beam in directions away from the Earth – representing a small subset of the approximately 270,000 neutron stars in unmerged binaries within the galaxy. The properties of these binaries remain somewhat uncertain; binary separations are still often fit using power-laws in population synthesis calculations [35] and masses can be difficult to determine with precision. The mass ratio of neutron stars seen in the binary radio pulsar systems detected to date is typically close to unity and masses are constrained to a small range, with an average mass of 1.4 $M_\odot$. On the other hand, the detected X-Ray binary systems (NS + regular star or NS + white dwarf) show a broader mass range of X-ray pulsars and have a slightly higher average mass. We have observed a range of masses for NS from near $1.35 M_\odot$ [36] to $2.1 \pm 0.2 M_\odot$ [37], which provides important information on the production mechanisms of neutron stars and the behavior of nuclear matter.

2.2.1 Stages of a Binary Merger

A binary neutron star merger, or that of any other pair of compact objects, consists qualitatively of three different phases: inspiral, merger and ringdown. Each of the three phases presents a distinct set of challenges to model numerically and to describe in theoretical terms. To visualize a binary neutron star merger, we can begin from the cartoon shown in Figure 2.2. The cartoon was originally designed to describe a binary black hole merger, and is commonly

attributed to Kip Thorne [2]. It may be adapted to a binary neutron star merger by noting that neutron stars are assumed to be non-spinning, or at least to spin much more slowly than typical BHs. Additionally, the result of the "ringdown" phase may either be a newly formed BH or a NS that survives against gravitational collapse.

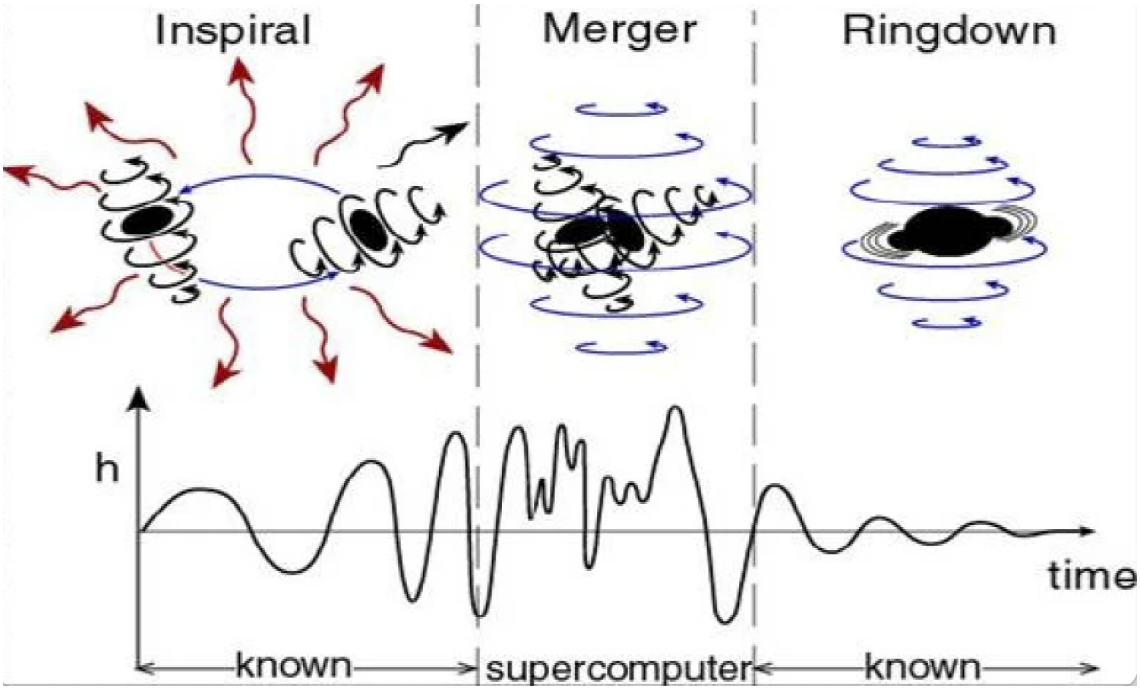

Figure 2.2: Cartoon image of a binary black hole merger, that may be applied to binary neutron mergers as well. Image taken from [2].

The three phases of a neutron star merger can be summarized as follows:

- During the *inspiral* phase, the orbital separation decays over long timescales through gravitational wave emission. This phase takes up the entire lifetime of the binary until its last few milliseconds. We can describe the binary system in the inspiral phase using a quasiequilibrium formalism until the point where the gravitational radiation timescale becomes comparable to the dynamical timescale. The evolution of the binaries in time, as well as their deformations due to tidal effects, are well described by the post-Newtonian approximation to general relativity.

[2]See, e.g., "Spacetime Warps and the Quantum World: Speculations about the Future" in R. H. Price, ed., The Future of Spacetime. W. W. Norton, New York, 2002, pp. 109-152. https://www.its.caltech.edu/ kip/index.html/PubScans/VI-42.pdf).

- Binaries become unstable when their separation becomes comparable to a few times their radii. As they come closer, dynamical instabilities set in, and the stars plunge together as the binary enters the *merger* phase. We need to perform full general relativistic simulations to understand the hydrodynamics of the merger phase. According to past simulations, if the two stars have nearly equal masses, they collide with each other in a balanced way, gradually forming first a bar like object and then a more axisymmetric configuration. On the other hand, if the primary is substantially heavier than the secondary, the less massive star gets torn apart due to tidal disruptions and largely accretes onto the primary. Numerical calculations of the GWs produced in binary mergers uniformly predict the largest GW amplitudes during this phase. Important information regarding the EOS of the NSs should in theory be possible to infer from within the GW emission during this phase.
- In the final stage, the *ringdown* phase, the system will settle into a dynamically stable configuration and emit a lower-amplitude, higher-frequency GW signal. The particular GW properties depend on the final remnant's mass and rotational profile. The remnant will always be a compact object, either a black hole or a neutron star. If the remnant is a neutron star, it can fall into one of the three categories:

  Stable neutron star: The NS mass is less than the maximum mass supported by the nuclear matter EOS for an isolated, non-rotating configuration.

  Supramassive neutron star: The NS is above the maximum stable stationary isolated mass given by the Tolman-Oppenheimer-Volkov (TOV) equation describing the relativistic stellar structure, but uniform rotation can support it for a much longer time because of centripetal effects.

  Hypermassive neutron star: If the remnant has a mass above the supramassive limit, it may fall into the hypermassive regime, where it is supported against gravitational collapse by rapid differential rotation. This cannot support itself on the same timescales as a supramassive or stable NS, since any dissipative process, e.g.,

viscosity or magnetic effects, will damp away the differential rotation and lead to the remnant's collapse into a black hole on a relatively shorter timescale (though still potentially quite long with respect to what most 3-d numerical simulations can model).

If the mass of the remnant is large enough, it will collapse into a black hole immediately, bypassing the HMNS stage entirely.

2.3 Gravitational Waves and Multimessenger Astronomy

The existence of gravitational waves was one of the immediate consequences of Einstein's General Theory of Relativity (GR). They are perturbations in spacetime resulting from accelerating massive bodies, traveling at the speed of light with amplitudes that decay inversely with the distance to their source. They have a quadrupolar nature, as opposed to electromagnetic waves which have a leading-order dipolar nature. They are most easily derived from the general relativistic field equations when treated in a linear regime. When we are far away from the compact sources, we can treat the spacetime metric as the Minkowski special relativistic metric $\eta_{\mu\nu}$ plus a perturbation $h_{\mu\nu}$ given as

$$g_{\mu\nu} = h_{\mu\nu} + \eta_{\mu\nu}. \tag{2.3.4}$$

As we assume the perturbation to be very small, $||h_{\mu\nu}|| << 1$, we can ignore higher-order terms and thus assume the weak nature of the gravitational field. The Christoffel symbols can be expanded in terms of $h_{\mu\nu}$ as

$$\begin{aligned} \Gamma^{\nu}_{\alpha\beta} &= \frac{1}{2}\eta^{\mu\nu}(\partial_\beta h_{\mu\alpha} + \partial_\alpha h_{\mu\beta} + \partial_\mu h_{\alpha\beta}), \\ &= \frac{1}{2}(\partial_\beta h^{\nu}{}_{\alpha} + \partial_\alpha h^{\nu}{}_{\beta} + \partial^{\nu} h_{\alpha\beta}). \end{aligned} \tag{2.3.5}$$

Thus, the Riemann tensor becomes

$$\begin{aligned} R^{\nu}_{\alpha\beta\mu} &= \partial_\beta \Gamma^{\nu}_{\alpha\mu} + \partial_\mu \Gamma^{\nu}_{\alpha\beta}, \\ &= \frac{1}{2}(\partial_\alpha \partial_\beta h^{\nu}{}_{\mu} + \partial_\mu \partial^{\nu} h_{\alpha\beta} - \partial_\beta \partial^{\nu} h_{\alpha\mu} - \partial_\mu \partial_\alpha h^{\nu}{}_{\beta}). \end{aligned} \tag{2.3.6}$$

In linearized theory the Ricci tensor becomes

$$R_{\alpha\beta} = R^{\mu}_{\alpha\beta\mu} = \frac{1}{2}(\partial_\mu \partial_\beta h^{\mu}{}_{\alpha} + \partial^{\mu} \partial_\alpha h_{\beta\mu} - \Box h_{\beta\alpha} - \partial_\alpha \partial_\beta h, \tag{2.3.7}$$

where the d'Alembertian wave operator is given by

$$\Box = \partial_\mu \partial^{\mu} = \nabla^2 - \partial_t{}^2, \tag{2.3.8}$$

and h is the trace of metric perturbation.

The general theory of relativity gives the Einstein tensor as

$$G_{\alpha\beta} = R_{\alpha\beta} - \frac{1}{2}\eta_{\alpha\beta} R. \tag{2.3.9}$$

We can calculate the Ricci scalar using the Ricci tensor as

$$R = R^{\alpha}_{\alpha} = (\partial_\mu \partial_\alpha h^{\mu}{}_{\alpha} - \Box h). \tag{2.3.10}$$

Thus, the Einstein tensor becomes

$$\begin{aligned} G_{\alpha\beta} &= \frac{1}{2}(\partial_\mu \partial_\beta h^{\mu}{}_{\alpha} + \partial^{\mu} \partial_\alpha h_{\beta\mu} - \Box h_{\beta\alpha} - \partial_\alpha \partial_\beta h - \eta_{\alpha\beta} \partial_\mu \partial_\alpha h^{\mu}{}_{\alpha} - \eta_{\alpha\beta} \Box h), \\ &= 8\pi T_{\alpha\beta}. \end{aligned} \tag{2.3.11}$$

Einstein's equations in linearized gravity yield

$$\Box \bar{h}_{\alpha\beta} - 2\partial_{(\alpha} \partial^{\rho} \bar{h}_{\beta)}{}_{\rho} + \eta_{\alpha\beta} \partial^{\rho} \partial\sigma \bar{h}_{\rho\sigma} = -16\pi T_{\alpha\beta}, \tag{2.3.12}$$

where

$$\bar{h}_{\alpha\beta} = h_{\alpha\beta} - \frac{1}{2} h \eta_{\alpha\beta}, \tag{2.3.13}$$

is the trace reversed metric perturbation.

The metric given by the above equation is not unique. When we do an infinitesimal coordinate transformation such as

$$x^{\alpha} \longrightarrow x^{\alpha} + \xi^{\alpha}, \tag{2.3.14}$$

it leaves the equation unchanged. Therefore the linearized theory is invariant under gauge transformation

$$h_{\alpha\beta} \longrightarrow h_{\alpha\beta} + 2\partial_{(\alpha}\xi_{\beta)}. \tag{2.3.15}$$

As a result, this transformation will not change the field equations. This problem is further simplified by making the choice of the Lorenz gauge

$$\partial^{\alpha}\bar{h}_{\alpha\beta} = 0. \tag{2.3.16}$$

This is analogous to the gauge transformation in electromagnetism where the Faraday tensor is invariant under the gauge transformation of the vector potential, to simplify Maxwell's equations.

The final form of Einstein's equations in weak field limit under linearized theory becomes

$$\Box\bar{h}_{\alpha\beta} = -16\pi T_{\alpha\beta}. \tag{2.3.17}$$

The above equation has the form of wave equation, propagating at the speed of light. In the case of the field equations in a vacuum and far away from the source we get

$$\Box\bar{h}^{\alpha\beta} = 0. \tag{2.3.18}$$

We can decompose the metric using Fourier transformation as

$$\Box\bar{h}^{\alpha\beta} = \int A_{\alpha\beta}(k)e^{ik_\rho x^\rho}d^4k. \tag{2.3.19}$$

We can further impose a transverse traceless (TT) gauge condition along with the Lorenz gauge condition to make the metric perturbation purely spatial and traceless. This gives us

$$h = 0, \tag{2.3.20}$$

$$h_{\alpha\beta} = \bar{h}_{\alpha\beta}. \tag{2.3.21}$$

In the TT gauge, for a gravitational wave traveling in the z direction, the metric perturbation becomes

$$h^{TT}_{\alpha\beta} = \begin{pmatrix} 0 & 0 & 0 & 0 \\ 0 & h_+ & h_\times & 0 \\ 0 & h_\times & h_+ & 0 \\ 0 & 0 & 0 & 0 \end{pmatrix}, \tag{2.3.22}$$

where h_+ is called the plus polarization and $h_\times$ is the cross polarization, making them the only two independent components of the waveform. For a circle of particles, with their center at the center of a Cartesian coordinate system, the plus polarization will elongate the particle configuration along the x- and y-axes in alternating fashion while the cross polarization will elongate it along the bisector of x- and y-axes.

If we wish to consider the production of gravitational waves by matter sources, we need to couple Einstein's equations with matter. Starting from the source equation for each component $\bar{h}_{\alpha\beta}(t, \vec{x})$, the linear wave equation (Eq. 2.3.17)

$$\bar{h}_{\alpha\beta}(t, \vec{x}) = 4\int \frac{T_{\alpha\beta}(t', \vec{x'})}{|\vec{x} - \vec{x'}|}d^3x', \tag{2.3.23}$$

where t' is the retarded time given as

$$t' = t - |\vec{x} - \vec{x'}|. \tag{2.3.24}$$

As we are interested in deriving the gravitational waves far from the source, $r = |\vec{x}| >> R_{\text{source}}$, we can further simplify the above expression by using the "slow source" approximation, where the wavelength linked with the characteristic source is much bigger than the source size, $\lambda >> R_{\text{source}}$. As a result, we get

$$\bar{h}_{\alpha\beta} = \frac{4}{r} \int T_{\alpha\beta}(t - r, \vec{x'}) d^3\vec{x'}. \tag{2.3.25}$$

We can relate the above term to the quadrupole source term and in doing so, explain why conservation of mass and momentum imply that monopole and dipole gravitational radiation cannot exist. Indeed, monopole radiation contributions would result from a change in time of the zeroth moment of the mass distribution, implying non-conservation of mass, and dipole radiation from the change in time of the mass-dipole moment, which is always zero when viewed in the center-of-mass frame assuming conservation of momentum.

Using the conservation of energy momentum tensor and integrating over a considered volume we get

$$\int T^{ij}(x) dx^3 = \frac{1}{2} \partial_0^2 \int x^i x^j T^{00} d^3x, \tag{2.3.26}$$

Applying the above condition to eqn (2.3.25)

$$\bar{h}_{ij}(t, \vec{x}) = \frac{2}{r} \ddot{I}_{ij}(t - r), \tag{2.3.27}$$

where $\ddot{I}_{ij}$ is the second mass moment given as

$$I_{ij}(t) = \int \rho(t, \vec{x}) x_i x_j d^3x. \tag{2.3.28}$$

We get the quadrupole formula by projecting eqn (2.3.27) in TT gauge, given as

$$h_{ij}^{TT}(t,\vec{x}) = \frac{2}{r}\Lambda_{ij,kl}(\vec{n})\ddot{Q}_{ij}(t-r), \tag{2.3.29}$$

where

$$\Lambda_{ij,kl} = P_{ik}P_{jl} - \frac{1}{2}P_{ij}P_{kl}, \tag{2.3.30}$$

where $P_{ij} = \delta_{ij} - n_i n_j$ is the projection operator with $\vec{n} - \vec{x}/\vec{r}$ and Q_{ij} is mass quadrupole moment,

$$Q_{ij}(t) = \int \rho(t,\vec{x}) \left(x_i x_j - \frac{1}{3}|\vec{x}|^2 \delta_{ij} \right). \tag{2.3.31}$$

2.3.1 Binary inspiral

In this section, we will derive the predicted inspiral of a binary system, applying it to the regime where the NS are separated enough so that tidal forces are negligible. The binaries are expected to be in circular orbits when they become visible to laser interferometers, due to gravitational wave emission, which has the effect of damping away eccentricity on a faster timescale than the inspiral timescale. Let us consider a binary system of stars with individual masses M_1 and M_2. The reduced mass of the system is given by

$$\mu = \frac{M_1 M_2}{M_1 + M_2}. \tag{2.3.32}$$

Further, let us assume the stars are spherical and irrotational, so the total Newtonian energy of the system is given by

$$\begin{aligned} E(r) &= \frac{1}{2}(M_1 v_1^2 + M_2 v_2^2) - \frac{GM_1 M_2}{r}, \\ &= -\frac{1}{2}\frac{GM\mu}{r}, \end{aligned} \tag{2.3.33}$$

and the angular velocity given by

$$\omega = \sqrt{\frac{GM}{r^3}}, \tag{2.3.34}$$

where r is the binary separation. The quadrupole moment of the system is given as

$$\begin{aligned} Q_{xx} &= \mu r^2(\cos^2\theta - \frac{1}{3}) = \frac{1}{2}\mu r^2 \cos 2\theta, \\ Q_{xy} &= \mu r^2(\cos\theta \, \sin\theta) = \frac{1}{2}\mu r^2 \sin 2\theta, \\ Q_{xz} &= \mu r^2(\sin^2\theta - \frac{1}{3}) = -\frac{1}{2}\mu r^2 \cos 2\theta. \end{aligned} \tag{2.3.35}$$

The energy loss rate in gravitational waves at a moment where they are separated at a distance r is given as

$$\begin{aligned} \frac{dE_{GW}}{dt} &= \frac{16G\mu^2 r^4 \omega^6}{5c^5}(2\cos^2\theta \, 2\sin^2\theta), \\ &= \frac{32G^4\mu^2 M^3}{5c^5 r^5}. \end{aligned} \tag{2.3.36}$$

The inspiral rate is calculated by equating the energy loss caused by gravitational radiation with the energy change resulting from a decrease in separation, such that

$$\begin{aligned} \frac{dr}{dt} &= \left(\frac{dE_{GW}}{dt}\right)\left(\frac{dE(r)}{dr}\right)^{-1}, \\ &= \frac{32G^4\mu^2 M^3}{5c^5 r^5}\frac{2r^2}{GM\mu}, \\ &= \frac{64G^3\mu M^2}{5c^5 r^3}. \end{aligned} \tag{2.3.37}$$

We can integrate and solve for $r(t)$ to give

$$r(t) = r_0\left(1 - \frac{t}{\tau}\right)^{\frac{1}{4}}, \tag{2.3.38}$$

where τ_0 is the expected time remaining for the binary to merge, if they were point masses, given as

$$\tau_0 = \frac{5}{256}\frac{5c^5 r_0^4}{G^3\mu M^2}. \tag{2.3.39}$$

When the stars get too close, we can now longer make use of the point mass formalism, as tidal interactions will become important in describing the dynamics of the simulations.

2.3.2 Multimessenger Astronomy with binary neutron star mergers

Along with emitting gravitational waves, BNS and BH-NS systems can also emit a wide range of electromagnetic and neutrino signals. They provide a wealth of varied probes and multiple avenues to learn more about the structure and astrophysics of neutron stars and open a new field of multimessenger astrophysics. In August 2017, the Laser Interferometer Gravitational Wave Observatory (LIGO) [38] and the Virgo Gravitational Wave Observatory [39] detected a BNS merger for the first time, a source named GW170817. It was accompanied by a mulitmessenger photon display with detections covering the entire electromagnetic spectrum, all the way from radio frequencies to γ-rays [10]. These events had been predicted to be sites of production of r-process elements, a prediction that was confirmed by the emission of IR/optical signals coincident with GW170817 [40, 41, 42]. It was also accompanied by a short gamma ray burst (SGRB) [43], as had also been widely suggested for many years (see, e.g., [44]).

SGRBs are among the most energetic astrophysical events that have ever been observed, each releasing around 10^{48} - 10^{52} ergs (see, e.g., [45] for a review of SGRB models in the LIGO era). The working mechanism of the central engine of SGRBs had not previously been conclusively determined, and various models had been proposed to explain the prompt emission from an ultrarelativistic outflow. Before LIGO had even been constructed, it was suggested that multimessenger events could be used to study the mechanism behind SGRBs in the Universe. They can also be used study the effects of NS EOSs and mass ratios on the properties of the merger remnant, and thus to place constraints on the central engine of SGRBs.

BNS merger events are also predicted to be the primary sites of production for r-process elements in the universe [46]. During the merger, for mass ratios that differ significantly from unity, the heavier star tears apart the outer layers of the lighter and less massive NS, the matter from which is either unbound and cast away or left bound to the system to form some kind of accretion disk. The mass ejecta of the BNS mergers hosts suitable conditions for producing heavy elements via nuclear processing. This is accompanied by characteristic EM radiation patterns called a “kilonova”, in which heavy radioactive elements decay and emit

radiation in ultraviolet, visible and near-infrared wavelengths. We can conduct fully general relativistic numerical simulations for predicting the characteristic properties of mass ejected during BNS and BH-NS merger events by expanding the parameter space for these systems and use them to correctly interpret GW and EM signals from multimessenger events.

2.3.3 Detected BNS and BHNS Events

Table 2.1 lists all observed GW events as detected by LIGO-VIRGO collaboration, for which the mass of the second star is $\leq 3M_{\odot}$, as of April 12, 2022. The data displayed here clearly show the importance of generating *unequal* mass BNS initial data, and studying the BNS mergers that result from them.

Name	$M_1(M_{\odot})$	M_2 $(M_{\odot})$	Release	Reference
GW170817	$1.46^{+0.12}_{-0.01}$	$1.27^{+0.09}_{-0.09}$	GWTC-1-confident	[47]
GW190425	$1.74^{+0.17}_{-0.09}$	$1.56^{+0.08}_{-0.14}$	GWTC-2.1-confident	[48]
*GW*190426_152155	$5.7^{+3.9}_{-2.3}$	$1.5^{+0.08}_{-0.5}$	GWTC-2.1-marginal	[48]
GW190814	$23.2^{+1.1}_{-1.0}$	$2.6^{+0.08}_{-0.09}$	GWTC-2.1-confident	[48]
*GW*190917_114630	$9.3^{+3.4}_{-4.4}$	$2.1^{+1.5}_{-0.5}$	GWTC-2.1-confident	[49]
*GW*191219_163120	$31.1^{+2.2}_{-2.8}$	$1.17^{+0.07}_{-0.06}$	GWTC-3-confident	[50]
*GW*200105_162426	$9.0^{+1.7}_{-1.7}$	$1.91^{+0.33}_{-0.24}$	GWTC-3-marginal	[50]
*GW*200115_042309	$5.0^{+2.0}_{-2.5}$	$1.44^{+0.85}_{-0.29}$	GWTC-3-confident	[50]
*GW*200210_092254	$24.1^{+7.5}_{-4.6}$	$2.83^{+0.42}_{-0.47}$	GWTC-3-confident	[50]

Table 2.1: BNS and BH-NS events detected by the LIGO-VIRGO collaboration through 12^{th} April 2022.

2.4 Initial data and the Conformal Thin Sandwich Formalism

All dynamical simulations of merging BNS systems require a starting point. AS is typical for hyperbolic PDE systems, the initial data must be generated through an approach that is consistent with, but very different in mathematical nature from, the time evolution equations. Indeed, the equations describing a self-consistent spacetime and matter configuration describing a quasi-equilibrium system are generally written down in elliptic form, and solved using a different set of numerical codes and techniques than those used to perform evolution simulations in time.

The most commonly used approach for generating BNS initial data by specifying the evolution of the spatial metric is the Conformal Thin Sandwich (CTS) formalism. The 4-dimensional spacetime is treated equivalently to a stack of 3-dimensional spacelike hypersurfaces Σ. The hypersurfaces do not intersect and are specified as a function of global time. This approach is called the 3+1 decomposition [51] and the metric is defined by

$$ds^2 = -\alpha^2 dt^2 + \gamma_{ij}(dx^i + \beta^i dt)(dx^j + \beta^j dt), \tag{2.4.40}$$

where α is lapse function, β^i are components of the shift vector (a relativistic 3-d vector), and γ_{ij} is the spatial 3-metric induced on the hypersurface. The lapse function measures the amount of proper time elapsed between two neighboring time slices along the normal vector to the hypersurface, while the shift vector β^i measures the difference between the normal vector and the time vector connecting two neighboring hypersurfaces. Thus, the lapse and shift, both of which involve a gauge freedom to specify their respective properties, measure the evolution of coordinates with time. We can use the 3+1 metric to cast the Einstein equations into a set of time-evolution equations for which the evolved quantities must satisfy the Hamiltonian and momentum constraint equations to remain self-consistent. With the help of extrinsic curvature, which measures the difference between normal vectors n to the hypersurface at adjacent points, defined as

$$K_{ab} = -\gamma_a^c \gamma_b^d \nabla_c n^d. \tag{2.4.41}$$

where n^i is the normal vector, the Hamiltonian constraint can be expressed as

$$R + K^2 - K_{ab}K^{ab} = 16\pi\rho, \tag{2.4.42}$$

where ρ is the total energy density as measured by a normal observer and R is the Ricci scalar (K is the trace of the extrinsic curvature). The momentum constraint equation is given as

$$D_b K_a^b - D_a K = 8\pi S_a, \tag{2.4.43}$$

with S_a as the momentum density measured by a normal observer and D_a denoting the spatial covariant derivative with respect to coordinate x^a. These constraint equations allow for the conversion of four dimensional manifold with the metric (g_{ab}) into a 3-dimensional hypersurface Σ with field data (γ_{ab}, K_{ab}). We have to solve these equations to construct initial data, but they provide more equations than the number of unknowns. One of the methods used to provide a sufficient number of constraints is to perform a conformal decomposition of the constraint equations using the CTS approach. Here, the spatial metric is conformally decomposed as [52, 53]

$$\gamma_{ij} = \psi^4 \overline{\gamma_{ij}}, \tag{2.4.44}$$

where the conformal factor ψ is defined such that $\det|\,\overline{\gamma_{ij}}\,| = 1$. The extrinsic curvature can be split into two parts given as

$$K_{ij} = A_{ij} + \frac{1}{3}\gamma_{ij}K = \psi^{-2}\overline{A}_{ij} + \frac{1}{3}\gamma_{ij}K, \tag{2.4.45}$$

with K as the trace of K_{ij} and A the traceless component. This method provides information about γ_{ij} on two time slices. We define the traceless part of the time derivative of the spatial metric as

$$u_{ij} = \gamma^{1/3}\partial_t(\gamma^{-1/3}\gamma_{ij}), \tag{2.4.46}$$

and use it to redefine $\overline{A}^{ij}$ in terms of shift vector as

$$\overline{A}^{ij} = \frac{\psi^6}{2\alpha}[(\overline{L}\beta)^{ij} - \overline{u}^{ij}], \tag{2.4.47}$$

where $\overline{L}$ is the conformal killing operator defined as

$$(\overline{L}G)^{ij} = \overline{D^i}G^j + \overline{D^j}G^i - \frac{2}{3}\overline{\gamma}^{ij}\overline{D}_k G^k. \tag{2.4.48}$$

For quasiequilibrium data we choose $\overline{u}_{ij} = 0$ and $\partial_t K = 0$. Further, we assume maximal

slicing (K=0) to get the derivative of the lapse from the ADM equations as

$$\overline{D^2}(\alpha\psi) = \alpha\psi\left(\frac{7}{8}\psi^{-8}\overline{A}_{ij}\overline{A}^{ij} + \frac{1}{8}\overline{R} + 2\pi\psi^4(\rho + 2S)\right), \tag{2.4.49}$$

with

$$\psi^{-4}\overline{R} = R + 8\psi^{-5}\overline{\gamma}^{ij}\overline{D}_i\overline{D}_j\psi. \tag{2.4.50}$$

The Hamiltonian constraint transforms as

$$\overline{D}^2\psi = \frac{1}{8}\psi\overline{R} - \frac{1}{8}\psi^{-7}\overline{A}_{ij}\overline{A}^{ij} - 2\pi\psi^5\rho, \tag{2.4.51}$$

and the momentum constraint as

$$(\overline{\Delta}_L\,\beta)^i = 2\overline{A}^{ij}\,\overline{D}_j(\alpha\psi^{-6}) + 16\pi\alpha\psi^4 S^i, \tag{2.4.52}$$

where $\overline{\Delta}_L$ is the vector Laplacian. and $\overline{D}^2$ is the covariant Laplace operator associated with $\overline{\gamma}_{ij}$ These three equations are the elliptic equations that completely describe the metric, Eq. 2.4.40, [54] and all unknowns can be calculated from them. They provide the lapse and the shift vector along with the metric and extrinsic curvature.

2.4.1 Conformal Flatness Approximation and elliptic equations solved by LORENE

The LORENE code, described in detail in section 3 below, solves elliptic equations for quasiequilibrium field configurations using the conformal flatness approximation. In this approach, it is assumed that gravitational radiation has a negligible contribution towards the structure and evolution of neutron stars. Thus the initial spatial metric becomes

$$\gamma_{ij} = \psi^4\eta_{ij}, \tag{2.4.53}$$

with η_{ij} as the flat 3-metric and we get

$$ds^2 = -(\alpha^2 - \beta_i\beta^j)dt^2 - 2\beta dt dx^i + \psi^4\eta_{ij}dx^i dx^j. \tag{2.4.54}$$

The extrinsic curvature is defined as

$$K^{ij} = -\frac{1}{2\alpha}(D^i\beta^j + D^j\beta^i) = -\frac{1}{2\psi^4\alpha}\left\{\overline{\nabla}^i\alpha^j + \overline{\nabla}^j\alpha^i - \frac{2}{3}\eta^{ij}\overline{\nabla}_k\alpha^k\right\}, \tag{2.4.55}$$

where $\overline{\nabla}$ is the covariant derivative with respect to flat metric η.

In order to derive the equation that `Lorene` will solve to define the spacetime metric for a given BNS configuration, the code uses a set of familiar constraint equations from general relativity, much as one would use the divergence-free nature of a magnetic field to ensure that a given electromagnetic field configuration was self-consistent. These constraints are known as the Hamiltonian and momentum constraints, and describe the properties of a spacetime in which energy and momentum sources yield the proper curvature effects, respectively. In `Lorene`, these may be combined with a "maximum slicing" condition, tr $K = 0$, to yield a set of elliptic equations that can be solved.

Two of the three elliptic equations can be derived using the Hamiltonian constraint equation and maximal slicing:

$$\nabla^2\nu = 4\pi\psi^4(E + S) + \psi^4 K_{ij}K^{ij} - \overline{\nabla}_i\nu\overline{\nabla}^i\epsilon, \tag{2.4.56}$$

$$\nabla^2\epsilon = 4\pi\psi^4 S + \frac{3}{4}\psi^4 K_{ij}K^{ij} - \frac{1}{2}\left[\overline{\nabla}_i\nu\overline{\nabla}^i\nu + \overline{\nabla}_i\epsilon\overline{\nabla}^i\epsilon\right], \tag{2.4.57}$$

where $\nu = \ln\alpha$, $\epsilon = \ln(\psi^2\alpha)$, E is matter energy density and S is trace of the stress tensor calculated as

$$E = \Gamma_n^2(e + p) - p, \tag{2.4.58}$$

$$S = 3p + (E + p)\mathbf{U}\cdot\mathbf{U}. \tag{2.4.59}$$

where $\mathbf{U}$ is the fluid velocity in inertial frame, p is the fluid pressure, e is the fluid proper

energy density and Γ_n is the Lorentz factor between the co-orbiting observer and the Eulerian observer.

The momentum constraint gives the last elliptic equation as

$$\nabla^2 N^i + \frac{1}{3}\overline{\nabla^i}(\overline{\nabla_j})N^j = -16\pi\alpha\psi^4(E+p)U^i + 2\alpha\psi^4 K^{ij}\overline{\nabla}_j(3\epsilon - 4\nu), \tag{2.4.60}$$

with the shift vector of non-rotating co-ordinates as,

$$\mathbf{N} = \boldsymbol{\beta} + \Omega\frac{\partial}{\partial\phi}. \tag{2.4.61}$$

Chapter 3

Description of LORENE

The LORENE code [**https://lorene.obspm.fr/**] was developed by scientists at Observatoire de Paris to solve different problems in computational astrophysics including the elliptic systems that occur in the Conformal Thin Sandwich formalism [3] to describe quasi-equilibrium binary neutron star configurations. It consists of a set of C++ classes that provide tools to solve partial differential equations using multi-domain spectral methods. In this section, we will briefly describe the method used by [3] in which a system of coupled non-linear partial differential equations are solved to obtain a quasiequillibrium relativistic binary system. The fluid motion is described by considering a zero-temperature, perfect fluid EOS. The matter stress energy tensor is described as

$$T^{\mu\nu} = \rho h u^{\mu} u^{\nu} + p g^{\mu\nu}, \tag{3.0.1}$$

where ρ is rest-mass density, h is fluid specific enthalpy, u is fluid 4-velocity, p is fluid pressure and $g^{\mu\nu}$ is the metric. The first law of thermodynamics for neutron star matter is :

$$\frac{\Delta p}{e+p} = \frac{1}{h}\Delta h, \tag{3.0.2}$$

where $e \equiv \rho h - p$ is the proper fluid energy density. The specific enthalpy is defined as

$$h = \frac{e+p}{m_B n}, \tag{3.0.3}$$

where n is fluid baryon density and m_B is the mean baryon mass. A cold matter equation of state is supplied, given by

$$n = n(h), \quad e = e(h), \quad p = p(h). \tag{3.0.4}$$

LORENE can use several different kinds of EOSs for calculating the initial data; these include three types we discuss further here: polytropes, piecewise polytropes and tabulated EOS. We will discuss more EOSs in section 3.2.

3.1 Co-ordinate system and computational domains

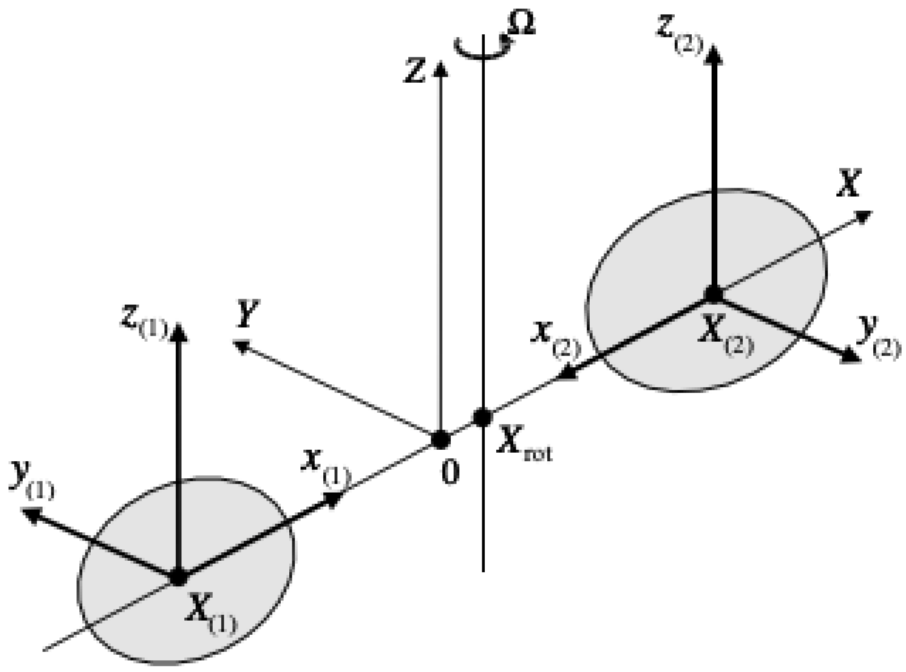

Figure 3.1: Depiction of placement of stars in LORENE[3]

The placement of stars is done in LORENE using co-orbiting Cartesian co-ordinates, where the orbital plane is at $Z = 0$, the two centers lie on the X-axis and the rotation axis lies along the Z-axis. Using these co-ordinates we can define the line element in the usual conformal decomposition involving a lapse function, shift vector, and conformal factor, as

$$ds^2 = -\alpha^2 dt^2 + \psi^4[(dX - \beta^X dt)^2 + (dY - \beta^Y dt)^2) + (dZ - \beta^Z dt)^2], \tag{3.1.5}$$

Additionally, two Cartesian coordinate systems are introduced by the code, one centered on each star and each covering all of the volume, that are used to describe the interior of the stars and the gravitational forces they each encounter (see Figure 1). The center of each star is defined at the location of maximum enthalpy h. We note to clear up the confusion that this may differ from the center-of-mass or other quantities one might typically prefer in a Newtonian calculation. LORENE divides the entire hypersurface into computational domains topologically representing spheroids. The domains are described using spherical co-ordinates (r, θ, ϕ) and extend via compactification up to $r = +\infty$. It allows for the spherical co-ordinates to adapt to the surface of each star using Eq. 74 & 75 from [3], which describe radial deformations of the spheroidal surface in terms of angular modes. For our calculations, we have used two sets of five domains, with one set of domains centered around each star. In each set, the first domain contains the center of the star and topologically represents a ball. The second domain represents a spherical shell covering the star. The surface of the star coincides exactly with the outer boundary of the second domain. The third and fourth domains also represent nested spherical shells, located outside of the surface of the stars. The fifth domain extends up to $r = +\infty$ and is mapped to a finite computational domain using compactification. The radii of different domains can be calculated as follows:

$$r = a_0[1 + P_0(\theta, \phi) + Q_0(\theta, \phi)], \tag{3.1.6}$$

is the radius of the outer boundary of the nucleus, where P_i and Q_i terms here and below

represent the odd and even Fourier modes, respectively.

$$r = a_i[-1 + P_i(\theta, \phi)] + b_i, \tag{3.1.7}$$

is the radius of the inner boundary of shell number i and

$$r = a_i[1 + Q_i(\theta, \phi)] + b_i, \tag{3.1.8}$$

where a_i and b_i are some constants and the boundary of each domain is determined in part by $P_i(\theta, \phi)$ and $Q_i(\theta, \phi)$. We have produced initial data where the domains are placed at radii having factors of 2 in spacing. For example, d_1 is placed at the surface of NS (i.e r=1), d_2 is placed at r=2, d_3 is placed at r=4 and so on. We have investigated the effect of changing domain boundaries on the quality of initial data, discussed in section 5.3

3.2 Initial conditions

`LORENE` needs to specify the following four quantities to build a quasiequilibrium binary neutron star configuration: 1) The equation of state for both stars, 2) the stellar rotation state – either irrotational or corotating, 3) the co-ordinate distance between the two stars and 4) the central enthalpies $h^c_{\langle 1\rangle}$ and $h^c_{\langle 2\rangle}$ and thus the central densities in each star. These parameters are used for computing the initial conditions for the iterative procedure. We note that while Lorene can theoretically employ different EOS models for the two stars, this is seemingly unphysical since there is assumed to be a "true" NS EOS model whose properties we've yet to determine. The initial state of the binary, prior to full relaxation, is comprised of two superposed numerical solutions for spherically symmetric, static, isolated neutron stars with the given central enthalpies. In our calculations, we have used simple polytropic EOS, piecewise polytropic EOS specified by 4 free parameters to model neutron star matter as given by [4], and tabulated EOS, discussed further below. A polytrope is defined as any region where pressure depends solely on the (rest-mass) density in a power law form: $p = K\rho^{\Gamma}$, where Γ is the adiabatic index and K is a constant.

3.2.1 Simple polytropes

The first law of thermodynamics, in relativistic form with $c = 1$, may be expressed in differential form as

$$d\left(\frac{\epsilon}{\rho}\right) = -pd\left(\frac{1}{\rho}\right), \tag{3.2.9}$$

For a single polytrope, the EOS is given as

$$p = K\rho^{\Gamma}, \tag{3.2.10}$$

with the above two equations, we can derive the following three quantities: ϵ, the "energy density" or "mass-energy density"; e, the "specific internal energy"; and h, the "specific enthalpy". The specific internal energy is given as

$$e \equiv \frac{\epsilon}{\rho} - 1, \tag{3.2.11}$$

$$\epsilon \equiv \rho(1 + e). \tag{3.2.12}$$

The specific enthalpy can be calculated as

$$h = \frac{\epsilon + p}{\rho}, \tag{3.2.13}$$

$$h = 1 + e + \frac{p}{\rho}. \tag{3.2.14}$$

At infinitesimal densities we note that

$$\lim_{\rho \to 0} h = 1, \tag{3.2.15}$$

$$\lim_{\rho \to 0} \frac{\epsilon}{\rho} = 1, \tag{3.2.16}$$

and

$$\lim_{\rho \to 0} e = 0. \tag{3.2.17}$$

On integrating the first law of thermodynamics in differential form and using the above conditions we obtain the following equations for energy density,

$$\begin{aligned}
\frac{\epsilon(\rho)}{\rho} =& -\int_0^{\rho} K\rho^{\Gamma}\left(-\frac{1}{\rho^2}\,d\rho\right),\\
\frac{\epsilon(\rho)}{\rho} =& \int_0^{\rho} K\rho^{\Gamma-2}\,d\rho,\\
\frac{\epsilon(\rho)}{\rho} =& \frac{K\rho^{\Gamma-1}}{\Gamma-1}+C,\\
\frac{\epsilon(\rho)}{\rho} =& 1+\frac{K\rho^{\Gamma-1}}{\Gamma-1},
\end{aligned} \tag{3.2.18}$$

which gives

$$\begin{aligned}
\epsilon(\rho) =& C\rho+\frac{K\rho^{\Gamma}}{\Gamma-1},\\
\epsilon(\rho) =& \rho+\frac{K\rho^{\Gamma}}{\Gamma-1},\\
\epsilon(\rho) =& \rho+\frac{p}{\Gamma-1}.
\end{aligned} \tag{3.2.19}$$

We can obtain specific internal energy as,

$$\begin{aligned}
e =& \frac{K\rho^{\Gamma-1}}{\Gamma-1},\\
e =& \frac{p}{(\Gamma-1)\rho},
\end{aligned} \tag{3.2.20}$$

giving the relation between pressure and specific internal energy as

$$p = (\Gamma-1)\rho e, \tag{3.2.21}$$

and the relation for specific enthalpy

$$h = 1+\Gamma e. \tag{3.2.22}$$

3.2.2 Piecewise polytropes

Piecewise polytropes are treated somewhat differently. We assume that there are a set of "breakpoint" densities $0 < \rho_0 < \rho_1 < \rho_2 < ...$, such that pressure can be treated as

$$p(\rho) = K_i \rho^{\Gamma_i}; \quad \rho_{i-1} \leq \rho \leq \rho_i. \tag{3.2.23}$$

We can freely determine only a single K value. We assume it is K_0 and note that the pressure being a continuous function of density requires

$$\begin{aligned} p(\rho_{i-1}) &= K_i \rho_{i-1}^{\Gamma_i}, \\ p(\rho_{i-1}) &= K_{i-1} \rho_{i-1}^{\Gamma_{i-1}}, \end{aligned} \tag{3.2.24}$$

which gives

$$K_i = K_{i-1} \rho_{i-1}^{\Gamma_{i-1} - \Gamma_i}. \tag{3.2.25}$$

To determine all other thermodynamic quantities, we use the fact that ϵ must also be continuous. We define $\epsilon_0 = \epsilon(\rho_0)$ and similarly continue for all breakpoint densities $\epsilon_i = \epsilon(\rho_i)$. From the above equations, we have

$$\frac{\epsilon}{\rho} = \frac{\epsilon_{i-1}}{\rho_{i-1}} + \frac{K_i}{\Gamma_i - 1}(\rho^{\Gamma_i - 1} - \rho_{i-1}^{\Gamma_i - 1}), \tag{3.2.26}$$

$$\begin{aligned} \epsilon &= \rho \left(\frac{\epsilon_{i-1}}{\rho_{i-1}} - \frac{K_i \rho_{i-1}^{\Gamma_i - 1}}{\Gamma_i - 1} \right) + \frac{K_i \rho^{\Gamma_i}}{\Gamma_i - 1}, \\ \epsilon &= \rho \left(\frac{\epsilon_{i-1}}{\rho_{i-1}} - \frac{K_i \rho_{i-1}^{\Gamma_i - 1}}{\Gamma_i - 1} \right) + \frac{p}{\Gamma_i - 1}, \end{aligned} \tag{3.2.27}$$

$$e = \left(\frac{\epsilon_{i-1}}{\rho_{i-1}} - \frac{K_i \rho_{i-1}^{\Gamma_i - 1}}{\Gamma_i - 1} - 1 \right) + \frac{K_i \rho^{\Gamma_i - 1}}{\Gamma_i - 1}, \tag{3.2.28}$$

$$h = \left(\frac{\epsilon_{i-1}}{\rho_{i-1}} - \frac{K_i \rho_{i-1}^{\Gamma_i - 1}}{\Gamma_i - 1} \right) + \frac{K_i \Gamma_i \rho^{\Gamma_i - 1}}{\Gamma_i - 1}. \tag{3.2.29}$$

It is convenient, following [4] to define

$$a_i \equiv \frac{\epsilon_{i-1}}{\rho_{i-1}} - \frac{K_i \rho_{i-1}^{\Gamma_i - 1}}{\Gamma_i - 1} - 1, \tag{3.2.30}$$

so that we find

$$\begin{aligned} \epsilon =& \rho(1 + a_i) + \frac{p}{\Gamma_i - 1}, \\ e =& a_i + \frac{K_i \rho^{\Gamma_i - 1}}{\Gamma_i - 1} = a_i + \frac{p}{(\Gamma_i - 1)\rho}, \\ h =& 1 + a_i + \frac{K_i \Gamma_i \rho^{\Gamma_i - 1}}{\Gamma_i - 1} = 1 + a_i + \frac{\Gamma_i p}{(\Gamma_i - 1)\rho}. \end{aligned} \tag{3.2.31}$$

Finally, we note that

$$\frac{\epsilon_i}{\rho_i} = \frac{\epsilon_{i-1}}{\rho_{i-1}} + \frac{K_i}{\Gamma_i - 1}\left(\rho_i^{\Gamma_i - 1} - \rho_{i-1}^{\Gamma_i - 1}\right). \tag{3.2.32}$$

There are over 40 approximate, piecewise polytropic equations of states listed in [4] that may be used to model many well-known physically motivated EOS models (i.e AP1-4[55], SLy[56], MS1-2[57], etc). The particular values of adiabatic indices and pressure at the first break point, corresponding to the models for which we have constructed initial data are shown in Table 3.1

EOS	$\log(p_1)$	Γ_1	Γ_2	Γ_3
SLy	34.384	3.005	2.988	2.851
AP3	34.392	3.166	3.573	3.281
AP4	34.269	2.830	3.445	3.348
WFF1	34.031	2.519	3.791	3.660
MPA1	34.495	3.446	3.572	2.887
MS1	34.858	3.224	3.033	1.325
MS1b	34.855	3.456	3.011	1.425

Table 3.1: List of EOSs and their free parameter values. The units for p_1 are dyne/cm^2.

The high density pressure profile for these models is calculated by stitching together three polytropic regions having breaks at $\rho_1 = 10^{14.7}$g/cm^3 and $\rho_2 = 10^{15}$g/cm^3. As a result, for $\rho \geq \rho_0$ (see below) we obtain

$$p(\rho) = K_i \rho^{\Gamma_i}, \quad \text{for } \rho_{i-1} \leq \rho \leq \rho_i. \tag{3.2.33}$$

The free parameters used to model the NSs are the adiabatic indices in the three regions $\Gamma_1, \Gamma_2, \Gamma_3$ and the pressure at the density between the first two regions. To make sure we

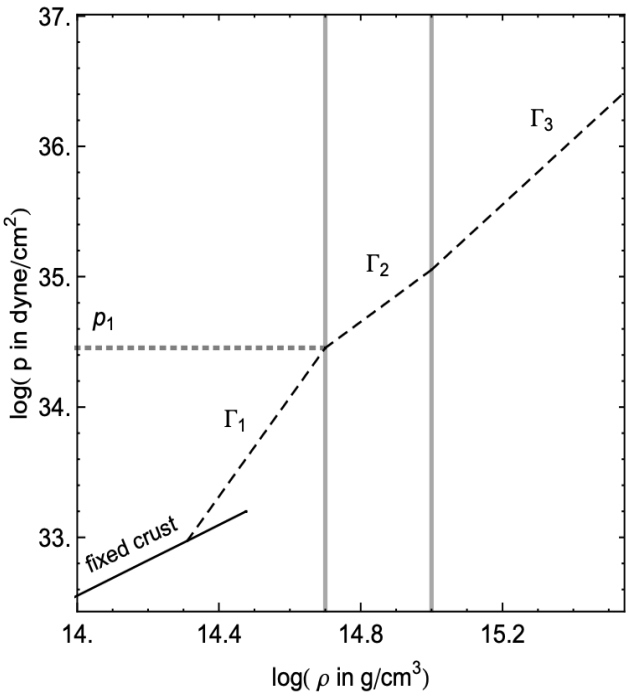

Figure 3.2: The high density region is parameterized using adiabatic indices $\Gamma_1, \Gamma_2, \Gamma_3$ and pressure p_1 at the first dividing density ρ_1 [4].

treat the low density fluid near the surface of the star, admittedly not resolved in great detail in our spectral scheme, consistently across all of the piecewise polytropic equations of state we consider, we adopt a "crust model" for the low density crust region derived from the SLy EOS model. In general, there will be very few if any collocation points for which the local densities are sufficiently small to make use of these values, but for consistency's sake, we use these values to specify the local pressure as $p = K_i \rho^{\Gamma_i}$ for all densities between ρ_{i-1} and ρ_i.

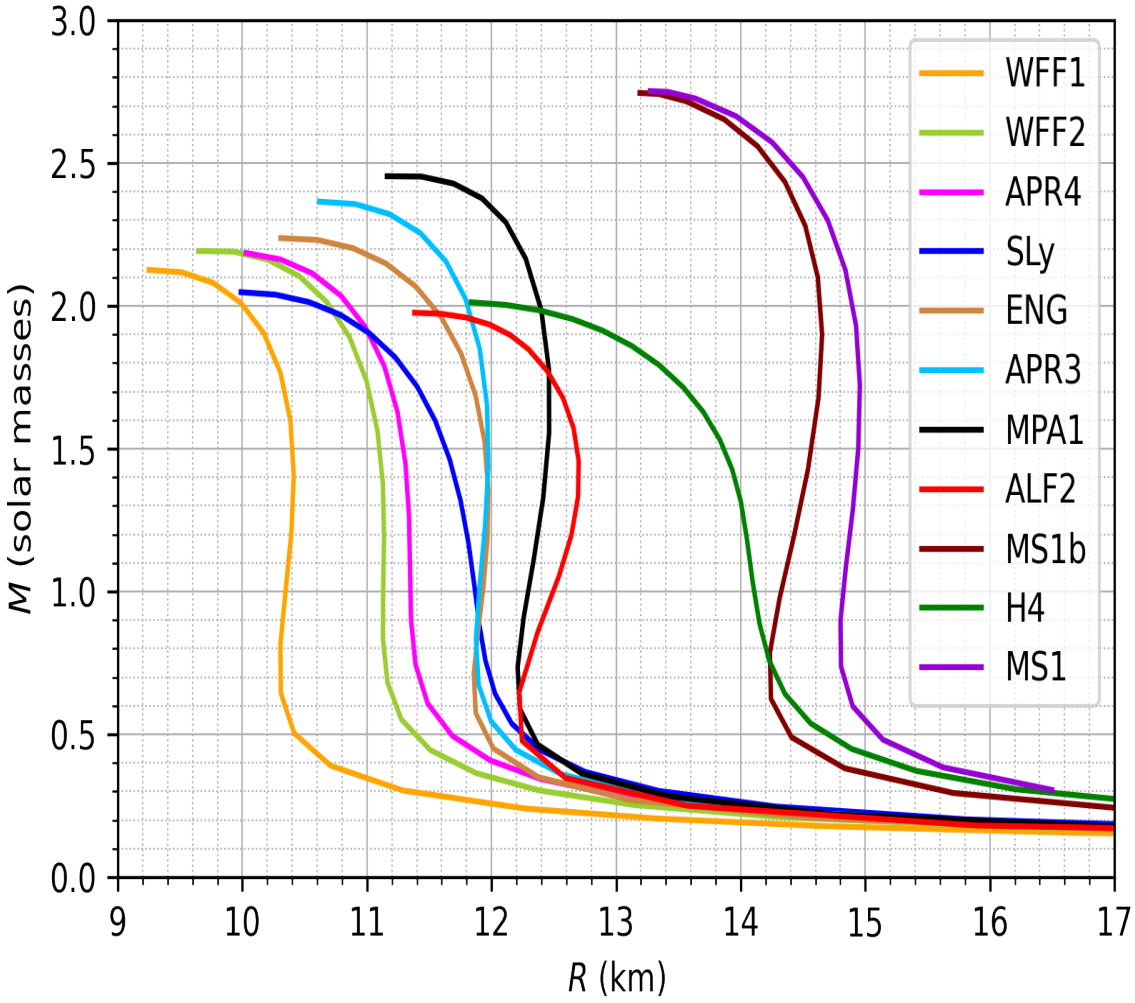

Figure 3.3: Mass versus radius variation for different models described in [4]

K_i	Γ_i	ρ_i
6.80110×10^{-9}	1.58425	2.44034×10^{7}
1.06186×10^{-6}	1.28733	3.78358×10^{11}
5.32697×10^{1}	0.62223	2.62780×10^{12}
3.99874×10^{-8}	1.35692	-

Table 3.2: List of values of K, density and adiabatic indices used to model the low density region for piecewise polytropes.

The transition from the crust model to the piecewise polytropic model is defined to occur at the density ρ_0 where the highest-density "crust" component yields the same pressure as the

first of the piecewise polytropic segments (such an overlap is guaranteed for any $\Gamma_1 \gtrsim 1.36$).

3.3 The Tolman-Oppenheimer-Volkov (TOV) equation

The Tolman-Oppenheimer-Volkov (TOV) equation for NS structure takes the following form in these units (again with $G = c = 1$):

$$\frac{dP}{dr} = -\frac{1}{r^2}(\epsilon + P)(m + 4\pi r^3 P)\left(1 - \frac{2m}{r}\right)^{-1}. \tag{3.3.34}$$

Here, r is the *circumferential radius*, which accurately measures distances in the angular direction for the NS, but *not* in the radial direction. The mass m satisfies

$$\begin{aligned} \frac{dm}{dr} &= 4\pi r^2 \epsilon \\ M &= \int_0^R 4\pi r^2 \epsilon \; dr. \end{aligned} \tag{3.3.35}$$

To find an equation for the density gradient, we may write

$$\frac{d\rho}{dr} = \frac{(dP/dr)_{TOV}}{dP/d\rho} = \frac{(dP/dr)_{TOV}}{K_i \Gamma_i \rho^{\Gamma_i - 1}}, \tag{3.3.36}$$

where every quantity on the RHS may be determined as a function of ρ and r.

3.3.1 Schwarzschild vs. isotropic metrics

The standard TOV equation derivation assumes that the metric takes the following form, known as the Schwarzschild metric:

$$ds^2 = \alpha^2 \; dt^2 - \left(1 - \frac{2m}{r}\right)^{-1} \; dr^2 - r^2(d\theta^2 + \sin^2\theta \; d\phi^2). \tag{3.3.37}$$

Here, r is the circumferential radius, since angular displacements of angle $d\xi$ represent proper distances given by $r \; d\xi$, and thus the proper circumference of a circle is $2\pi r$. The value at the surface is the circumferential (or areal) radius R. The radial proper distance measurement is

different. There, we find

$$r_{prop;rad} = \int_0^r \frac{dr}{\sqrt{1-\frac{2m}{r}}} > r. \tag{3.3.38}$$

If you think of the classic "funnel" model of a black hole or neutron star, the radial dimension deforms out of the plane, and distances are longer in that direction. To determine the proper radial distance for a neutron star, we can integrate the equation above as part of our ODE setup.

Lorene uses a different metric, known as an isotropic conformal metric:

$$ds^2 = \alpha^2\ dt^2 - [\psi(\hat{r})]^4(d\hat{r}^2 + \hat{r}^2[d\theta^2 + \hat{r}^2 d\phi^2]). \tag{3.3.39}$$

The function $\psi(\hat{r})$ is known as the *conformal factor* of the metric (α is known as the *lapse function*, but we don't need to worry about that here). Comparing the expressions, we find the following equivalences:

$$\begin{aligned} \text{radial}: \quad dr_{prop;rad} &= \frac{dr}{\sqrt{1-\frac{2m}{r}}} = \psi^2\ d\hat{r}, \\ \text{angular}: \quad r &= \psi^2 \hat{r}. \end{aligned} \tag{3.3.40}$$

To actually solve for the conformal factor, we divide the radial expression by the angular one:

$$\frac{d\hat{r}}{\hat{r}} = \frac{dr}{\sqrt{r^2-2mr}}, \tag{3.3.41}$$

where we make sure that as $r \to \infty$, the two distance measures agree up to an additive constant. Setting $m = M$ constant in the exterior, we find for $r \geq R$

$$\begin{aligned} \hat{r} =& \left(\frac{\sqrt{r}+\sqrt{r-2M}}{2}\right)^2, \\ r =& \hat{r}\left(1+\frac{M}{2\hat{r}}\right)^2, \\ R =& \hat{R}\left(1+\frac{M}{2\hat{R}}\right)^2, \\ \psi =& 1+\frac{M}{2\hat{r}}. \end{aligned} \tag{3.3.42}$$

The baryon mass differs from the gravitational mass in two respects. First, we count only the rest-mass density ρ, not the energy density ϵ. Second, we have to account for how the space-time metric measures volumes. As a result, we find the following expression:

$$M_b = \int_0^R \frac{4\pi r^2 \rho}{\sqrt{1-\frac{2m}{r}}}\, dr. \tag{3.3.43}$$

3.4 Description of one step

LORENE begins each step using first an integral of the motion, derived by assuming a quasiequilibrium configuration, with fluid motion described as either corotational or irrotational. It is given by

$$H + \nu - ln\,\Gamma_0 + ln\,\Gamma = \text{constant}, \tag{3.4.44}$$

with

$$H = \ln h, \tag{3.4.45}$$

$$\nu = \ln \alpha, \tag{3.4.46}$$

with α the lapse function and Γ_0 the Lorentz factor between a co-orbiting observer and an Eulerian observer. The value of Γ is calculated by taking the negative dot product between the fluid velocity and velocity of the co-orbiting observer and is the Lorentz factor between the fluid and a co-orbiting observer. The specified coordinate separation of the two neutron stars is defined with respect to the *maximum enthalpy within each star*. The gradient of Eq. 3.4.44 above is taken along the X direction to determine the value of the orbital angular velocity Ω and the X co-ordinate of rotation axis X_{rot}. This leads to two equations for each star

$$\frac{\partial}{\partial X}\ln\Gamma_0\Big|_{(X_{\langle a\rangle},0,0)} = \frac{\partial}{\partial X}\ln(\Gamma+\nu)\Big|_{(X_{\langle a\rangle},0,0)} \quad a = 1, 2, \tag{3.4.47}$$

where Γ_0 is given by

$$\ln\Gamma_o = -\frac{1}{2}\left\{1 - \frac{\psi^4}{N^2}\left[[\Omega Y + N^X]^2 + [\Omega(X - X_{rot}) - N^Y]^2 + N^{Z\,2}\right]\right\}, \tag{3.4.48}$$

where ψ is the conformal factor. After this, an elliptic equation for the velocity potential is solved. This equation is derived in the next section.

3.5 Equations for the fluid with a conformally flat 3 metric

We can derive the elliptic equation for the flow by assuming the existence of an irrotational, relativistic velocity potential, such that

$$\mathbf{w} = \nabla\Psi, \tag{3.5.49}$$

where Ψ is the velocity potential of irrotational flow and $\mathbf{w}$ is the comomentum 1-form given by $\mathbf{w} = h\mathbf{u}$. Combined with our equation of motion, we find

$$\frac{n}{h}\nabla\cdot\nabla\Psi + \nabla\Psi\cdot\nabla\left(\frac{n}{h}\right). \tag{3.5.50}$$

The Lorentz factor between the fluid and Eulerian observer is given by

$$\Gamma_n = \left(1 + \frac{1}{h^2}\mathbf{D}\Psi\cdot\mathbf{D}\Psi\right)^{1/2}, \tag{3.5.51}$$

$\mathbf{D}$ being the covariant derivative with respect to the 3 metric of spatial hypersurface Now, the 3+1 form of Eq. 3.4.40, the continuity equation, can be written as

$$n\mathbf{D}\cdot\mathbf{D}\Psi + \mathbf{D}n\cdot\mathbf{D}\Psi = h\Gamma_n\mathbf{U}_0\cdot\mathbf{D}n + n\left(\mathbf{D}\Psi\cdot\mathbf{D}\ln\frac{h}{\alpha} + \mathbf{U}_0\cdot\mathbf{D}\Gamma_n\right) + nhK\Gamma_n, \tag{3.5.52}$$

where $\mathbf{U}_0$ is orbital 3-velocity. The Lorentz factor between the co-orbiting observer and the Eulerian observer for a conformally flat metric and irrotational motion can be written as

$$\Gamma_n = \left(1 + \frac{1}{\psi^4 h^2}\eta^{ij}\overline{\nabla}_i\Psi\overline{\nabla}_j\Psi\right)^{1/2}, \tag{3.5.53}$$

and the fluid 3-velocity is

$$U^i = \frac{1}{\psi^4 \Gamma_n h} \overline{\nabla}^i \Psi. \tag{3.5.54}$$

LORENE considers the enthalpy as a function of baryon density and introduces a thermodynamic coefficient using the definition

$$\zeta = \frac{d \ln H}{d \ln n}. \tag{3.5.55}$$

We can rewrite the continuity Eq. 3.5.52 by replacing the gradient of baryon density with the gradient of enthalpy as,

$$\zeta H \nabla^2 \Psi + \overline{\nabla}^i H \overline{\nabla}_i \Psi = \psi^4 h \Gamma_n U_0^i \overline{\nabla}_i H + \zeta H (\overline{\nabla}^i \Psi \overline{\nabla}_i (H - \epsilon) + \psi^4 h U_0^i \overline{\nabla}_i \Gamma_n). \tag{3.5.56}$$

Let us define the constant (translational) velocity field as

$$W^i = \psi^4 h \Gamma_n U_0^i. \tag{3.5.57}$$

We can rewrite Eq. 3.5.56 as

$$\begin{aligned} &\zeta H \nabla^2 \Psi_0 + \left[(1 - \zeta H) \overline{\nabla}^i H + \zeta H \overline{\nabla}^i \epsilon \right] \overline{\nabla}_i \Psi_0 = \\ &(W^i - W_0^i) \overline{\nabla}_i H + \zeta H \left(W_0^i \overline{\nabla}_i (H - \epsilon) + \frac{W^i}{\Gamma_n} \overline{\nabla}_i \Gamma_n \right), \end{aligned} \tag{3.5.58}$$

where

$$\Psi = \Psi_0 + \eta W_0^i x^j, \tag{3.5.59}$$

and W_0^i is the central value of W^i. LORENE solves the above equation using spectral methods as described in [3]. After this step, new thermodynamic values for density, pressure and specific energy are computed using the EOS and enthalpy. Next, the matter energy density and trace of the stress energy tensor are calculated to solve the Einstein equations.

Chapter 4

Modified version of LORENE

In this Chapter, we describe our modifications to the publicly released `Lorene` code to increase the stability of its iterative scheme, and to allow for the generation of close binaries of unequal mass beyond those capable of being produced stably by the public code. All modifications described herein have been shared with the community at large. In Appendix B, we discuss the structure of the different routines used to generate quasiequilibrium binary sequences, as well as the contents of the parameter files used to set up a given run.

4.1 Generating unequal mass ratios far from unity

`LORENE` uses a complicated relaxation scheme and historically has had multiple failure modes that can cause a run designed to generate initial data to crash prior to converging to the desired configuration. For very unequal-mass binary neutron star systems, one of the key culprits is a flaw in the numerical methods found in the current releases of the code. The safest parameter choices are low-mass binaries and mass ratios either equal or close to unity. In solving simultaneously for the angular velocity and rotation axis of the system, Eq. 3.4.47, `Lorene` uses a 2-d secant method. While this is a standard numerical method for use in these situations, the particular equations as implemented are poorly chosen for stability as shown in Fig. 4.2, and can generate both divide-by-zero errors as well as discontinuous changes in the sign of the terms. Even when the code continued to generate configurations without crashing,

the center of mass and rotational axis often had a highly oscillatory behavior as shown in Fig. 4.1.

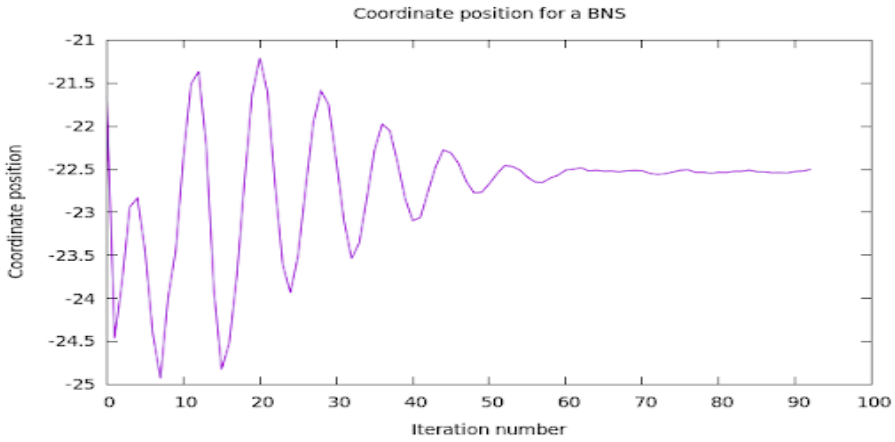

Figure 4.1: Oscillatory behavior of center of mass co-ordinate before converging to a constant value for unequal mass configurations.

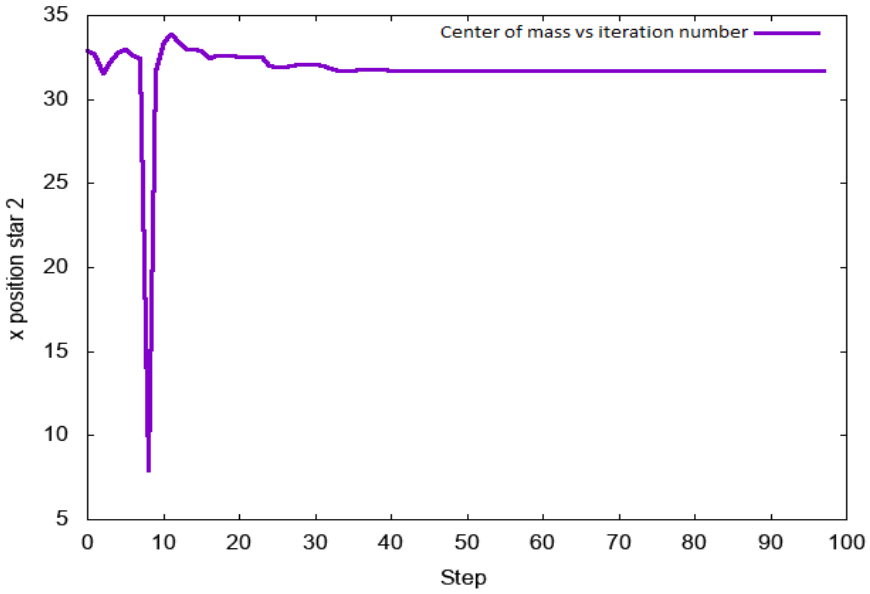

Figure 4.2: Center of mass of one of the stars versus iteration number. It diverges from the equilibrium making the code unstable.

To describe the particular issues associated with the choice of function on more detail, we note that the code estimates the value of system's angular velocity Ω for each star *separately*, and then iteratively forces the difference to zero to achieve a consistent value. The angular

velocity values for each star are obtained from equation Eq. 3.4.47, expanded as:

$$\Omega^2_{(a)} = \frac{\frac{d\xi}{dX_a}}{[\frac{1}{2}(\frac{d\mu}{dX_a}\lambda + \mu\frac{d\lambda}{dX_a}) + \mu\lambda\frac{d\xi}{dX_a}]}, \tag{4.1.1}$$

where

$$\mu = \frac{A^2}{N^2}, \tag{4.1.2}$$

$$\xi = \nu + ln\Gamma, \tag{4.1.3}$$

$$\lambda = [(Y + \frac{\beta^X}{\Omega})^2 - ((X - X_{rot}) - \frac{\beta^Y}{\Omega})^2 + (\frac{\beta^Z}{\Omega})^2] \tag{4.1.4}$$

where a=1,2 for both the stars. Please refer to Appendix A for the detailed derivation. Unfortunately, these functional choices for each star require a division by a term that can change sign (as seen in Eq. 4.1.1), leading to non-continuous behavior of the function whose root the routine attempts to determine. To alleviate this problem, we have found that taking the reciprocal of Ω^2 for each star and setting those equal to each other yields well-defined, continuous results for all reasonable parameter choices (see Sec. 4.2.1 for demonstrations of how Lorene convergence was enabled by this code modification).

4.2 Higher-mass configurations and close separations

As a BNS system is driven to inspiral by gravitational radiation, the baryon mass remains conserved during the evolution. `LORENE` computes evolutionary sequences of BNS by computing configurations for a specified set of baryon masses. The computation of a sequence is initiated from the central enthalpies of the stars and the initial separation between them as input parameters. Since the baryon mass is an increasing function of the central enthalpy, an iterative procedure is implemented to reach a given final baryon mass for each star. During

this procedure, the central enthalpy is multiplied by a factor given by

$$\eta = \left(\frac{2+\xi}{2+2\xi} \right)^{1/4}, \tag{4.2.5}$$

where ξ is the relative difference between the actual baryon mass $M_B^{\langle 1 \rangle J}$ and the desired baryon mass $M_B^{\langle 1 \rangle}$: $\xi = M_B^{\langle 1 \rangle J}/M_B^{\langle 1 \rangle} - 1$. The factor η tends to one on convergence.

As mentioned in the previous section, LORENE attempts to estimate the values of X_{rot} and Ω for the BNS system. For high-mass binaries that are initially too far from equilibrium, this procedure leads to fluctuations of the estimates of X_{rot} and the center of mass of the system at the beginning of the iterative procedure, with the possibility that a given configuration will be unstable and rapidly lead to non-convergence. We modified the driver code routines to include a mass scanning routine to compute stable, high-mass BNS systems by designing an iterative procedure to reach a given high-mass, low-mass-ratio configuration ($q < 1$) having started with both the stars at a low baryon mass and stable mass ratio. We modified the code to increase the baryon mass to the desired value $M_B^{\langle 1 \rangle}$ in a number of steps (which are user-modified) and slowly relax the stars to the given high mass configuration. Thus when the stars reach higher masses, they are already much closer to equilibrium, and the routine is much more stable as a result. The failure mode is easily classified, if not completely intuitive. When configurations are moved inward, any underdamping in the relaxation scheme tends to produce overshooting as the stars settle into their new equilibrium configuration corresponding to the new tidal gravity forces. Should either NS instantaneously find its outer surface having exceeded the Roche lobe radius at a given iteration step, the response is to keep growing unstably, eventually leading to numerical non-convergence. It is mistaken to describe this process as "Roche lobe overflow" or other terms describing dynamical binaries, since we note that this is an elliptic-equation relaxation scheme and there is no time-evolution whatsoever. We also implemented a stepping routine to achieve a small binary separation between the stars. The routine is automated to begin at a relatively wide binary configuration and then gradually shrink the binary separation until the system reaches the tidal stability limit that would mark the onset of a merger. A graphical representation of achieving a BNS configuration

for high-mass binaries at a low separation distance is shown in Fig. 4.3.

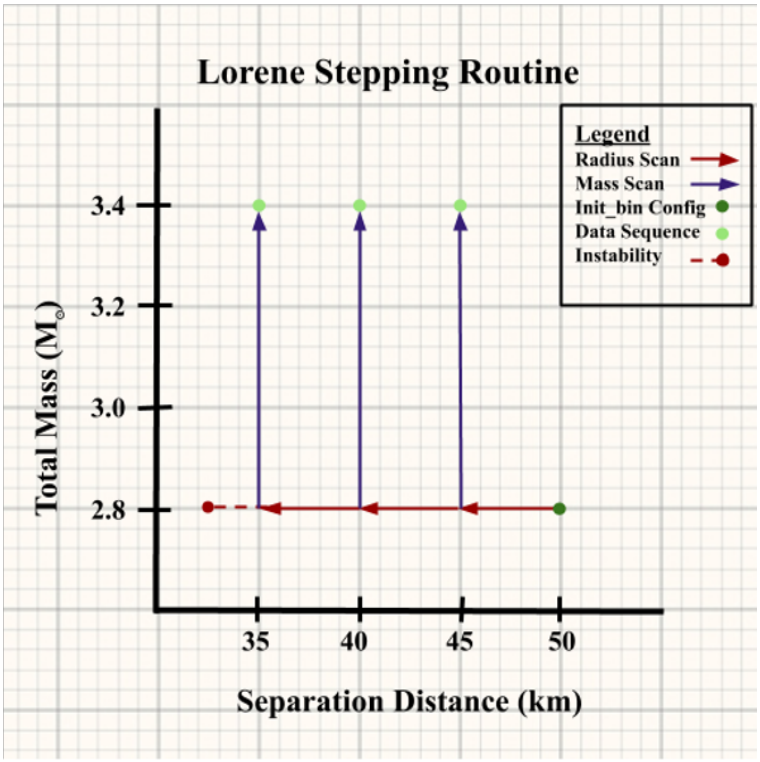

Figure 4.3: The mass and separation scanning routine as employed by the updated version of `LORENE`. First, the binary separation is gradually reduced until we reach a desired value for a low-mass configuration. Next, we gradually increase the masses at fixed separation until the desired quasi-equilibrium binary configuration is achieved. To compute a binary configuration at smaller separations, we go back to the final low-mass configuration and repeat the process from that point again.

As discussed above, the difference in central enthalpy for the NS is the parameter used as a convergence factor as described in the parameter file `parcoal_seq.d`. Figure 4.4 shows the evolution of this value, called `diff_ent` within the `Lorene` code, for a typical BNS configuration with simple polytropic EOS and $1.4M_\odot$ gravitational mass. The configuration eventually converges after around 130 steps.

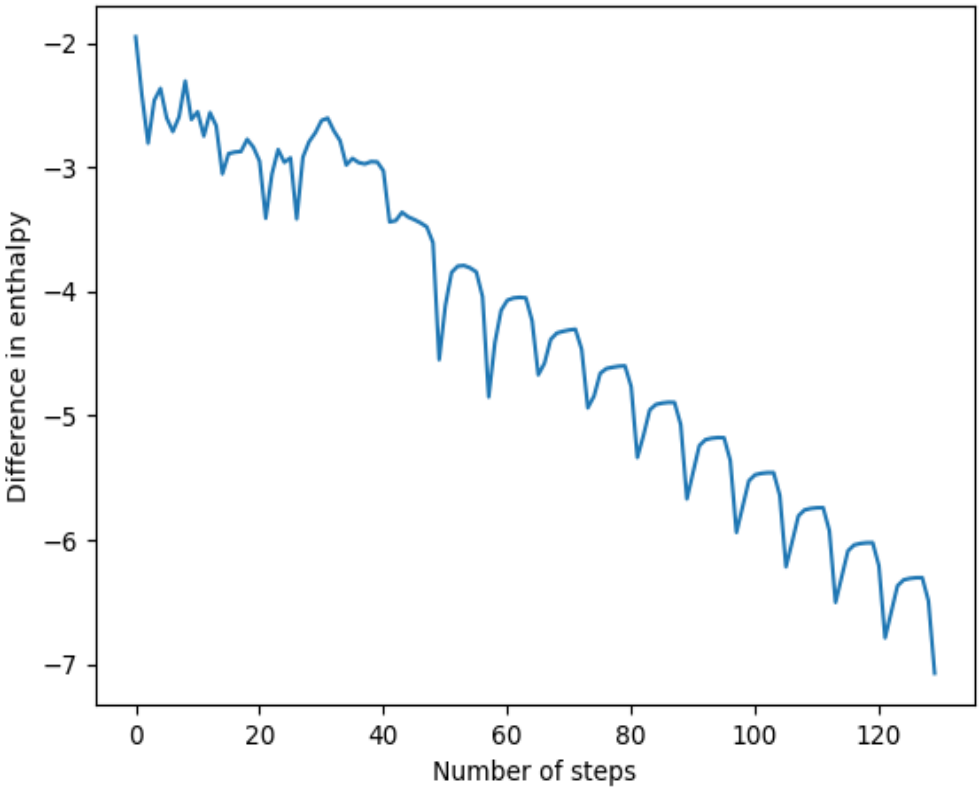

Figure 4.4: Step-over-step difference in central enthalpy for the two NS for an equal-mass pair of polytropic with $\gamma = 2$ NS during a run that successfully generates a quasi-equilibrium configuration. This error measure produces a somewhat underdamped decaying exponential over time, eventually falling below the step-over-step tolerance condition.

4.2.1 Demonstration of Lorene stepping routine to produce a higher-mass configuration at close separations

In this section, we will demonstrate the improvements seen in LORENE after incorporating our modifications. We started with a BNS configuration having $M_1 = 1.2\mathrm{M}_\odot$ and $M_2 = 1.0\mathrm{M}_\odot$ having FPS[58] EOS. The previous version(before fixes) of LORENE did not converge for the said configuration at 50 kms as shown in Figure 4.5b. It failed to find a root of Eq. 4.1.1. However modified LORENE successfully generates a quasi-equilibrium configuration at 50kms and 45kms separation as shown in Figure 4.5a

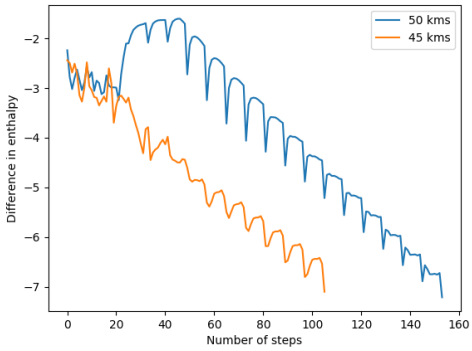

Figure 4.5a: Step-over-step difference in central enthalpy for the two NS for $M_1 = 1.2\mathrm{M}_\odot$ and $M_2 = 1.0\mathrm{M}_\odot$ with a FPS piecewise polytropic EOS at 45kms and 50kms separation. This run produces a stable quasi-equilibrium configuration using the new modified version of LORENE

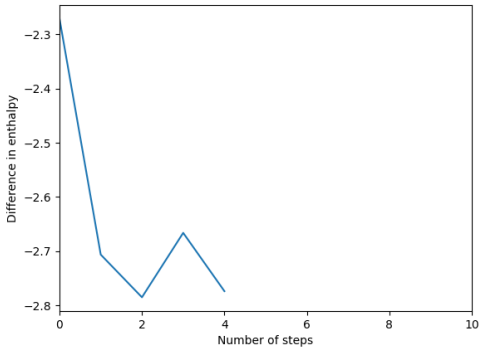

Figure 4.5b: Step-over-step difference in central enthalpy for the two NS for $M_1 = 1.2\mathrm{M}_\odot$ and $M_2 = 1.0\mathrm{M}_\odot$ with a FPS piecewise polytropic EOS and 50kms separation. This run fails to produce a stable quasi-equilibrium configuration using the older version of LORENE

Chapter 5

Results

5.1 Updated Lorene

We are able to produce initial data (ID) for various EOSs and unequal mass ratios using both our new secant method fix and the mass and separation scanning routines. Our data, as well as all of the changes to the publicly released `Lorene` code, are fully documented, and released on our public BNS Initial Data Repository, (`https://ccrgpages.rit.edu/~jfaber/BNSID/Data/`) for public use.

A typical procedure to develop initial data for a BNS configuration using `LORENE` involves specifying the central enthalpy to generate initial mass and radius of both stars individually. We have developed a TOV equation solver, separately, to determine the central enthalpy by using radius and/or mass as inputs for the neutron stars with a given equation of state (for polytropes, both may be specified and K needs to be determined as well; for piecewise and tabulated models, one may specify either the radius or mass and then determine the other). Using the enthalpy, an initial configuration is generated that is used as the input for the coalescence routine. We have shown an initial output of `LORENE` in figure 5.1 for an unequal mass binary with $M_1 = 2.0M\odot$ and $M_2 = 1.4M_\odot$, thus $q = 0.7$, modeled with an SLy EOS at a separation of 50km.

An iterative step for the coalescence routine begins with calculating the position of rotational

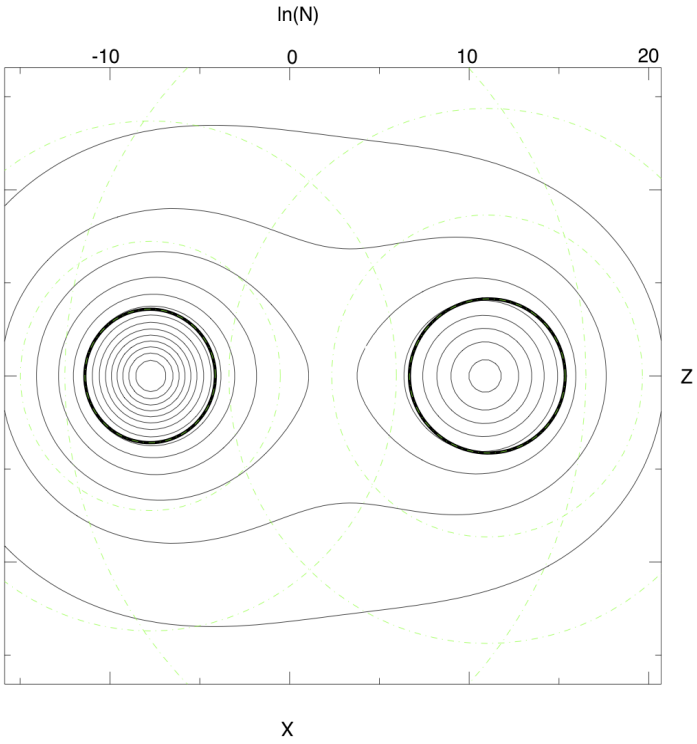

Figure 5.1: Initial output from Lorene for a BNS system with an unequal mass ratio of q= 0.7 and total mass of 3.4 $M_{\odot}$. The black curves show isocontours of the lapse function in the X-Z plane, one of the metric field quantities calculated by the code.

axis and angular velocity, while at the same time making sure that the enthalpy is maximized at both the stellar centers. Using this routine, a BNS configuration is set up as described in chapter 3. We are able to produce initial data for piecewise polytropes for mass ratios from unity down to 0.7, and a total combined gravitational mass of up to $3.4M_{\odot}$ for the binary. We observed that for EOSs with larger maximum mass (AP3, AP4, MS1, MS1b, WFF1, MPA1, SLy) we are able to produce ID of single NSs having higher masses ($M_{\odot} \geq 2$). The initial data files generated by `LORENE` are used as input by the `Einstein Toolkit` for creating dynamical simulations.

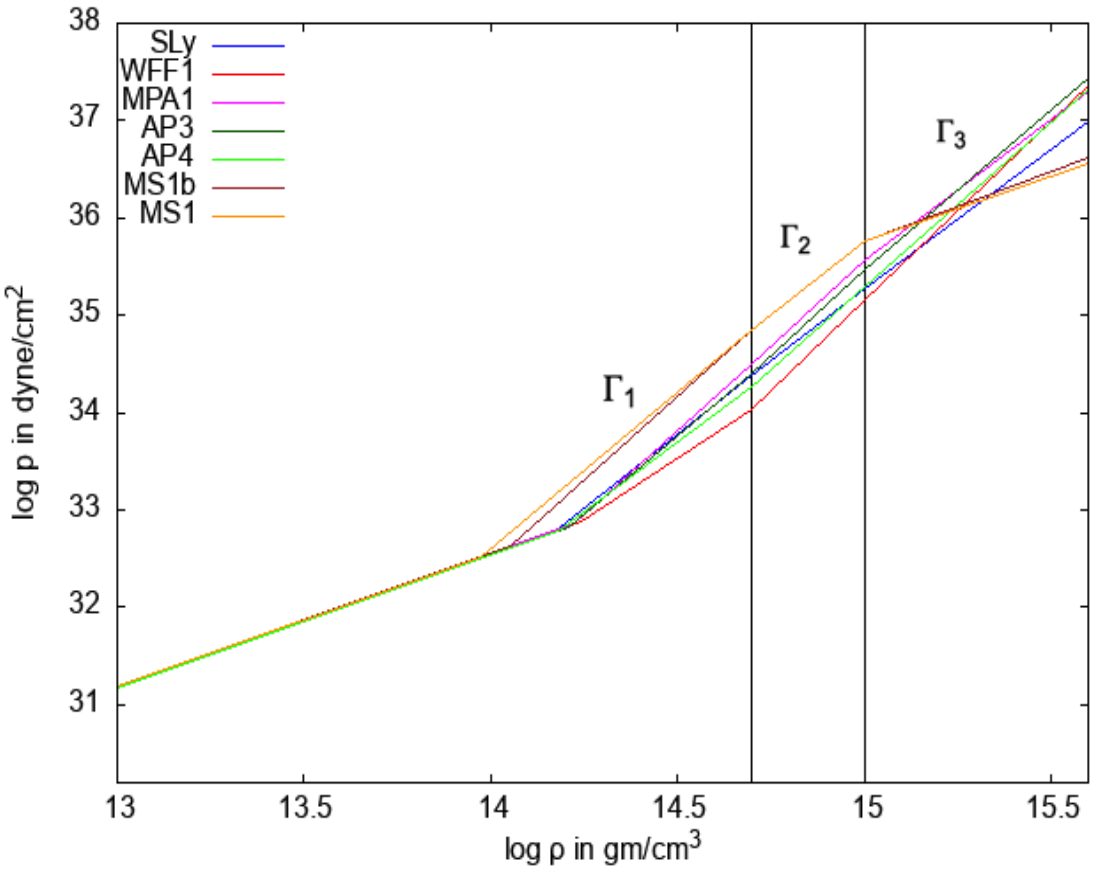

Figure 5.2: Pressure versus density plot for piecewise polytropic EOSs included in our publicly released Initial Data library, available at (`https://ccrgpages.rit.edu/~jfaber/BNSID/Data/`.

The following list details the piecewise polytropic EOS models and component masses of the different configurations included in the initial data library published at `https://ccrgpages.rit.edu/~jfaber/BNSID/Data/`. Parameters for each model are listed in Table 3.1. The pressure versus density plot for various models is shown in Fig. 5.2. The masses are in units of $M_\odot$. We produced data from initial separations starting at 50km, gradually shrinking the binary separation in each case by steps of 2.5km until the system reached the tidal stability limit that would mark the onset of a merger.

$$
\begin{aligned}
\text{SLy} &: 1.4+1.4,\ 1.6+1.4,\ 1.8+1.4,\ 2.0+1.4 \\
\text{AP3} &: 1.4+1.4,\ 1.6+1.4,\ 1.8+1.4,\ 2.0+1.35,\ 2.0+1.4 \\
\text{AP4} &: 1.4+1.0,\ 1.4+1.4,\ 1.5+1.5,\ 1.6+1.08,\ 1.6+1.4, \\
&\quad 1.7+1.14,\ 1.8+1.215,\ 1.8+1.4,\ 1.9+1.2825, \\
&\quad 2.0+1.35,\ 2.0+1.4 \\
\text{MPA1} &: 1.4+1.4,\ 1.6+1.4,\ 1.8+1.4,\ 2.0+1.4 \\
\text{MS1} &: 1.4+1.4,\ 1.6+1.4,\ 1.8+1.4,\ 2.0+1.4, \\
\text{MS1b} &: 1.4+1.4,\ 1.6+1.4,\ 1.8+1.4,\ 2.0+1.4 \\
\text{WFF1} &: 1.4+1.4,\ 1.6+1.4,\ 1.8+1.4,\ 2.0+1.4
\end{aligned}
$$

5.2 Tabulated EOS

Our ID library also includes BNS configurations for NS with tabulated EOS taken from **https://stellarcollapse.org**, developed by [6] and [8]. The finite-temperature tables provide thermodynamic quantities as a function of three variables: the electron fraction Y_e (ratio of the number density of charged baryons to total baryon density), the rest mass energy density (ρ), and temperature (T). The nuclear matter is assumed to consist of photons, alpha particles, protons, neutrons, electrons and positrons. The high-density region utilizes the liquid-drop model and the low-density region assumes nuclear statistical equilibrium with interpolation to

achieve smoothness.

As thermodynamic quantities, the pressure and specific internal energy are both dependent on the three variables, ρ , T and Y_e, but initial data configurations are generally assumed to be one-dimensional, so we have to slice the 3-dimensional table two times in order to correlate pressure and specific internal energy.[1] The first slicing condition is the beta-equilibrium condition, enforcing chemical equilibrium of beta decay and inverse beta decay, which constrains the electron fraction. The condition is given by

$$Y_e(T, \rho) = Y_e : (\mu_e + \mu_p - \mu_n)|_{(T,\rho)} = 0, \tag{5.2.1}$$

where μ_e, μ_p and μ_n are chemical potentials of electrons, protons and neutrons respectively. After this step, the number of independent parameters is reduced to 2 (ρ, T). The second slicing condition is achieved by constraining the temperature to be "cold", which is achieved numerically by choosing a constant value representing the lowest tabulated temperature present in the data, typically either 0.01 or 0.1 MeV. Using these two slicing conditions, we can express the pressure and specific energy as

$$p = p(\rho), \quad \epsilon = \epsilon(\rho). \tag{5.2.2}$$

Therefore the number of independent variables has been reduced to one and the 1D table can be read by `LORENE`.

5.3 Verification of initial data

5.3.1 Conservation of Hamiltonian constraints

The Einstein equations, decomposed using the 3+1 decomposition, consist of a set of evolution equations and constraint equations as shown in Eqs. 2.4.51 and 2.4.52. If the spatial metric and the extrinsic curvature satisfy the constraint equations at time $t = 0$ and are advanced

[1] The routines to slice the tables have been developed by our collaborator Lorenzo Sala from the University of Trento.

forward in time using the evolution equations, then they should satisfy the constraint equations at all later times, evaluating to zero in absence of numerical error. Therefore, we can test the quality of initial data based on how well the Hamiltonian constraint is conserved, and use any violations to measure the accuracy of our initial data.

We use the Baikal thorn[2] in the `EinsteinToolkit` to calculate constraint violations. Baikal defines the Hamiltonian constraint using Equation 13 of [59], given as:

$$\mathcal{H} = \frac{2}{3}K^2 - \overline{A}_{ij} - \overline{A}^{ij} + e^{-4\phi}(\overline{R} - 8\overline{D^i}\phi\overline{D}_i\phi - 8\overline{D}^2\phi) - 16\pi\rho, \tag{5.3.3}$$

where e^{ϕ} is a conformal factor. We vary different parameters in `LORENE`, including the spectral resolution, number of domains, and the convergence factor on the iteration-by-iteration change in the central enthalpy to study the violation of the Hamiltonian constraint for different models for the equation of state that include simple polytropes, piecewise polytropes, and tabulated EOS. In each case, we assume NS with gravitational mass $1.32\mathrm{M}_{\odot}$ and a separation of 50 km. We present our results in the following section.

5.3.1.1 Changing the spectral resolution

We change the spectral resolution, by increasing the number of points in the radial (nr), theta (nt) and phi (np) directions (this also represents increased spatial resolution as well, but for spectral decompositions, smooth functions should converge much more rapidly towards "exact" values than the power-law convergence one expects using methods like finite differencing). We use the following values:

Resolution	Radial	Theta	Phi
low resolution	9	7	4
medium resolution	49	17	16
high resolution	49 or 63	33	32

Table 5.1: Different Spectral resolutions used for analysing the Hamiltonian Constraint Violations

[2]"Thorns" in the language of the `EinsteinToolkit` project are packages of routines that can be included in a compiled version of the code should the functionality they provide be desired for a particular simulation.

The parameter choices for spectral resolution are chosen such that $nr \geq nt > np$. The number of points in the phi direction need to work well in a fast Fourier transform (FFT), in factors of 2 and 3 whenever possible. The number of points is the theta direction is given by $nt = np+1$ in nearly all cases. For our models, the theta parameter only covers half of the range due to vertical symmetry used by `LORENE` – only points above the equatorial plane are calculated, with symmetry conditions used to extend the configuration to its mirror image below the plane. The number of points in the radial direction is supposed to be an "FFT number+1". Runs with higher spectral resolution generally take longer to converge to a stable configuration. In some cases, increased resolution can actually over-resolve the cusps that form on the inner side of both the stars and can be problematic for configurations close to the stability limit. Therefore we need to choose the spectral resolution carefully for optimal results.

EOS: simple polytrope

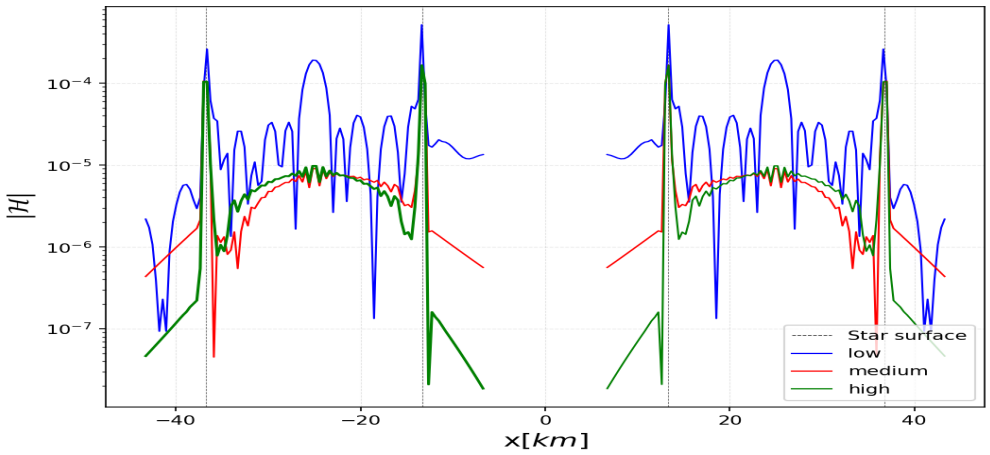

Figure 5.3: Hamiltonian constraint violation of BNS with for simple polytropic EOS having $\Gamma = 2.5$ with gravitational mass = $1.32 M_\odot$ and a separation of 50 kms

EOS: Piecewise polytrope

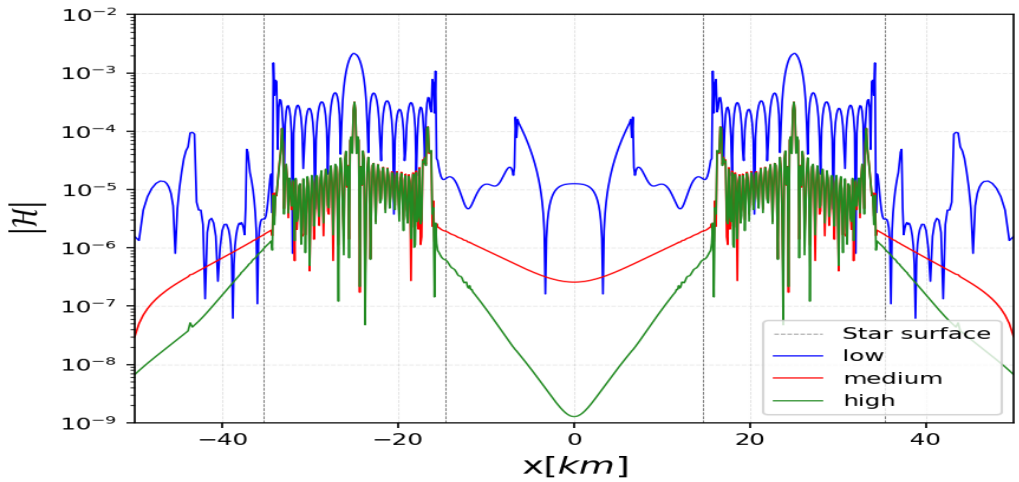

Figure 5.4: Hamiltonian constraint violation of BNS with piecewise polytropic EOS with gravitational mass = 1.32$M_\odot$ and a separation of 50 kms

EOS: Tabulated (older version taken from [6])

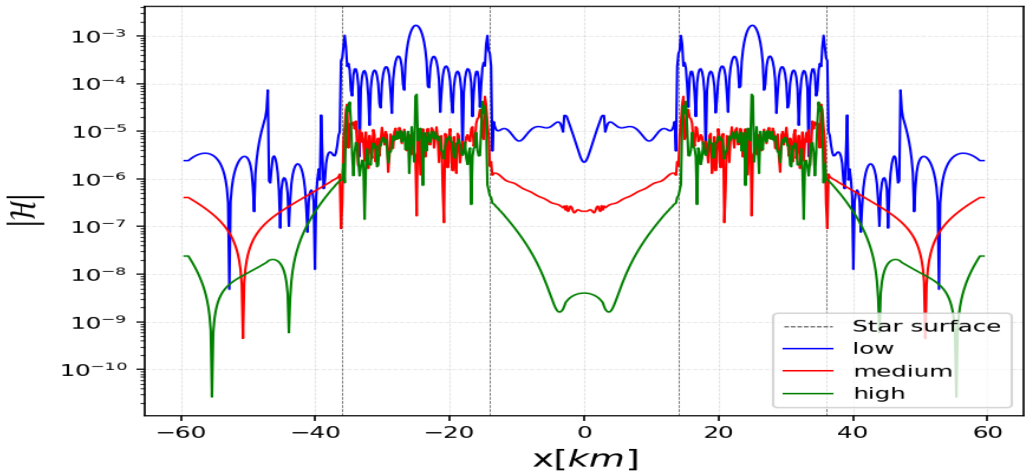

Figure 5.5: Hamiltonian constraint violation of BNS with for tabulated EOS:BHB$\lambda\phi$ [5] with tables developed by [6] with gravitational mass = 1.32$M_\odot$ and a separation of 50 kms

EOS: Tabulated (newer version taken from [8])

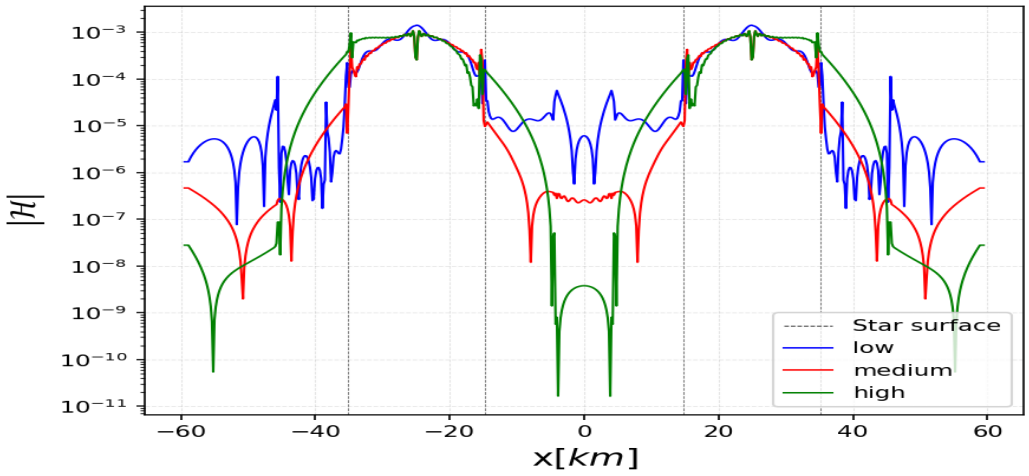

Figure 5.6: Hamiltonian constraint violation of BNS with for tabulated EOS:LS220 [7] with SREOS table developed by [8])

As discussed in section 5.2 we have used the finite temperature tables to convert a function of three variables, the electron fraction Ye, the rest mass energy density (ρ), and temperature (T) into a 1D table, which is read as an input into `LORENE`. The slicing algorithm uses the following steps:

1. Read in the input variables from the tables: Y_e, P, ϵ, T, and ρ and the chemical potentials.
2. Find the temperature index at which the tables needs to be sliced.
3. Set 2d interpolators for P and ϵ as functions of ρ and Y_e.
4. Finally, determine P and ϵ in β equilibrium for the particular densities.

We can see from Fig 5.3, Fig 5.4 and Fig 5.5 that increasing the spectral resolution of the grid in `LORENE` improves conservation of Hamiltonian constraints within the star and in the vacuum region.

We can see from Fig 5.6 that increasing spectral resolution only improved the constraint violations in vacuum region, while there was little to no improvement inside the stars. It also worth noting that convergence issues are largely associated with the fluid itself in virtually all cases, as we see increased convergence down to very small levels in the vacuum regions of the simulation in virtually all cases. Increasing resolution within `LORENE` is unlikely to help once

we start encountering (small) Gibbs phenomenon errors associated with the NS surfaces being "seen" in the other domain set. The remaining non-convergent behavior is likely attributed to discretization effects from within the Einstein Toolkit.

The non-convergent behavior, which appears in the domain containing the NS for every EOS model that `LORENE` can compute, is an inevitable side effect of the dual-coordinate multi-domain spectral method used to describe binary systems. For a single NS, using a single set of nested domains and placing a domain boundary at the stellar surface is sufficient to eliminate numerical errors associated with Gibbs' phenomenon. For a binary system, this can only serve to minimize Gibbs' phenomenon noise to the extent possible. Indeed, the "auto-potentials" that appear as the component of a given metric field whose source is centered on a given star are able to confine all non-smooth behavior to the domain boundary, but when `LORENE` interpolates these values over to the coordinates describing the other domain to form the "comp-potentials", there will inevitably be non-smooth behavior captured by the transition. The resulting Gibbs' phenomenon errors will appear as spurious oscillations in the source potentials, which are then fed through the elliptic equations, in particular as pre-factors multiplying the densities and/or momenta in Eqs. 2.4.56, 2.4.57, and 2.4.60. In vacuum regions, these particular density/momentum source terms are uniformly zero, and we see errors that decay exponentially with distance from the stellar surface whose source is the much smaller-magnitude terms in which auto-potentials are multiplied by comp-potentials, yielding effectively spectral convergence in the vacuum regions between, around, and outside of both NS.

5.3.1.2 Changing number of domains

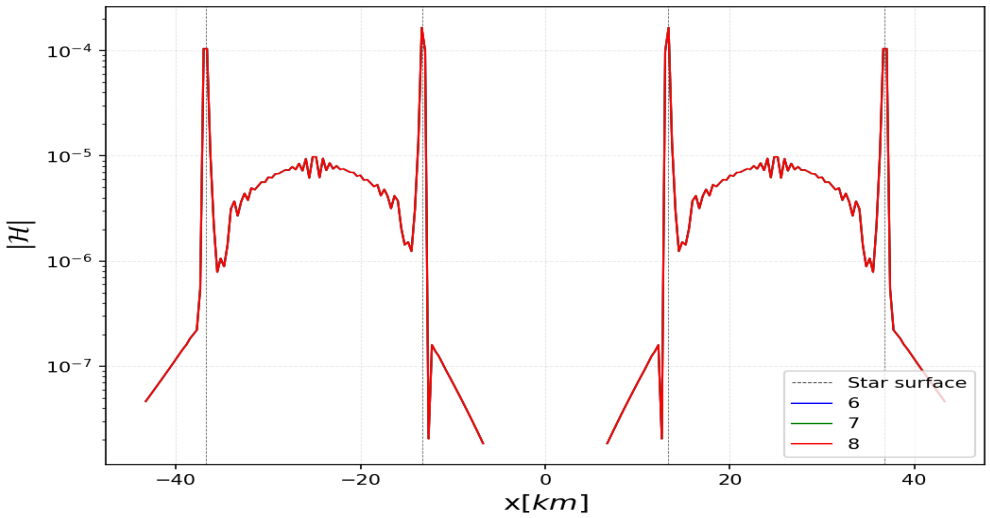

Figure 5.7: Hamiltonian constraint violation of BNS with for tabulated EOS having $\Gamma = 2.5$

5.3.1.3 Changing the convergence factor

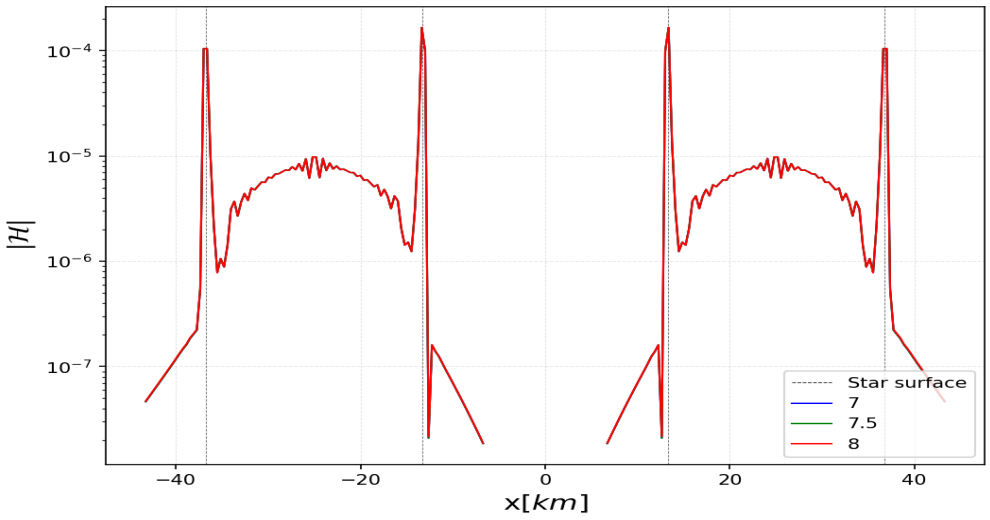

Figure 5.8: Hamiltonian constraint violation of BNS with for tabulated EOS having $\Gamma = 2.5$

We can conclude from Figure 5.7 and 5.8 that increasing the number of domains did not change the Hamiltonian constraint violations, as the curves are completely overlapping. It

is worth noting that we also tried changing the location of domain boundaries, but found that since essentially all of the constraint violation can be attributed to the surface of NS themselves, it doesn't matter how many domains we use to resolve the vacuum regions of the space nor their specific radii.

5.3.2 Summary of analysis performed to study the conservation of Hamiltonian constraints

- We can see from the plots above that increasing the spectral resolution improved the Hamiltonian constraint violation for all three EOSs. If we increase `LORENE` resolution even further, it is unlikely to help as the remaining non-convergent behavior is likely attributable to Gibbs phenomenon effects in the elliptic equation source terms used by the multidomain spectral method.
- There is no improvement in the quality of initial data when we change the number of domains or the convergence factor of `LORENE` used as a stopping condition for a given run.
- The Hamiltonian constraint violations do reduce down to very small values at the grid points associated with vacuum regions in virtually all cases.
- As shown in Fig. 4.4, minor details in the stellar configuration owing to the exact iteration at which a run is declared to have converged do not seem to be the key factor determining Hamiltonian constraint violation. It is a global property of having a NS with a surface producing Gibbs phenomenon errors in the potentials seen by its companion.

5.4 Dynamical Simulations

5.4.1 Mass Ejecta

In order to study the relationship between the initial binary NS parameters, including the choice of the NS EOS, and the amount of unbound mass left on the grid during and immediately after the merger, we have conducted high-resolution dynamical simulations of BNS mergers for different mass ratios and EOSs. The fluid material is considered ejected from the system when it is unbound by the gravitational potential of the BNSs and the merger remnant formed after the merger.

There are two criteria that can be used to define whether or not a fluid element is "unbound". For particles in Newtonian physics, one would typically only need to check whether the potential energy or kinetic energy is of larger magnitude. For fluid configurations, hydrodynamic simulations typically require one to modify the kinetic energy description to include the internal energy of the gas as well: even if a small region of the fluid has not achieved escape velocity collectively, the fluid will be expected to expand if placed in a low-pressure environment with the vast majority of the mass eventually becoming unbound as a result should the temperature/internal energy be sufficiently large. For our calculations, we use the relativistic analogue of this latter approach. The fluid material is considered unbound when it satisfies the following condition

$$hu_t < -1, \tag{5.4.4}$$

where u_t is the first component of the fluid velocity at each grid point given as

$$u_t = u_\nu t^\nu, \tag{5.4.5}$$

where t^ν is a timelike vector [60]. The mass of the ejecta can then be calculated by integrating the total fraction of rest mass that is unbound over some volume using the above condition:

$$M_{unbound} = \int_{hu_t<-1} \rho \; d^3x \tag{5.4.6}$$

In order to study the dynamical properties of the mergers that would result from the time evolution of our initial data, and to further validate the ID produced by our modified version of `LORENE`, we used the `EinsteinToolkit` (ETK) with the IllinoisGRMHD evolution system [61] & [62] to dynamically simulate BNS configurations. ETK has modules that are built to read `LORENE`'s ID. To see the evolution of the merger, we have plotted the distribution of different quantities: the fluid density, enthalpy, and the metric terms needed to classify whether matter remains bound or has become unbound from the binary. We have used three different EOSs: simple polytropes with $\gamma = 2$ and piecewise polytropes representing the APR4[55] and SLy[56] EOSs. The initial distance between the NSs was chosen to be 40km for all the simulations. Distance is in km and units of time and density in geometric units. For $G = c = \mathrm{M}_\odot = 1$, t=1 in geometric units is 4.93×10^{-6}s and ρ =1 is 6.194×10^{17} g/cm^3. We have implemented the following grid structure for the dynamical simulation runs

- The grid extends to +/- 3729.04 km in the x-, y- and z-directions.
- There are 7 refinement boundaries, each with a factor of two improvement in resolution.
- The finest-level resolution is $\sim$120 m.
- After the black hole is formed, two additional refinement levels are added, centered at the remnant, yielding a finest resolution after merger of $\sim$30 m.

Run 1: PPEOS- APR4, $M_1 = 1.4$ and $M_2 = 1.4$

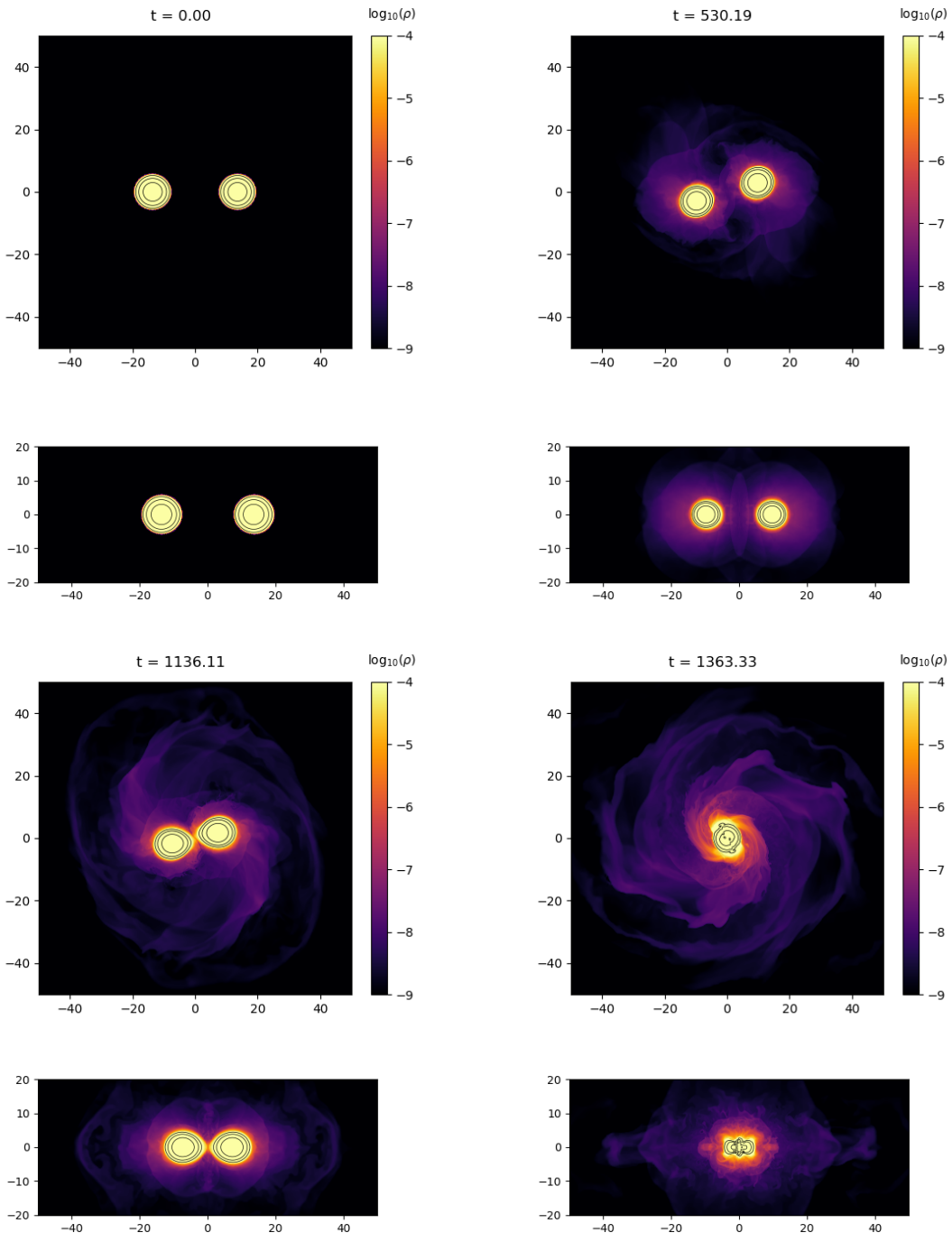

Run 1: PPEOS- APR4, $M_1 = 1.4$ and $M_2 = 1.4$

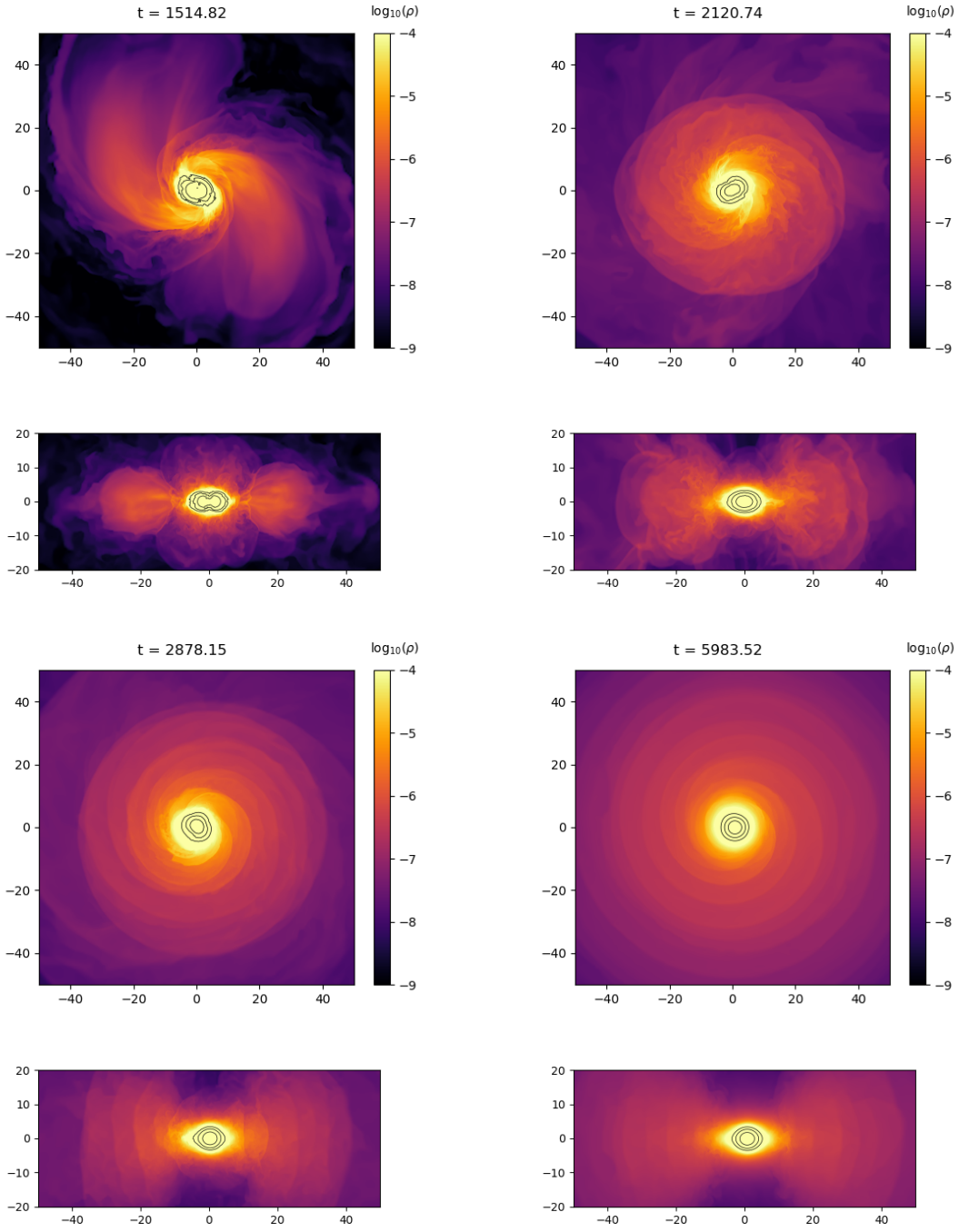

Figure 5.9: Evolution of the density for a BNS system with masses of $1.4M_\odot$ each and piecewise polytropic APR4 EOS, shown at equivalent times for the $x-y$ and $x-z$ planes, respectively (top and bottom of each subfigure). The run was stopped at 29.8ms. The merger remnant at the end of 29.8ms is a hypermassive neutron star.

Run 1: PPEOS- APR4, $M_1 = 1.4$ and $M_2 = 1.4$

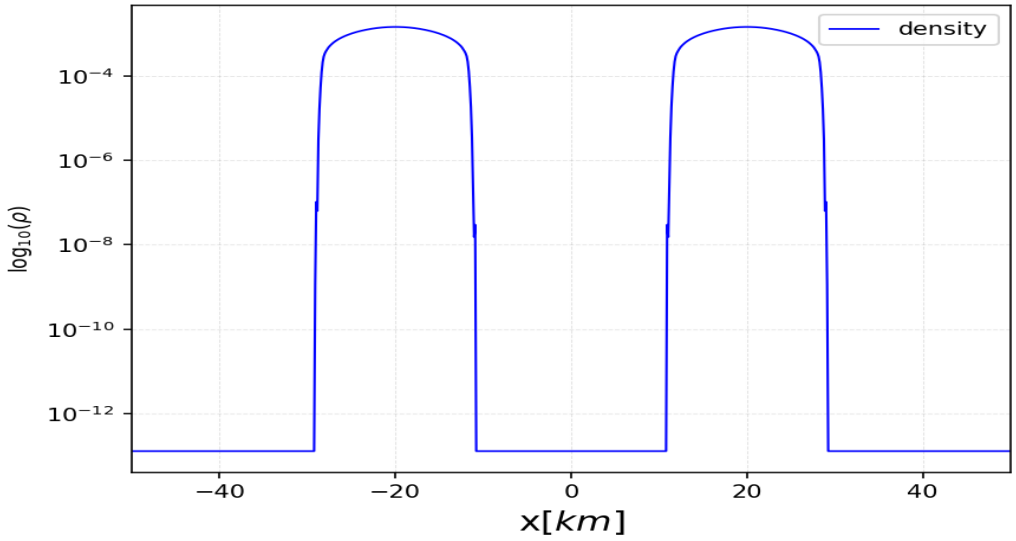

Figure 5.10: Density profile at $t = 0$

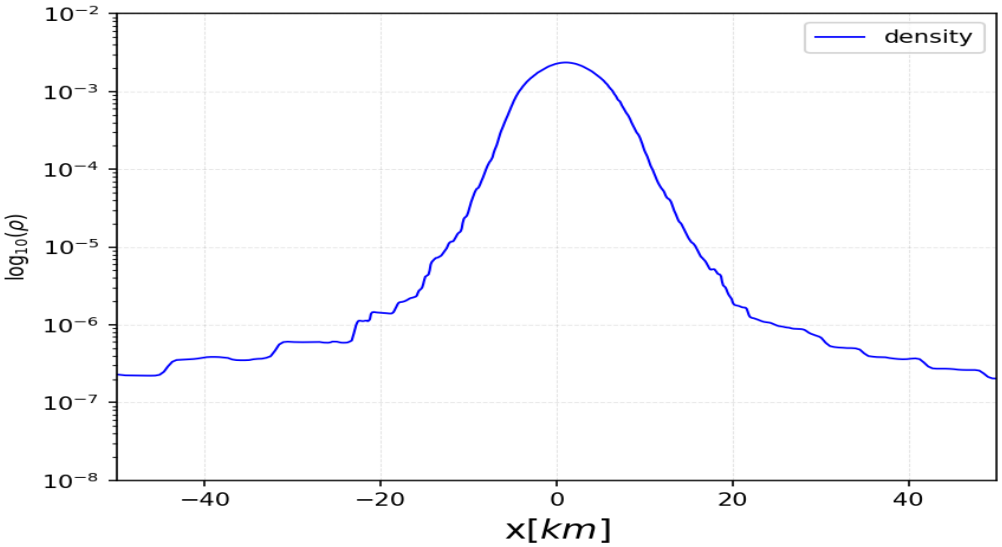

Figure 5.11: Density profile at $t = 6059.26$ CU

Analysis of Run 1: PPEOS- APR4, $M_1 = 1.4$ and $M_2 = 1.4$

The simulation begins from an initial separation of 40 km with a total mass of $2.8M_\odot$ and a mass ratio of 1. As the initial orbital separation is only a few times of the radii of NSs, such binaries rapidly become unstable and we need to use numerical relativity to dynamically simulate the system. The BNS configuration is evolved relativistically using the `EinsteinToolkit` (ETK) with IllinoisGRMHD [61] & [62]. Since the two NS masses are equal, the merger resembles a slow collision. First, the stars inspiral together and their orbital separation decreases. As their separation further decreases, the NS surfaces come in contact with each other and the two NS form a dumbbell shaped massive NS remnant comprised of two cores. Eventually the dumbbell shape transforms into an ellipsoid due to loss of angular momentum and gravitational wave emission, as the ellipticity of the remnant decreases with time. The angular momentum loss rate depends on the type of EOS. As seen from Figs. 5.9 and 5.11 the remnant stabilizes into a long-lived, oblate-spheroid shaped HMNS as predicted by earlier studies [22]. For this particular run, we stopped the simulation at 29.8 ms, at which time it remained a HMNS. If we continued the simulation, it could have eventually collapsed into a BH as the total mass of the NSs at the beginning of the simulations is equal to $2.8M_\odot$, but the timescale on which this is expected to occur is much larger than we can simulate using these techniques. Very little mass ejecta left on the grid during the merger process, due to the symmetrical nature of the NS masses and their resulting evolution process – neither star can be said to be tidally disrupted during the merger process, and only weak mass loss in a spiral pattern from the outer edges is seen, very little of which is outflowing with significant enough velocity to unbind the material.

5.4.2 Formation of hyper massive neutron star

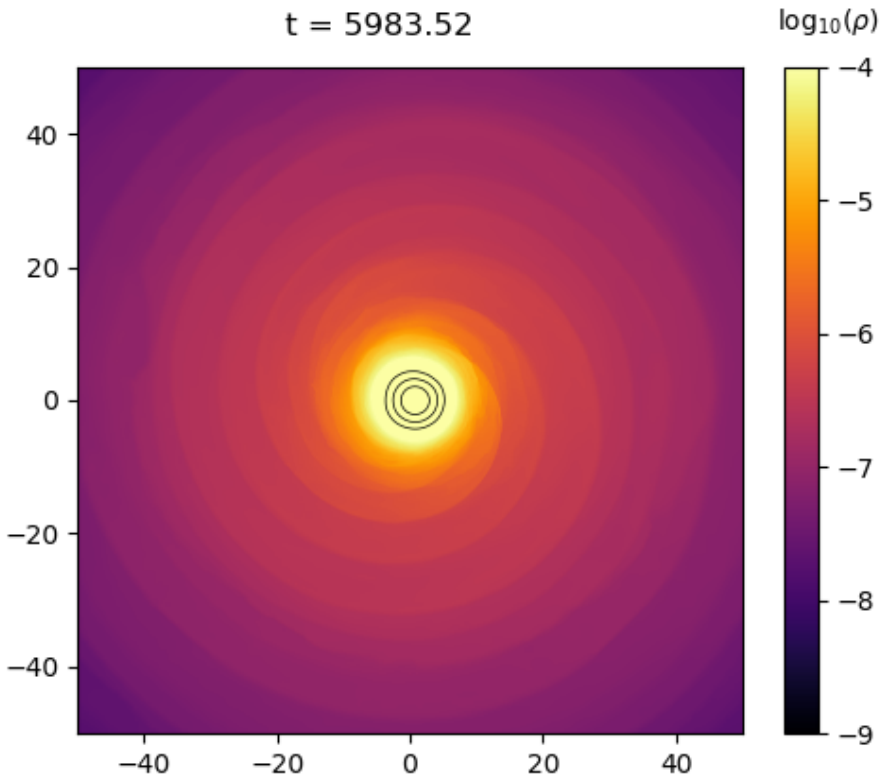

Figure 5.12: Density profile at late times for AP4 EOS run with $M_1 = M_2 = 1.4$, where a HMNS is formed

Run 2: PPEOS- APR4, $M_1 = 1.6$ and $M_2 = 1.4$

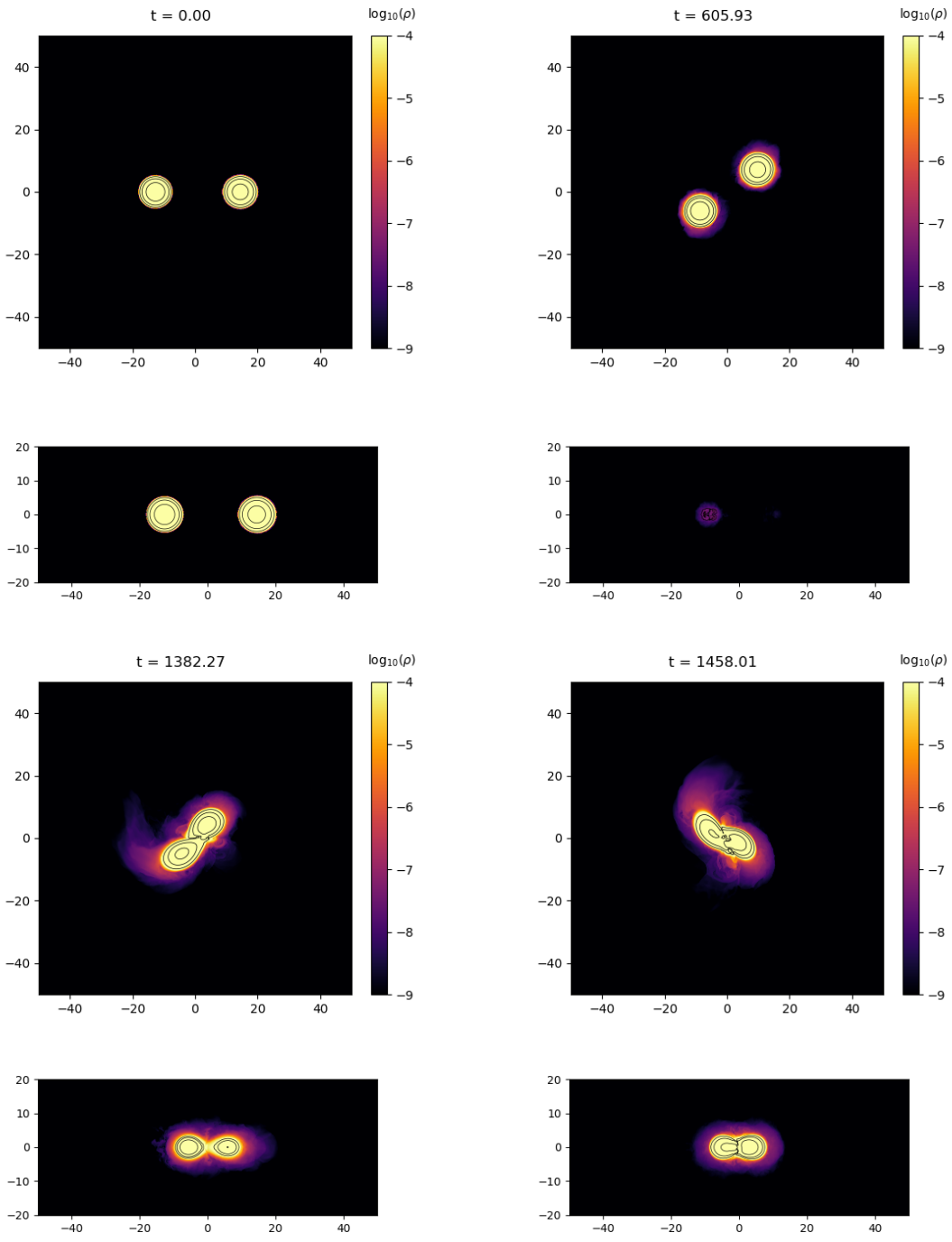

Run 2: PPEOS- APR4, $M_1 = 1.6$ and $M_2 = 1.4$

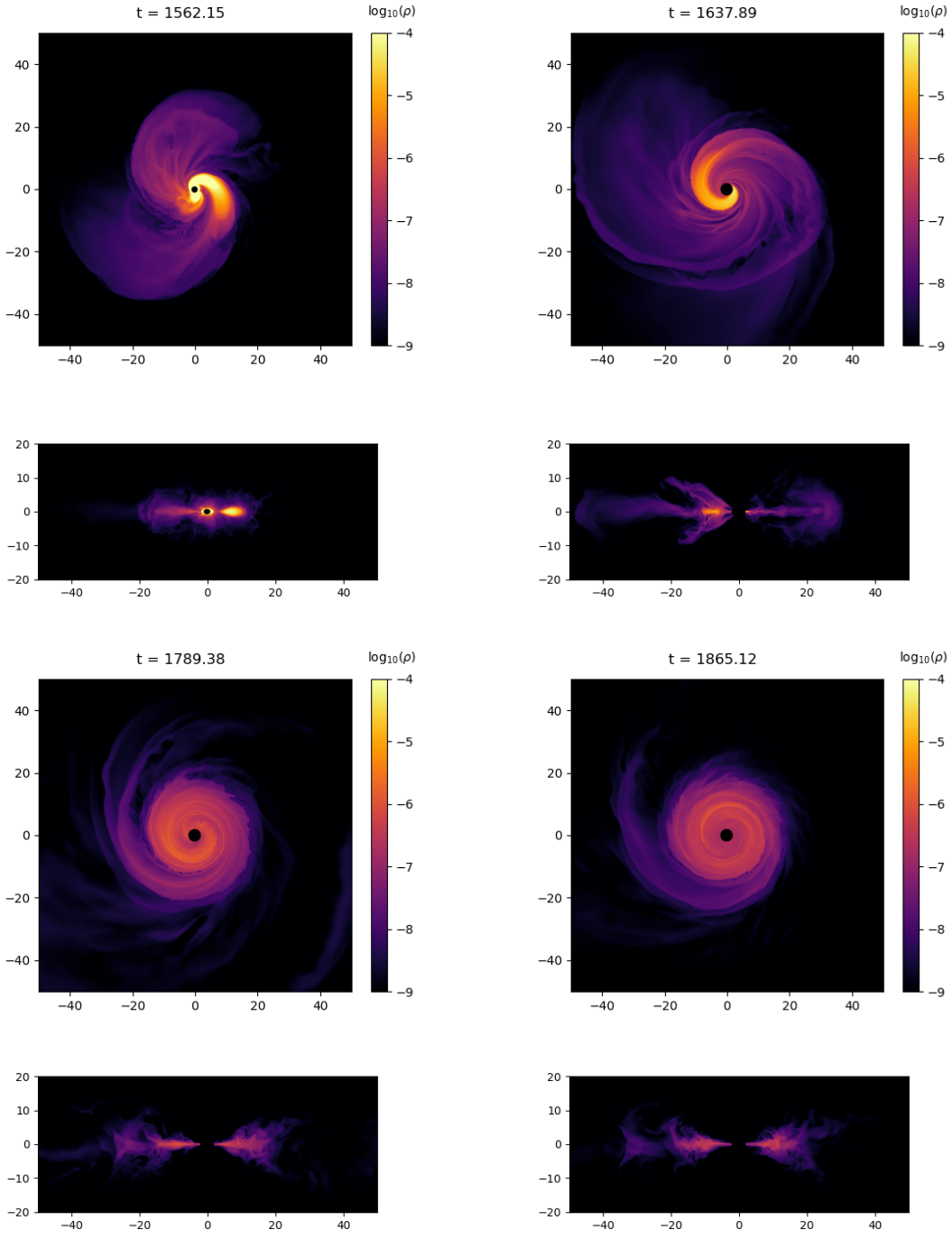

Figure 5.13: Evolution of density of BNS system with masses $1.6M_\odot$ and $1.4M_\odot$ and EOS APR4 in $x-y$ and $x-z$ direction. The merger remnant is a black hole formed at $t = 7.69$ms star.

Run 2: PPEOS- APR4, $M_1 = 1.6$ and $M_2 = 1.4$

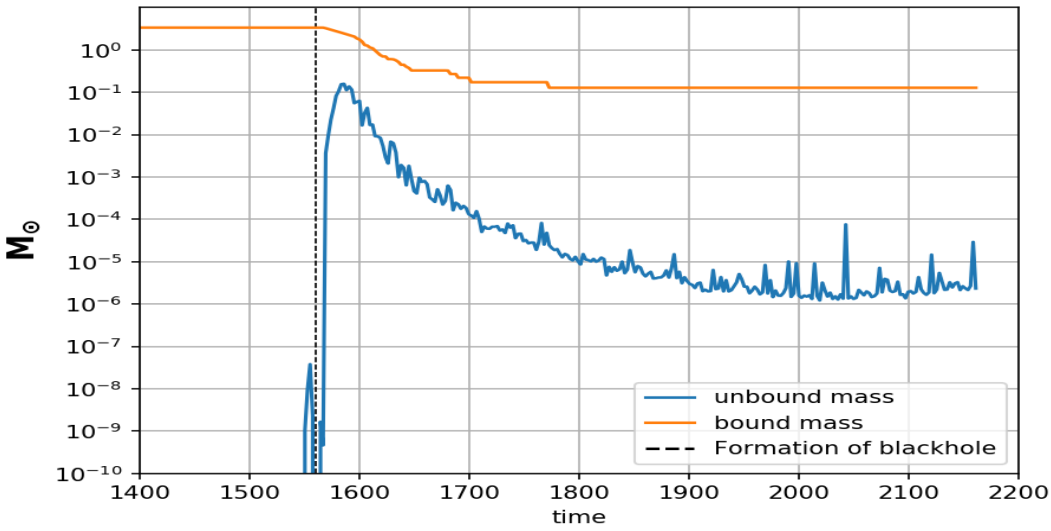

Figure 5.14: Evolution of bound and unbound mass for EOS APR4 having masses 1.6 $M_\odot$ and 1.4 $M_\odot$.

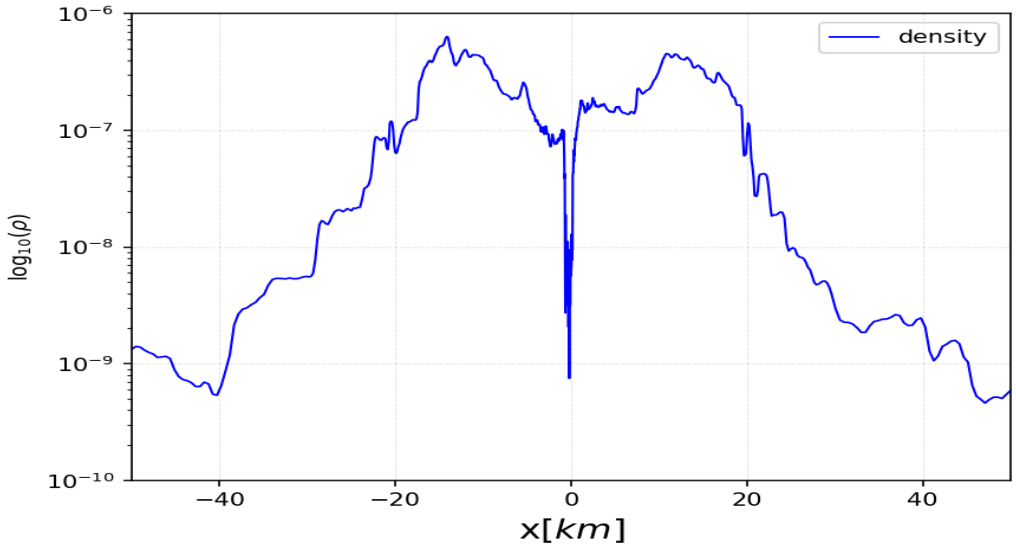

Figure 5.15: Density profile in x direction at $t = 2158.6128$ CU

Analysis of Run 2: PPEOS- APR4, $M_1 = 1.6$ and $M_2 = 1.4$ The simulation begins from an initial separation of 40 km with a total mass of 3.0 $M_\odot$ and a mass ratio of 0.875 ($M_1 = 1.6,\ M_2 = 1.4$). We see that as the stars approach merger, the evolution process for an unequal mass BNS configuration is different from an equal mass configuration. The less massive star gets tidally deformed and its outer layers get stripped during the merger. The stripped material forms an envelope around the remnant while the core of the lower mass NS interacts with the core of the high mass NS, forming a remnant composed of two asymmetric cores. The massive NS remnant eventually relaxes into a quasi stationary state due to release of angular momentum by interacting with the envelope, thus decreasing the degree of asymmetry. The merger occurs more rapidly from a given initial orbital separation than an equal mass ratio BNS systems and has a larger amount of mass ejecta. As can be seen from the density profile plotted in Figure 5.14, an accretion disk is formed at around 10km away from center, and the remnant promptly collapses into BH at 7.69 ms after the start of simulation.

Run 3: PPEOS- APR4, $M_1 = 1.8$ and $M_2 = 1.4$

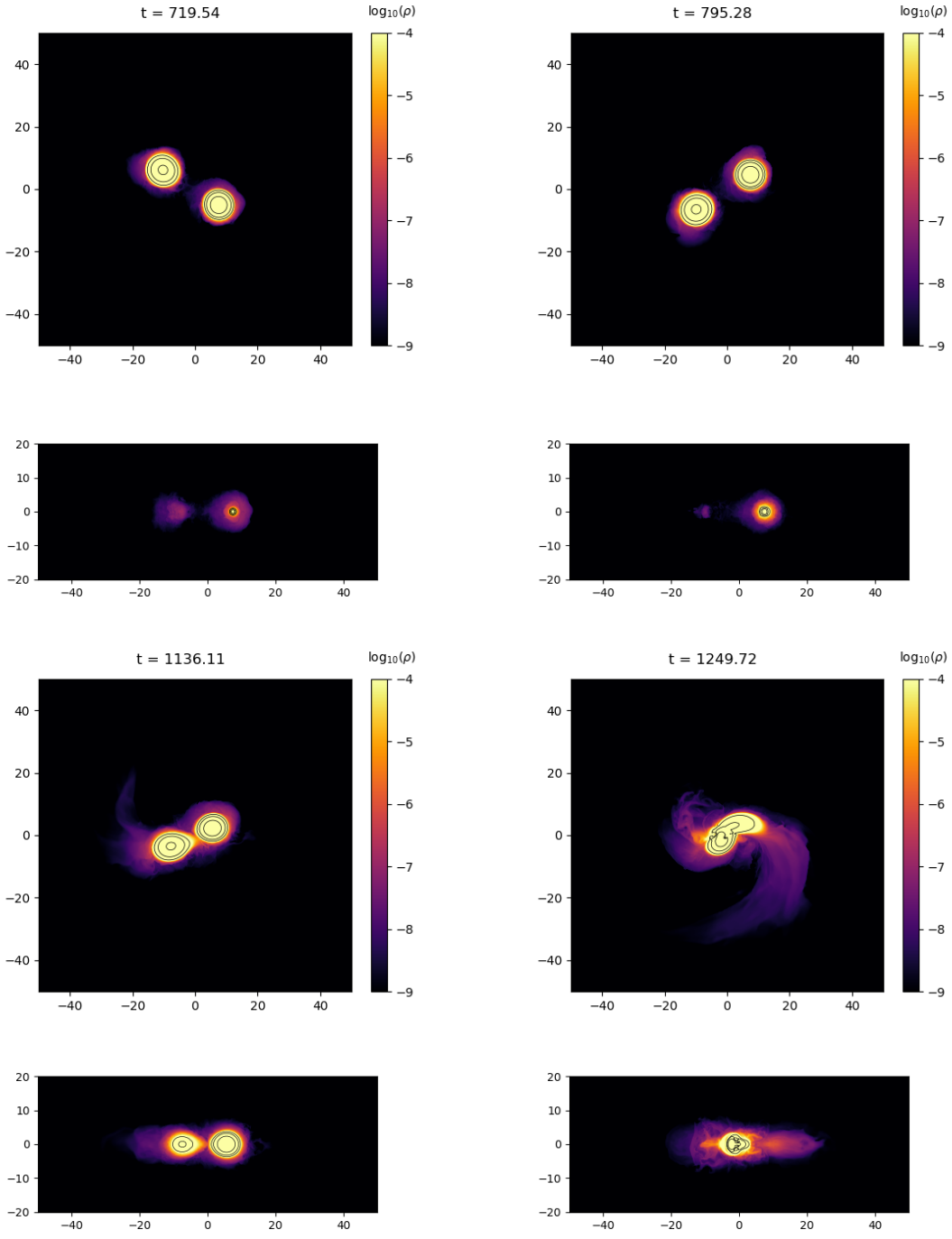

Run 3: PPEOS- APR4, $M_1 = 1.8$ and $M_2 = 1.4$

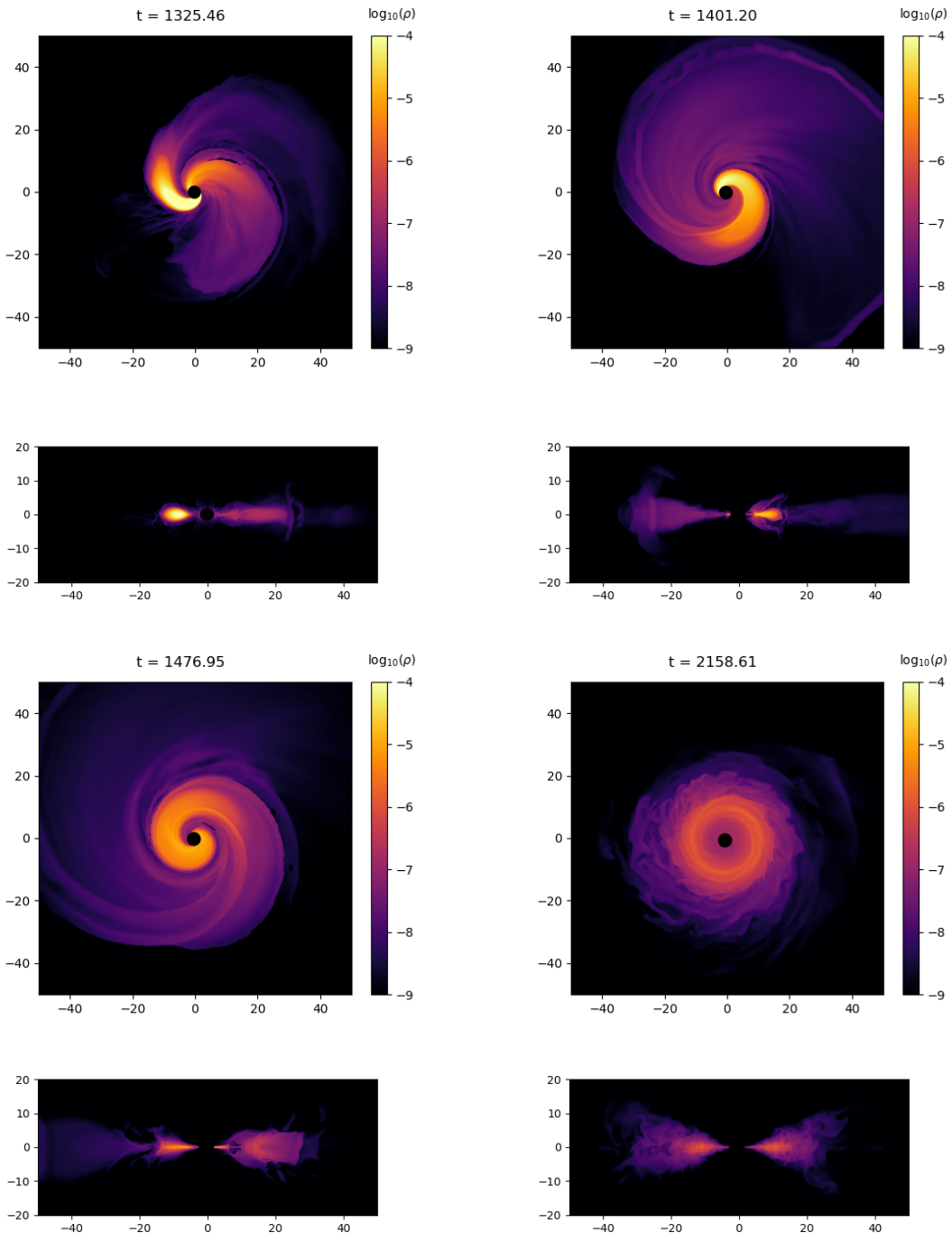

Figure 5.16: Evolution of the density of a BNS system with masses $1.8M_\odot$ and $1.4M_\odot$ and AP4 EOS in the $x-y$ and $x-z$ directions. The merger remnant is a black hole formed at t = 7.69ms.

Run 3: PPEOS- APR4, $M_1 = 1.8$ and $M_2 = 1.4$

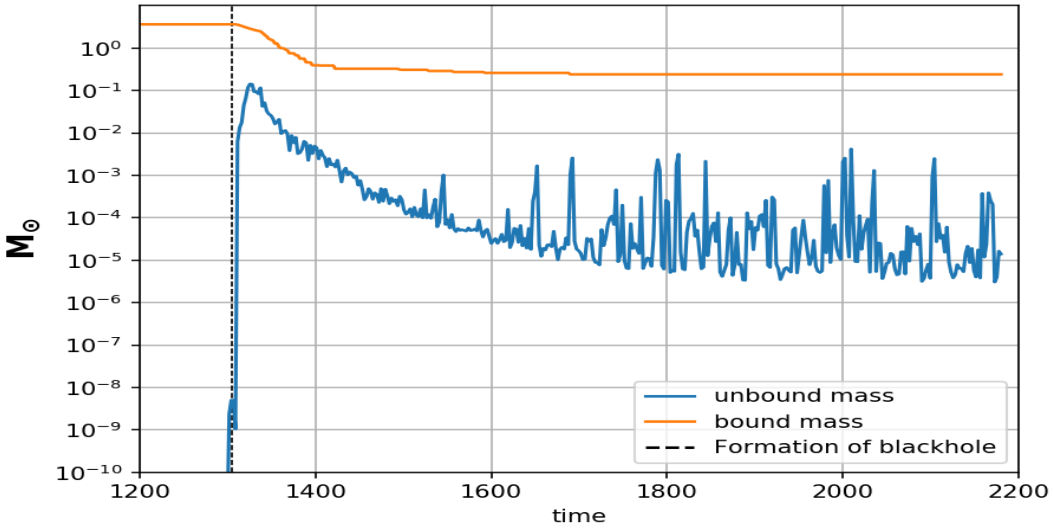

Figure 5.17: Evolution of bound and unbound mass for EOS APR4 having masses 1.6 $M_\odot$ and 1.4 $M_\odot$.

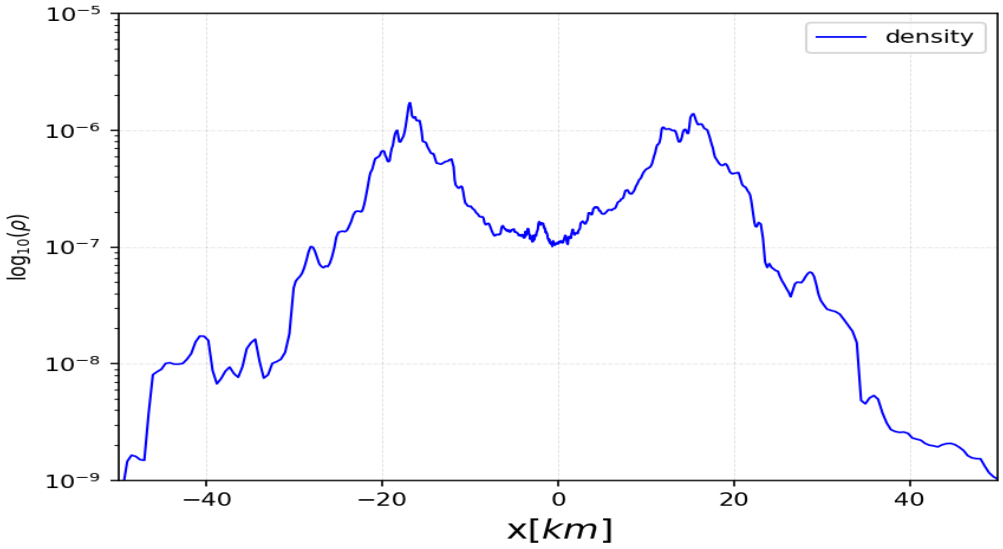

Figure 5.18: Density profile in the $x-$direction at t = 2158.6128 CU

Analysis of Run 3: PPEOS- APR4, $M_1 = 1.8$ and $M_2 = 1.4$ The simulation begins from an initial separation of 40 km and the total mass of the system is 3.2 $M_\odot$ with a mass ratio of 0.78 ($M_1 = 1.8,\ M_2 = 1.6$). Here, the evolution process is similar to the process of Run 2 due to the unequal mass ratio. Compared to Run 2, the merger occurs at an even larger orbital separation and at a faster rate due to the more extreme mass ratio, resulting in a more violent tidal disruption of the secondary. As can be seen from Fig 5.18, the accretion disk is denser at $t = 2158$CU than the disk formed during Run 2 and the remnant collapses to a BH sooner, at 6.31ms.

Run 4: PPEOS- SLY, $M_1 = 1.4$ and $M_2 = 1.4$

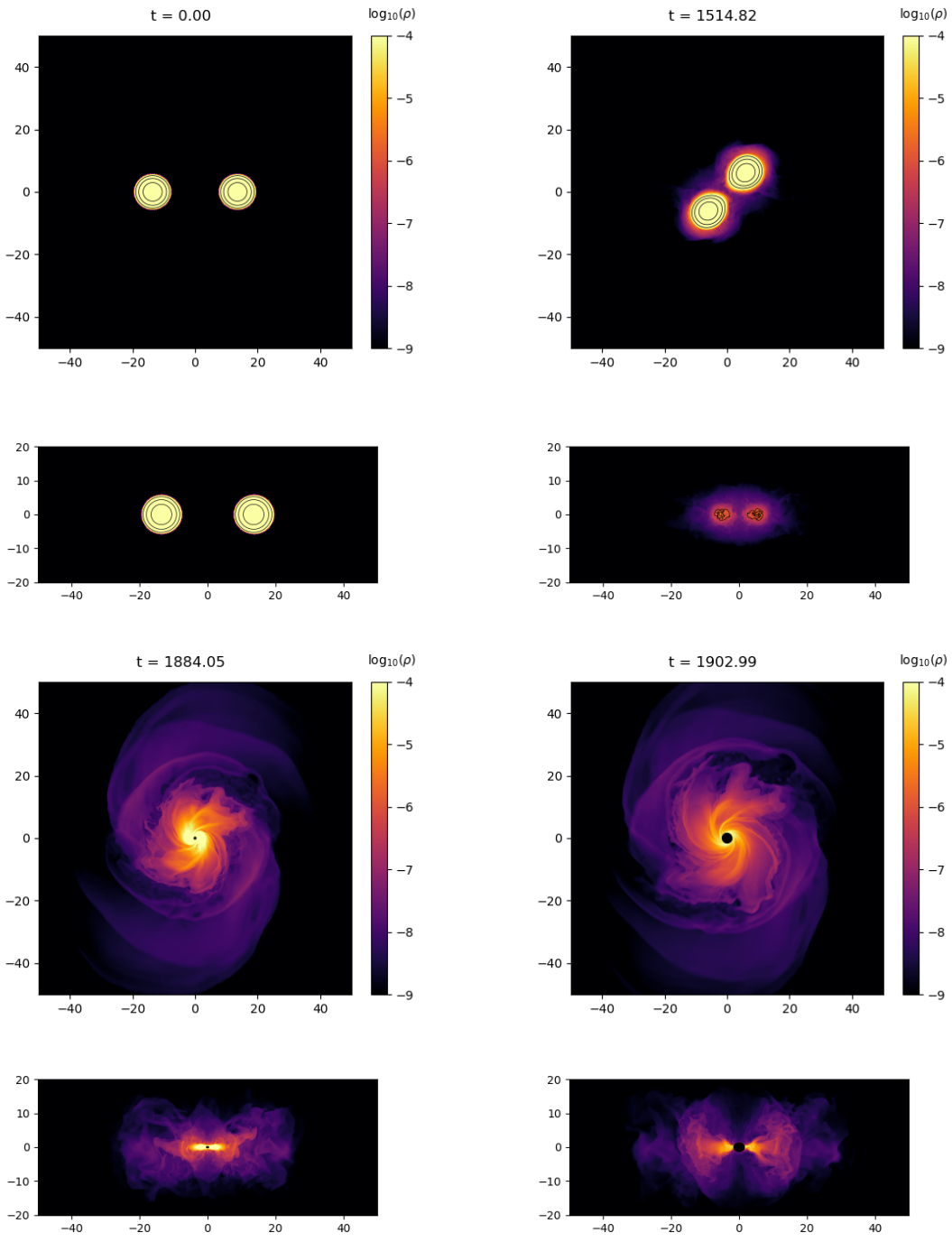

Run 4: PPEOS- SLY, $M_1 = 1.4$ and $M_2 = 1.4$

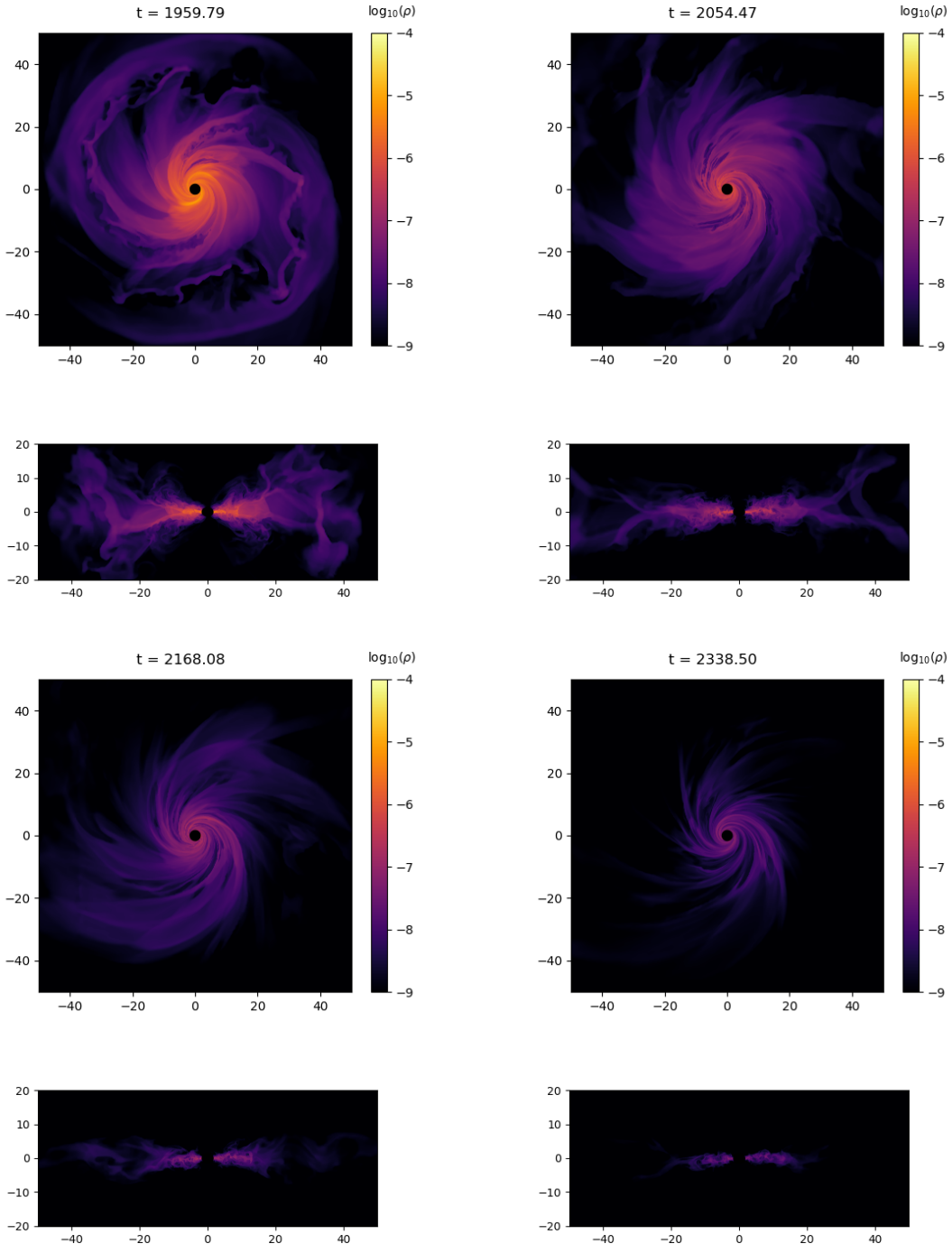

Figure 5.19: Evolution of the density of a BNS system with masses $1.4M_\odot$ and $1.4M_\odot$ and Sly EOS, shown in the $x-y$ and $x-z$ directions. The merger remnant is a black hole formed at $t = 9.25$ms.

Run 4: PPEOS- SLY, $M_1 = 1.4$ and $M_2 = 1.4$

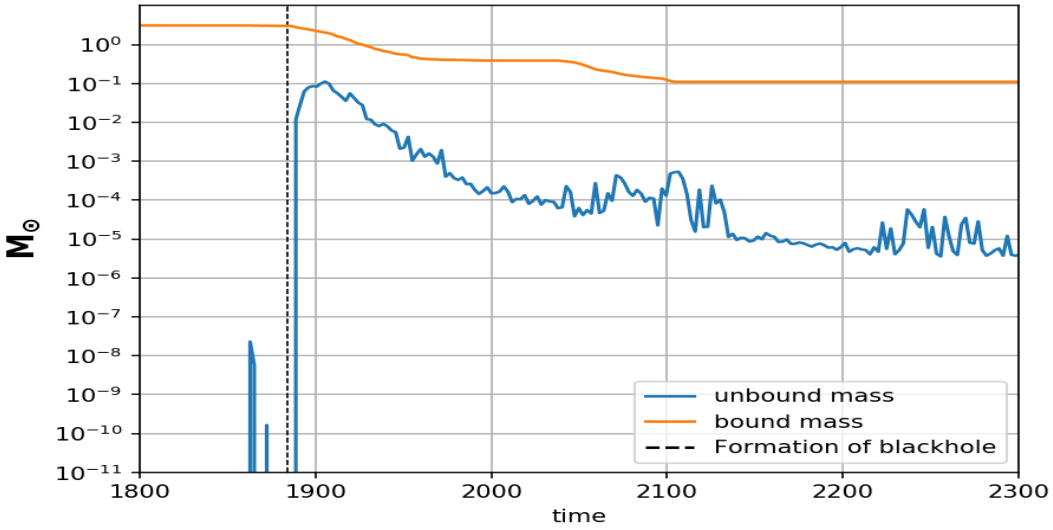

Figure 5.20: Evolution of bound and unbound mass for Sly EOS with NS masses 1.4 $M_\odot$ and 1.4 $M_\odot$.

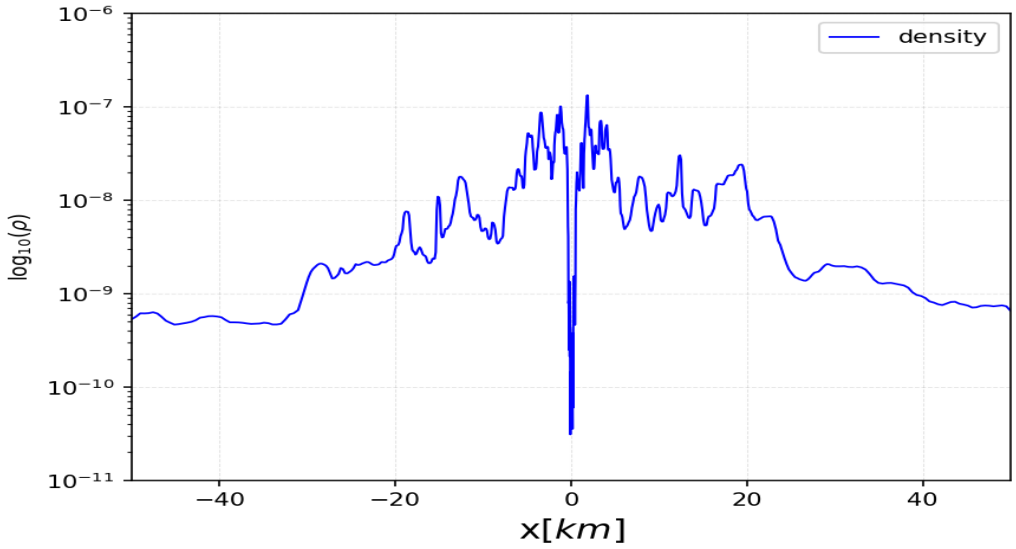

Figure 5.21: Density profile in the $x-$direction at $t = 2338.4972$ CU

Analysis of Run 4: PPEOS- SLY, $M_1 = 1.4$ and $M_2 = 1.4$

1. The simulation begins from an initial separation of 40 km and the total system mass is $2.8M_\odot$ with a mass ratio of unity. The evolution process is similar to the process of Run 1, as it is an equal mass BNS system the merger resembles a slow collision. The stars plunge together as their orbital separation decreases. Unlike the case of the AP4 EOS shown previously, the remnant of this run promptly collapses into a BH, as opposed to Run 1, where for a similar mass configuration the remnant was a long-lived HMNS. This is due to the difference in stiffness of the EOSs for both of the runs – AP4 can support a larger stable mass configuration than Sly. The BH forms at 9.25 ms after the start of simulation run.

Run 5: PPEOS- SLY, $M_1 = 1.6$ and $M_2 = 1.4$

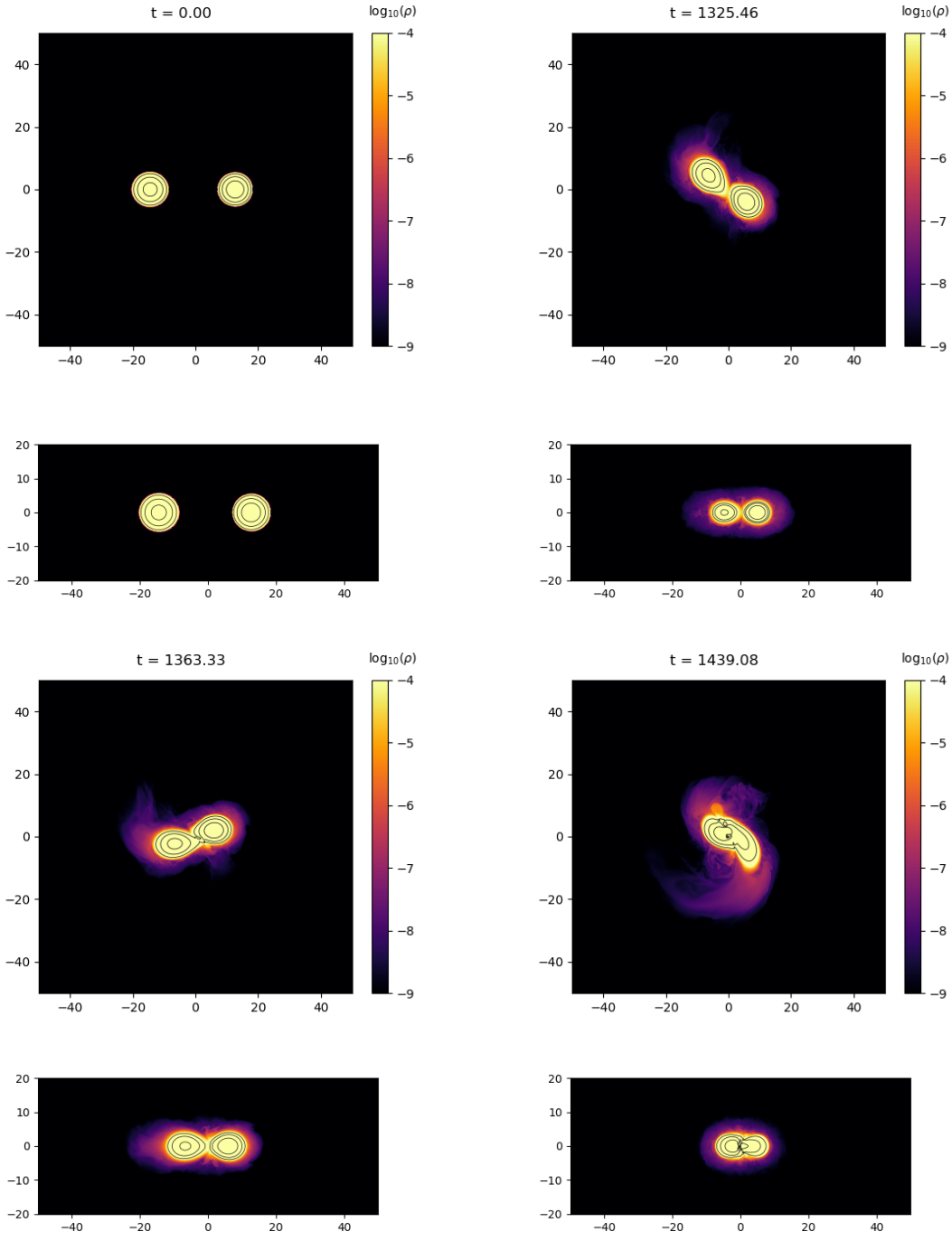

Run 5: PPEOS- SLY, $M_1 = 1.6$ and $M_2 = 1.4$

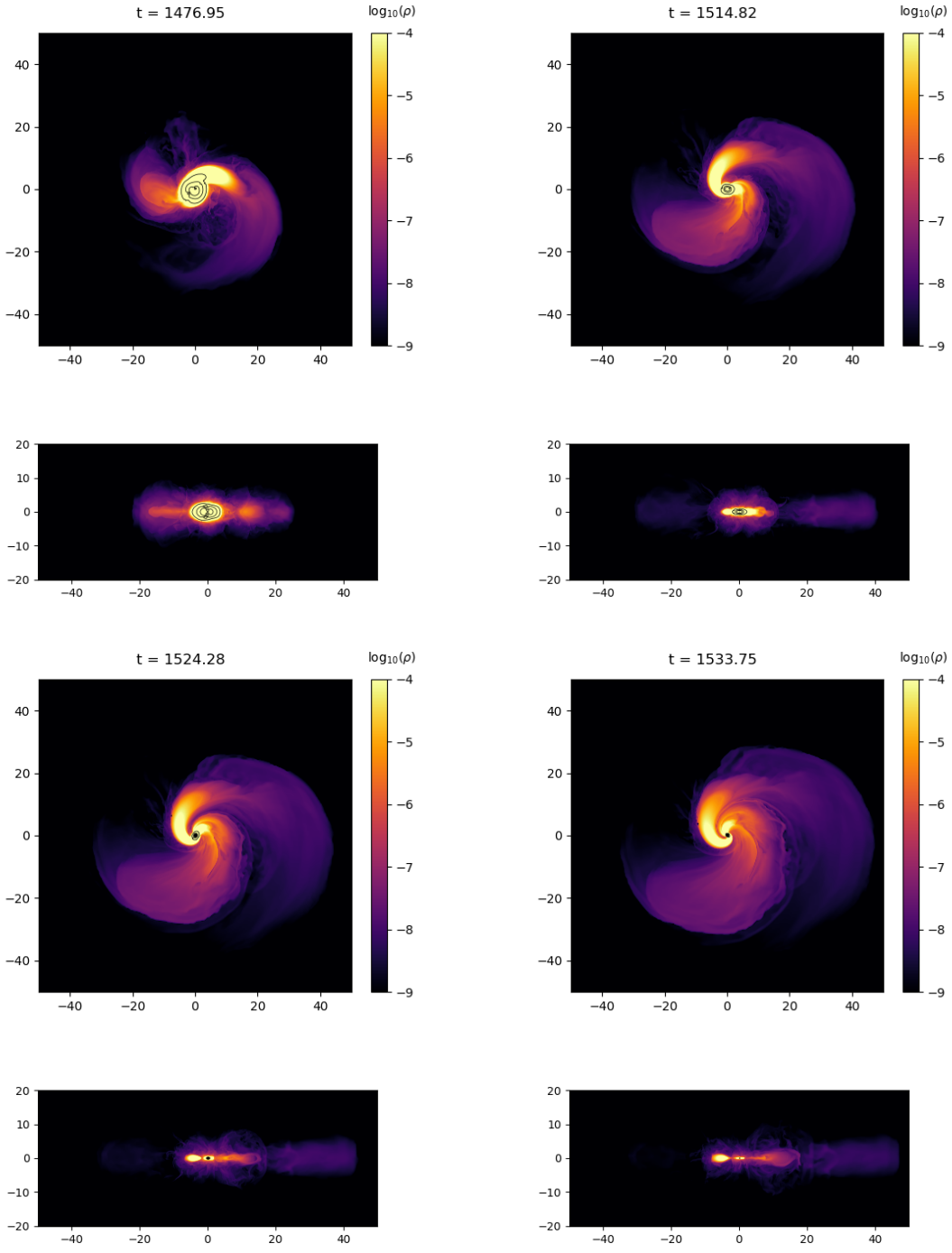

Figure 5.22: Evolution of density of BNS system with masses $1.6M_\odot$ and $1.4M_\odot$ and EOS SLY in $x-y$ and $x-z$ direction. The merger remnant is a black hole formed at $t = 7.86$ms.

Run 5: PPEOS- SLY, $M_1 = 1.6$ and $M_2 = 1.4$

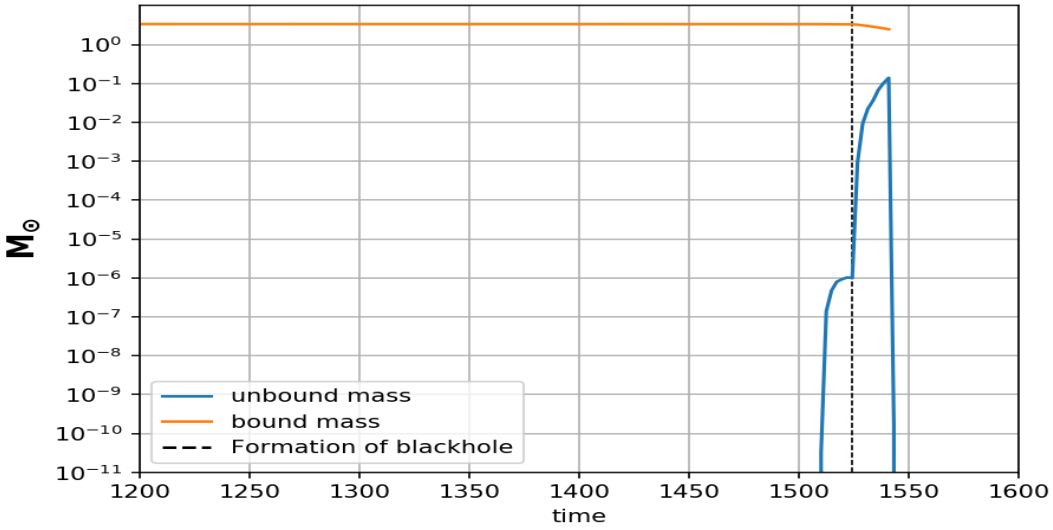

Figure 5.23: Evolution of bound and unbound mass for EOS SLY having masses 1.6 $M_\odot$ and 1.4 $M_\odot$.

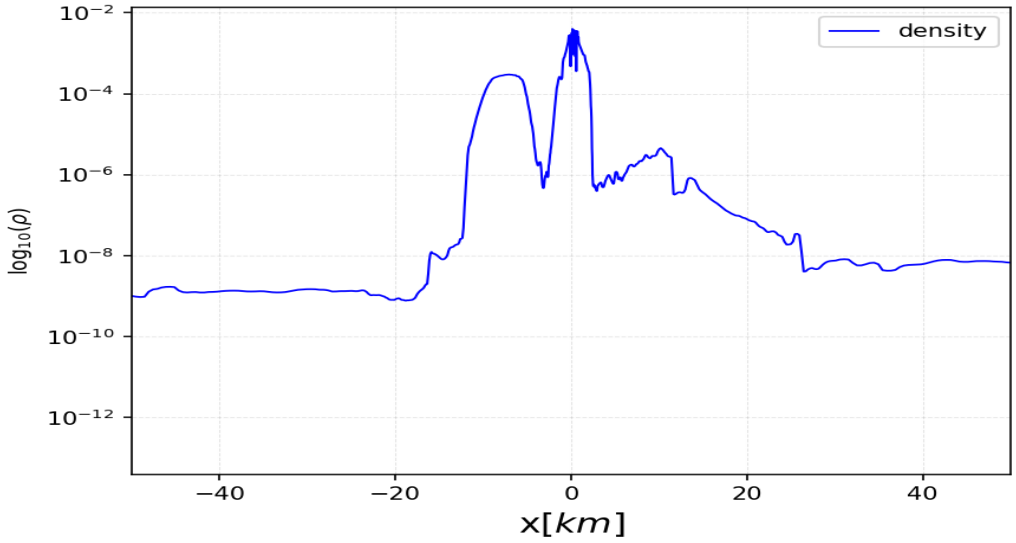

Figure 5.24: Density profile in x direction at $t = 1533.7512$ CU

Analysis of Run 5: PPEOS- SLY, $M_1 = 1.6$ and $M_2 = 1.4$

1. The simulation begins from an initial separation of 40 km with a total system mass of $3.0\mathrm{M}_\odot$ and a mass ratio of 0.875 ($M_1 = 1.6,\ M_2 = 1.4$). The evolution process is similar to the process of Run 2 as it is an unequal mass BNS system, but with a different EOS. The remnant promptly collapses into a BH at 7.86 ms after the start of simulation, very similar to Run 2 which collapses into a BH at 7.69 ms. This run stopped soon after the formation of black hole, due to numerical errors encountered by `IllinoisGRMHD` soon after the BH formed, a challenge for numerical codes that is only exacerbated by the formation of an off-center horizon with a non-trivial kick velocity, owing to asymmetric gravitational wave emission and mass ejecta patterns.

Run 6: PPEOS- SLY, $M_1 = 1.8$ and $M_2 = 1.4$

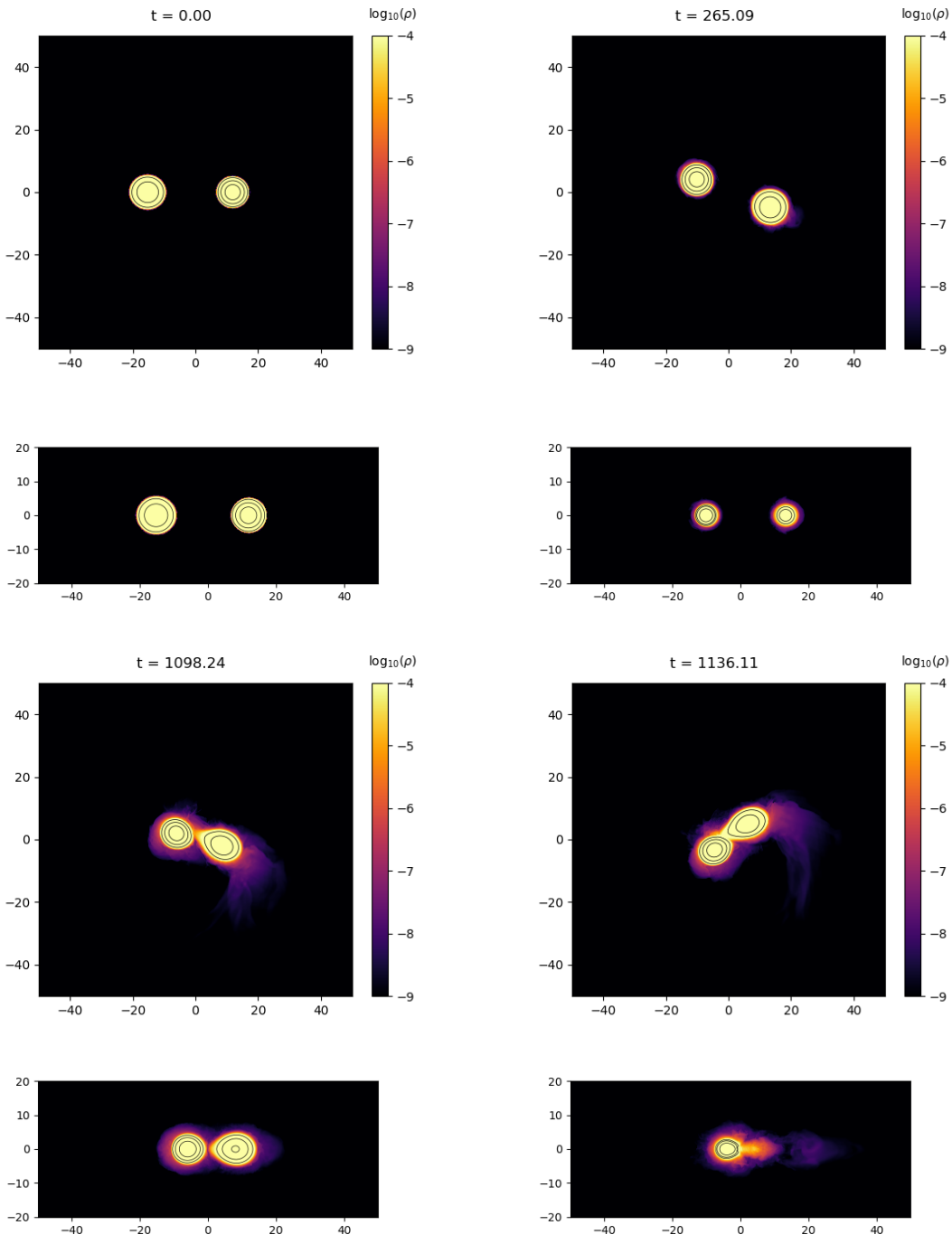

Run 6: PPEOS- SLY, $M_1 = 1.8$ and $M_2 = 1.4$

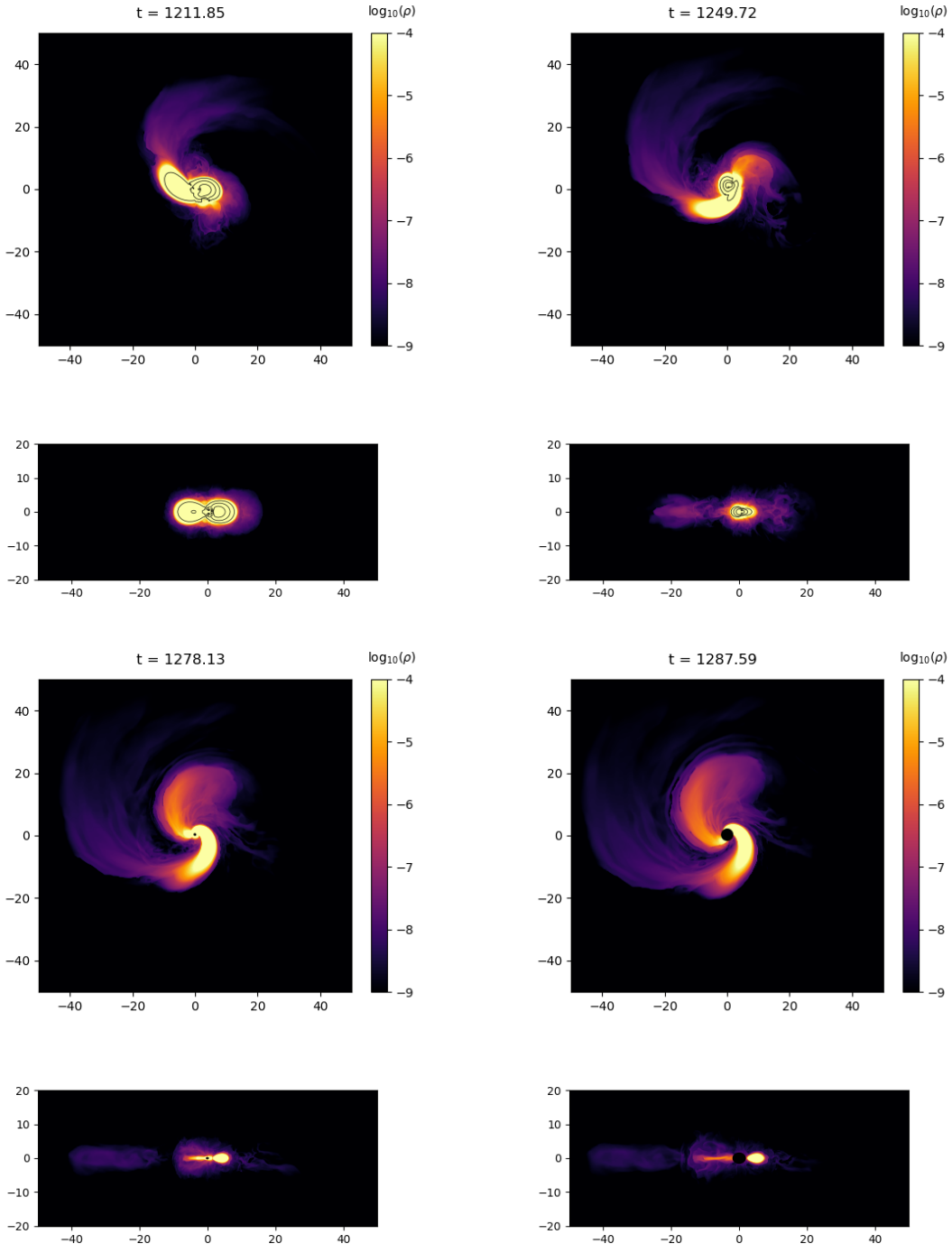

Figure 5.25: Evolution of density of BNS system with masses $1.8M_\odot$ and $1.4M_\odot$ and EOS SLY in $x-y$ and $x-z$ direction. The merger remnant is a black hole formed at $t = 6.26$ms.

Run 6: PPEOS- SLY, $M_1 = 1.8$ and $M_2 = 1.4$

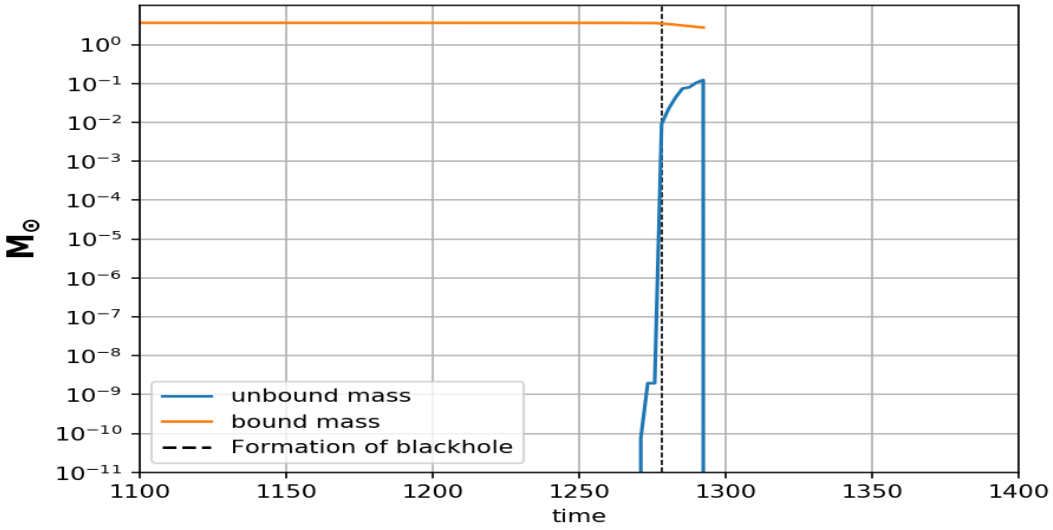

Figure 5.26: Evolution of bound and unbound mass for Sly EOS for NS having masses 1.8 $M_\odot$ and 1.4 $M_\odot$.

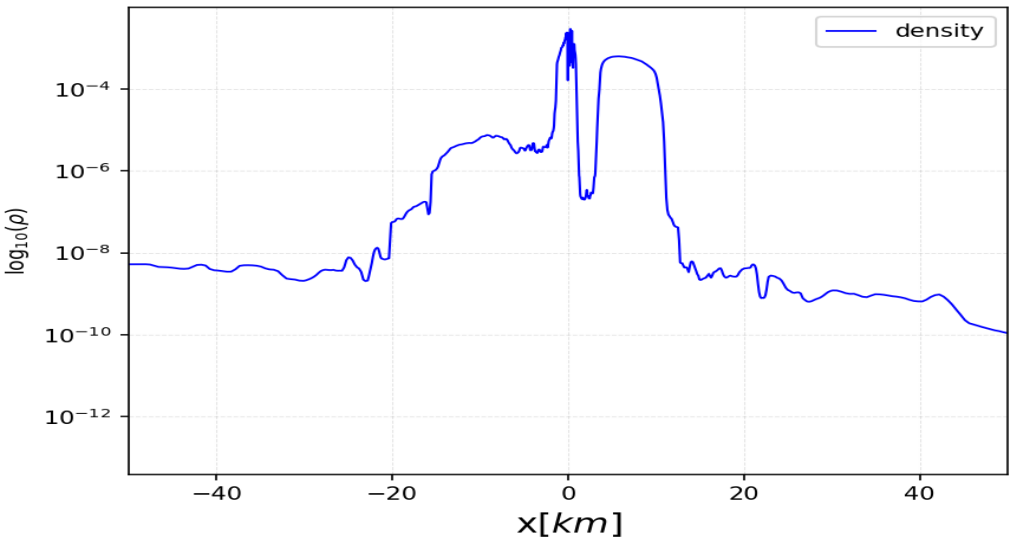

Figure 5.27: Density profile in the $x-$direction at $t = 1287.5936$ CU

Analysis of Run 6: PPEOS- SLY, $M_1 = 1.8$ and $M_2 = 1.4$

1. The simulation begins from an initial separation of 40 kms with a total system mass $3.2M_\odot$ and a mass ratio of 0.78 ($M_1 = 1.8,\ M_2 = 1.4$). The evolution process is similar to the process of Run 3 as it is an unequal mass BNS, system but with a different EOS. Compared to Run 5, the merger occurs at an even larger orbital separation and faster due to the mass ratio. The remnant promptly collapses into a BH at 6.26 ms after the start of simulation, very close to Run 3 which collapses into a BH at 6.31 ms. This run stopped soon after the formation of BH. As the masses of NSs are not equal to each other, the BH acquired a kick velocity, causing the crash in a similar scenario as Run 5.

Run 7: PPEOS- simple polytrope with $\gamma = 2$, $M_1 = 1.4$ and $M_2 = 1.4$

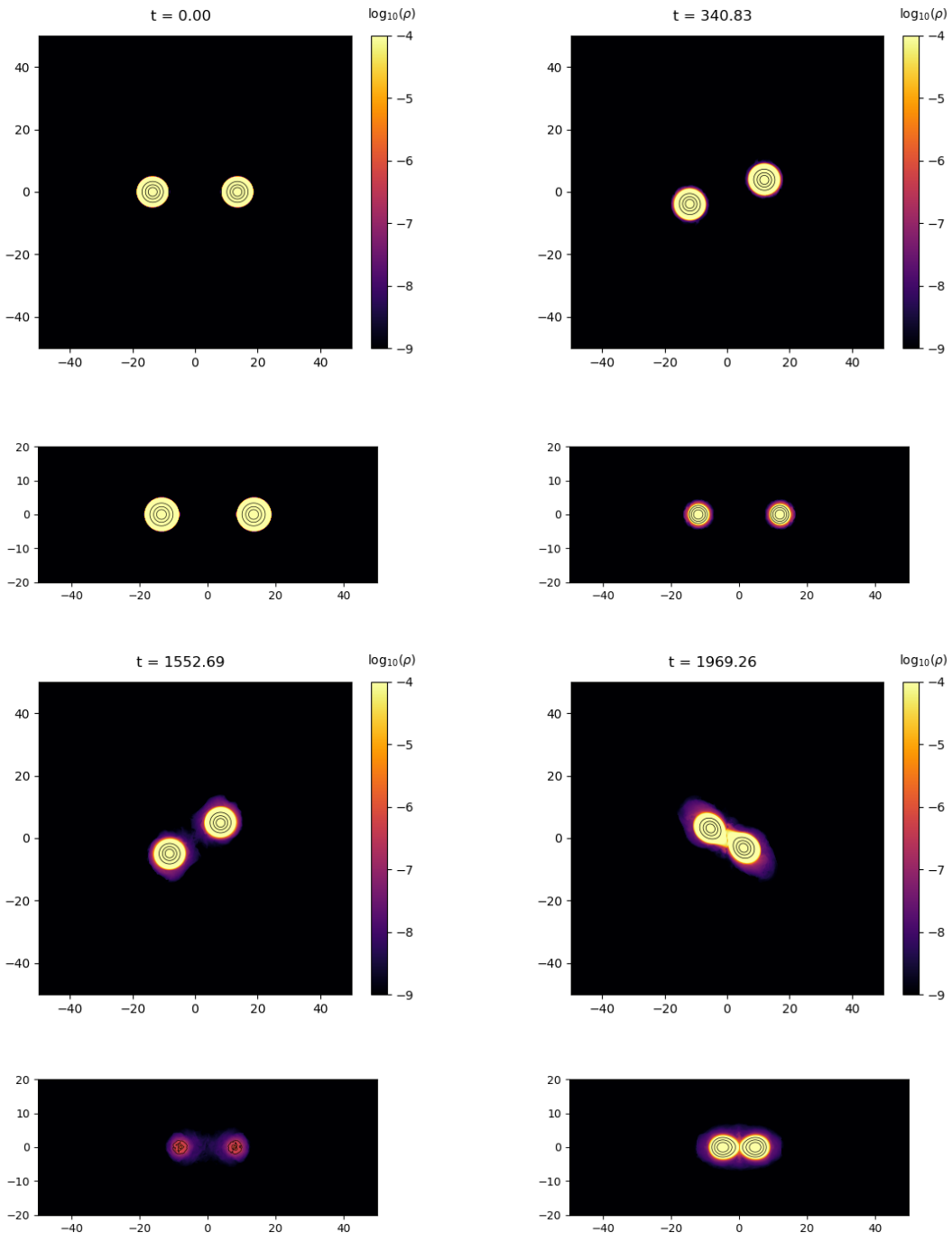

Run 7: PPEOS- simple polytrope with $\gamma = 2$, $M_1 = 1.4$ and $M_2 = 1.4$

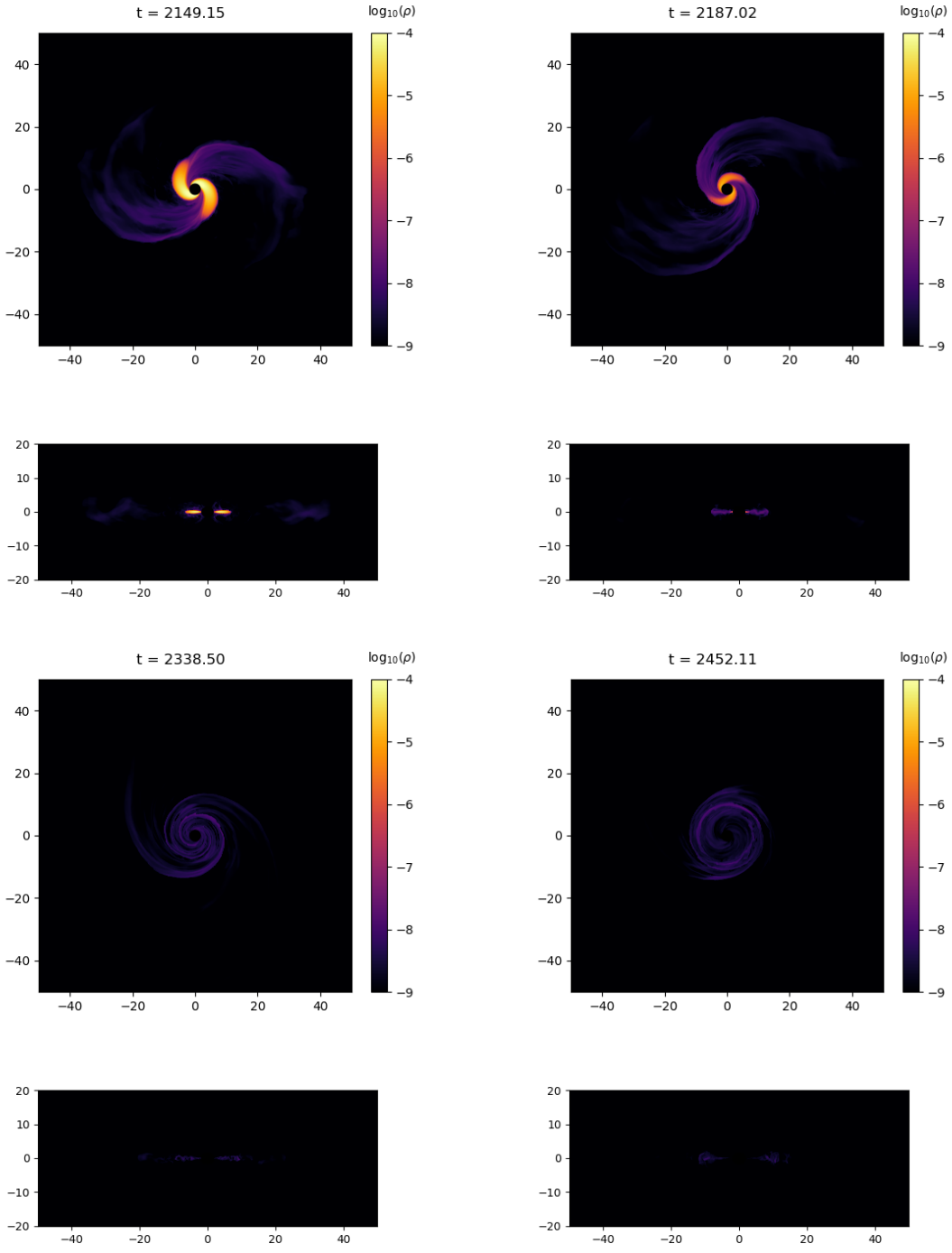

Figure 5.28: Evolution of density of BNS system with masses $1.4M_\odot$ each and simple polytropic EOS in the $x-y$ and $x-z$ directions. The merger remnant is a black hole formed at $t =$ 10.37ms .

Run 7: PPEOS- simple polytrope with $\gamma = 2$, $M_1 = 1.4$ and $M_2 = 1.4$

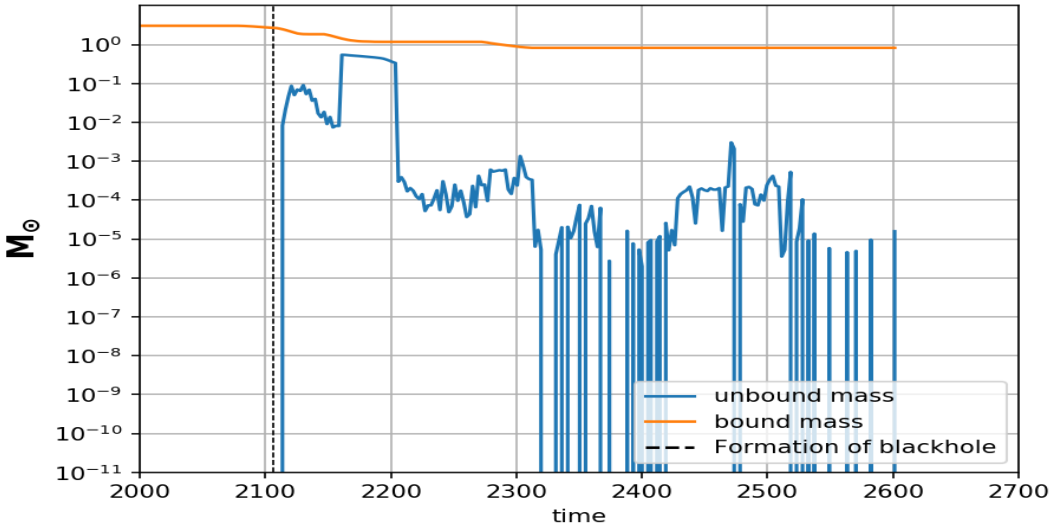

Figure 5.29: Evolution of bound and unbound mass for simple polytropic EOS with $\gamma = 2$ having masses 1.4 $M_\odot$ and 1.4 $M_\odot$.

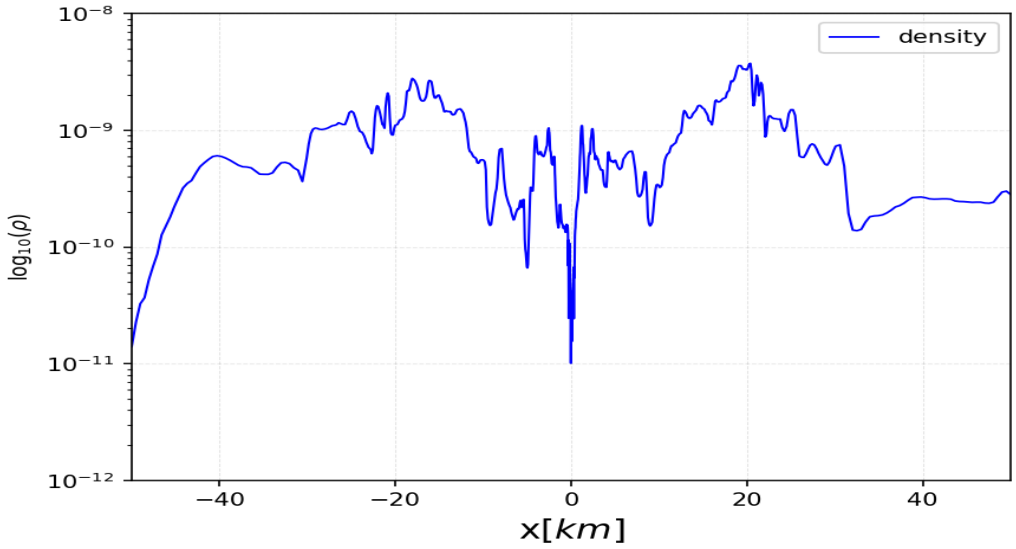

Figure 5.30: Density profile in x direction at $t = 2565.7196$ CU

Analysis of Run 7: PPEOS- simple polytrope with $\gamma = 2$, $M_1 = 1.4$ and $M_2 = 1.4$

1. The simulation begins from an initial separation of 40 km with a total mass of is $2.8M_{\odot}$ ans a mass ratio of unity. The evolution process is similar to the process of Run 1 as it is an equal-mass BNS system and the merger resembles a slow collision. The remnant of this run promptly collapses into a BH, as opposed to Run 1, where for similar mass configuration the remnant is a HMNS. Again, the difference in the EOSs of both the runs is responsible, since $\gamma - 2$ is relatively soft compared to most physically motivated models. The BH forms at 10.37 ms as compared to Run 4 with similar mass configuration (but SLY EOS) where the remnant collapses into a black hole at 9.25ms.

5.4.3 Binary neutron star merger remnant

We also conduct an analysis on how different initial properties of NSs affect the fate of the merger remnant. The result of a merger is inevitably a compact object, either a black hole or a neutron star. If the remnant is a neutron star, it can fall into one of the three categories:- supramassive neutron star, hypermassive neutron star, or stable neutron star, depending on whether and how the rotational state is necessary to prevent gravitational collapse. If the mass of the remnant is large enough, it will collapse into a black hole immediately. The table below consists of the list of the dynamical simulations we performed and the different parameters of the runs, along with the final merger remnant we observed.

We note that while we can and do see BHs forming as the result of many of our simulations, it remains extremely difficult to classify the eventual fate of what appears to be a HMNS that survives the the end of our numerical simulations. These configurations typically maintain strong rates of differential rotation, and will do so for timescales much longer than we can simulate. Our simulations do not include magnetic effects, which can facilitate the transfer of angular momentum from the remnant to its surroundings. Thus, we can only conclude that such remnants do not collapse *promptly*, nor have they collapsed *yet*; their final fate remains unknown to us given our available computational resources.

Run No.	M_1	M_2	EOS	Remnant	Time(ms)	Max unb mass
1	1.4	1.4	AP4	HMNS	29.8	NA
2	1.6	1.4	AP4	BH	7.69	0.1
3	1.8	1.4	AP4	BH	6.31	0.1
4	1.4	1.4	SLY	BH	9.25	0.1
5	1.6	1.4	SLY	BH	7.86	0.1
6	1.8	1.4	SLY	BH	6.26	0.1
7	1.4	1.4	$\gamma = 2$	BH	10.37	0.1*

Table 5.2: Different dynamical simulations performed with different parameters. The dynamical simulation run with AP4 EOS and M_1 =1.4 and M_2 = 1.4 was stopped at 29.8 ms and the merger remnant at t = 29.8 ms was a long lived HMNS. The last column includes the maximum amount of unbound mass left on the grid for each run. We could not get the unbound mass for Run 1 as we were able to capture the value only after a BH was formed and Run 1 was terminated before the HMNS could collapse into a BH. we recorded a slightly higher maximum unbound mass for Run 7, *although this could be due to numerical error and not a real physical effect as the resolution used for the run was not high enough.

5.5 Summary of Results

- The maximum amount of unbound mass left on the grid soon after the merger is approximately 10^{-1} $M_{\odot}$ for the grid structure and the resolution we have used in our simulations, except for Run 7, where more unbound material is seen left on the grid (Figure 5.28). This discrepancy can be explained as an artifact of the mass falling into the black hole, being calculated as unbound mass.
- A fraction of material from the NS is ejected in the form of unbound mass immediately after the remnant collapses to a black hole, an amount that eventually decreases as it leaves the numerical grid. We did not observe any unbound mass for Run 1, as the run was stopped before the remnant collapsed into a black hole.
- Run 5 and Run 6 stopped soon after the black hole formed. This seemingly occurred because the NS had unequal masses and the BH could acquire a non-trivial kick velocity. The investigation of the details of the crash is outside the scope of this dissertation and will be considered in future works.

Chapter 6

Conclusion

6.1 Conclusion

In this dissertation we investigated improving the quality of binary neutron star initial data and expanded the parameter space of publicly available binary neutron star quasi-equilibrium configurations, constructing several new models as part of our initial data library. We have also used the initial data from our library to launch dynamical simulations and investigate how different system parameters affect the amount of mass ejected versus the amount left on the grid over time, while classifying the fate of the merger remnant. We summarize our results below.

6.1.1 Update of `LORENE`

We have modified `LORENE` to build initial data for more unequal mass ratios and higher total masses using a secant method fix and routines that "scan" configuration through sequential steps in both mass and radius. We have released the data publicly on our website, so that they may be used to conduct dynamical simulations of BNS mergers using the Einstein Toolkit. With both the secant method fix and the mass and separation scanning routines in place, many of the problems that most users have encountered with Lorene have been resolved. These fixes allow for an easier use of Lorene along with an increased consistency for initial data runs.

6.1.2 Conservation of Hamiltonian constraints

We investigated different methods for improving the conservation of the Hamiltonian constraints, thus improving the quality and validity of initial data using `LORENE`. We can conclude the following regarding the conservation of Hamiltonian constraint:

- First, we were able to improve the quality of initial data for three different types of EOS by increasing the grid resolution, namely
  1. Simple polytrope
  2. Piecewise polytrope
  3. Tabulated EOS taken from [6]
- Second, we were not able to improve the initial data for the newer version of tabulated EOS given by [8].
- Third, we did not see any change in the conservation of the Hamiltonian constraint after increasing the number of domains or changing the convergence factor used by `LORENE`. This strongly suggests that these parameters do not play a significant role in the level of the numerical constraint violations, which are instead inherent to the multidomain spectral methods used by LORENE. These appear to be directly attributable to non-smooth behavior in the field solutions at the surface on one NS leading to non-smooth behavior in the factors multiplying the matter source terms for the elliptic equations centered on the other star.

6.1.3 Dynamical simulations and analysis of mass ejecta

We have performed dynamical simulations of BNS mergers using the initial data produced by our modified version of `LORENE`. Due to our radius scanning sequence, we were able to produce initial data at smaller separations (40km) than those previously generated, reducing the computational time required to see the onset of a merger. We summarize our results below.

- We can see from the evolution of the density (Figures 5.9 - 5.29) that the matter that bleeds off of the surfaces of the neutron star occurs at extremely low densities. Prior to merger, any and all ejecta is due to numerical effects, an artifact of the modeling of the

"atmospheres" required by conventional Eulerian hydrodynamic schemes. This effect is extremely small with regard to the total mass of the binary, and can largely be ignored. On the other hand, the mass loss during and immediately after the merger itself is a real physical effect caused by tidal interactions between the two stars.

- The amount of unbound mass produced in the simulations after the merger occurs increases as the mass ratio of the NS decreases ($q<1$). More unequal-mass mergers lead to more unbound material, since the lower-mass secondary is disrupted in a more violent fashion via interactions with the relatively heavier primary.
- A fraction of material from the NS is ejected in form of unbound mass immediately after the remnant collapses to a black hole and decreases eventually as it leaves the grid.
- The bound mass left on the grid eventually becomes constant in time and can be seen in form of a longer-lived accretion disk.
- The NS EOS affects the fate of the merger remnant and the amount of mass ejected during and after a merger. This is largely a consequence of the NS compactness depending on the EOS. The BNS merger remnant collapses faster when the mass ratio goes away from 1 ($q<1$).

6.2 Future Work

We will continue to work on expanding the initial data library and include more EOSs as well as better quality initial data. We will also continue to publish documentation addressing the following:

- How to use `LORENE` with a step-by-step sequence to produce stable initial data
- How to use `LORENE` to expand the parameter space for producing initial data
- How to use the initial data from our library to launch runs with the Einstein Toolkit.

Bibliography

[1] Duncan R. Lorimer. Binary and millisecond pulsars. *Living Reviews in Relativity*, 11(1), Nov 2008. (document), 2.2, 2.1

[2] K.S. Thorne. *The Future of Spacetime*, chapter Spacetime Warps and the Quantum World: Speculations about the Future. (document), 2.2

[3] Eric Gourgoulhon, Philippe Grandclément, Keisuke Taniguchi, Jean-Alain Marck, and Silvano Bonazzola. Quasiequilibrium sequences of synchronized and irrotational binary neutron stars in general relativity: Method and tests. *Physical Review D*, 63(6), Feb 2001. (document), 3, 3.1, 3.1, 3.5, A

[4] J. S. Read, B. D. Lackey, B. J. Owen, and J. L. Friedman. Constraints on a phenomenologically parametrized neutron-star equation of state. *Physical Review D*, 79(12), Jun 2009. (document), 3.2, 3.2.2, 3.2.2, 3.2, 3.3

[5] Sarmistha Banik, Matthias Hempel, and Debades Bandyopadhyay. New Hyperon Equations of State for Supernovae and Neutron Stars in Density-dependent Hadron Field Theory. *Astrophys. J. Suppl.*, 214(2):22, 2014. (document), 5.5

[6] Evan O'Connor and Christian D. Ott. A New Open-Source Code for Spherically-Symmetric Stellar Collapse to Neutron Stars and Black Holes. *Class. Quant. Grav.*, 27:114103, 2010. (document), 5.2, **??**, 5.5, 6.1.2

[7] James M. Lattimer and Douglas F. Swesty. A generalized equation of state for hot, dense matter. *Nucl. Phys. A*, 535(2):331–376, December 1991. (document), 5.6

[8] A. S. Schneider, L. F. Roberts, and C. D. Ott. Open-source nuclear equation of state framework based on the liquid-drop model with skyrme interaction. *Physical Review C*,

96(6), Dec 2017. (document), 5.2, **??**, 5.6, 6.1.2

[9] B. P. Abbott et al. Gw170817: Observation of gravitational waves from a binary neutron star inspiral. *Phys. Rev. Lett.*, 119:161101, Oct 2017. 1

[10] B. P. Abbott, R. Abbott, T. D. Abbott, F. Acernese, K. Ackley, C. Adams, T. Adams, P. Addesso, R. X. Adhikari, V. B. Adya, and et al. Gravitational waves and gamma-rays from a binary neutron star merger: Gw170817 and grb 170817a. *The Astrophysical Journal*, 848(2):L13, Oct 2017. 1, 2.3.2

[11] B. P. Abbott, R. Abbott, T. D. Abbott, F. Acernese, K. Ackley, C. Adams, T. Adams, P. Addesso, R. X. Adhikari, V. B. Adya, and et al. Search for post-merger gravitational waves from the remnant of the binary neutron star merger gw170817. *The Astrophysical Journal*, 851(1):L16, Dec 2017. 1

[12] B. P. et al Abbott. Gw170817: Observation of gravitational waves from a binary neutron star inspiral. *Phys. Rev. Lett.*, 119:161101, Oct 2017. 1

[13] B. P. et al. Abbott. Gw190425: Observation of a compact binary coalescence with total mass 3.4 m . *The Astrophysical Journal*, 892(1):L3, Mar 2020. 1

[14] P. C. Peters. *Gravitational Radiation and the Motion of Two Point Masses*. PhD thesis, Caltech, 1964. 1

[15] P. C. Peters and J. Mathews. Gravitational radiation from point masses in a keplerian orbit. *Phys. Rev.*, 131:435–440, Jul 1963. 1

[16] Stefano Gandolfi, Alexandros Gezerlis, and J. Carlson. Neutron matter from low to high density. *Annual Review of Nuclear and Particle Science*, 65(1):303–328, Oct 2015. 1

[17] J LATTIMER and M PRAKASH. Neutron star observations: Prognosis for equation of state constraints. *Physics Reports*, 442(1-6):109–165, Apr 2007. 1

[18] Silvano Bonazzola, Eric Gourgoulhon, and Jean-Alain Marck. Relativistic formalism to compute quasiequilibrium configurations of nonsynchronized neutron star binaries. *Physical Review D*, 56(12):7740–7749, Dec 1997. 1

[19] Christopher S. Kochanek. Coalescing Binary Neutron Stars. *ApJ*, 398:234, October 1992. 1

[20] Lars Bildsten and Curt Cutler. Tidal Interactions of Inspiraling Compact Binaries. *ApJ*, 400:175, November 1992. 1

[21] Masaru Shibata and Keisuke Taniguchi. Merger of binary neutron stars to a black hole: Disk mass, short gamma-ray bursts, and quasinormal mode ringing. *Physical Review D*, 73(6), Mar 2006. 1

[22] Kenta Hotokezaka, Kenta Kiuchi, Koutarou Kyutoku, Takayuki Muranushi, Yu-ichiro Sekiguchi, Masaru Shibata, and Keisuke Taniguchi. Remnant massive neutron stars of binary neutron star mergers: Evolution process and gravitational waveform. *Phys. Rev. D*, 88:044026, 2013. 1, 5.4.1

[23] Kenta Kiuchi, Yuichiro Sekiguchi, Masaru Shibata, and Keisuke Taniguchi. Long-term general relativistic simulation of binary neutron stars collapsing to a black hole. *Physical Review D*, 80(6), Sep 2009. 1

[24] J. M. Lattimer and M. Prakash. The physics of neutron stars. *Science*, 304(5670):536–542, Apr 2004. 2.1

[25] Richard C. Tolman. Static solutions of einstein's field equations for spheres of fluid. *Phys. Rev.*, 55:364–373, Feb 1939. 2.1, 2.1.2

[26] J. R. Oppenheimer and G. M. Volkoff. On massive neutron cores. *Phys. Rev.*, 55:374–381, Feb 1939. 2.1, 2.1.2

[27] B. K. Harrison, K. S. Thorne, M. Wakano, and J. A. Wheeler. *Gravitation Theory and Gravitational Collapse*. 1965. 2.1

[28] Ondrej Pejcha and Todd A. Thompson. The Landscape of the Neutrino Mechanism of Core-Collapse Supernovae: Neutron Star and Black Hole Mass Functions, Explosion Energies and Nickel Yields. *Astrophys. J.*, 801(2):90, 2015. 2.1.1

[29] Tuguldur Sukhbold, T. Ertl, S. E. Woosley, Justin M. Brown, and H. T. Janka. Core-Collapse Supernovae from 9 to 120 Solar Masses Based on Neutrino-powered Explosions. *Astrophys. J.*, 821(1):38, 2016. 2.1.1

[30] J. A. Pons, S. Reddy, M. Prakash, J. M. Lattimer, and J. A. Miralles. Evolution of proto–neutron stars. *The Astrophysical Journal*, 513(2):780–804, Mar 1999. 2.1.1

[31] R. N. Manchester, G. B. Hobbs, A. Teoh, and M. Hobbs. The Australia Telescope National Facility Pulsar Catalogue. *Astron. J.*, 129(4):1993–2006, April 2005. 1

[32] Mira Dey, Ignazio Bombaci, Jishnu Dey, Subharthi Ray, and B.C. Samanta. Strange stars with realistic quark vector interaction and phenomenological density-dependent scalar potential. *Physics Letters B*, 438(1-2):123–128, Oct 1998. 2.1.2

[33] D. Bhattacharya and E. P. J. van den Heuvel. Formation and evolution of binary and millisecond radio pulsars. *Phys. Rep.*, 203(1-2):1–124, January 1991. 2.2

[34] Paz Beniamini and Tsvi Piran. The Gravitational waves merger time distribution of binary neutron star systems. *MNRAS*, 487(4):4847–4854, August 2019. 2.2

[35] Jeff J. Andrews and Ilya Mandel. Double Neutron Star Populations and Formation Channels. *ApJ*, 880(1):L8, July 2019. 2.2

[36] S. E. Thorsett and Deepto Chakrabarty. Neutron star mass measurements. 1. Radio pulsars. *Astrophys. J.*, 512:288, 1999. 2.2

[37] David J. Nice, Eric M. Splaver, Ingrid H. Stairs, Oliver Loehmer, Axel Jessner, Michael Kramer, and James M. Cordes. A 2.1 solar mass pulsar measured by relativistic orbital decay. *Astrophys. J.*, 634:1242–1249, 2005. 2.2

[38] J. Aasi et al. Advanced LIGO. *Class. Quant. Grav.*, 32:074001, 2015. 2.3.2

[39] T. Accadia et al. Virgo: a laser interferometer to detect gravitational waves. *JINST*, 7:P03012, 2012. 2.3.2

[40] V. Ashley Villar et al. The Combined Ultraviolet, Optical, and Near-Infrared Light Curves of the Kilonova Associated with the Binary Neutron Star Merger GW170817: Unified Data Set, Analytic Models, and Physical Implications. *Astrophys. J. Lett.*, 851(1):L21, 2017. 2.3.2

[41] R. Chornock et al. The Electromagnetic Counterpart of the Binary Neutron Star Merger LIGO/VIRGO GW170817. IV. Detection of Near-infrared Signatures of r-process Nucleosynthesis with Gemini-South. *Astrophys. J. Lett.*, 848(2):L19, 2017. 2.3.2

[42] E. Pian et al. Spectroscopic identification of r-process nucleosynthesis in a double neutron star merger. *Nature*, 551:67–70, 2017. 2.3.2

[43] A. Goldstein et al. An Ordinary Short Gamma-Ray Burst with Extraordinary Implications: Fermi-GBM Detection of GRB 170817A. *Astrophys. J. Lett.*, 848(2):L14, 2017. 2.3.2

[44] David Eichler, Mario Livio, Tsvi Piran, and David N. Schramm. Nucleosynthesis, Neutrino Bursts and Gamma-Rays from Coalescing Neutron Stars. *Nature*, 340:126–128, 1989. 2.3.2

[45] Davide Lazzati. Short duration gamma-ray bursts and their outflows in light of gw170817. *Frontiers in Astronomy and Space Sciences*, 7, 2020. 2.3.2

[46] A. Perego, F. K. Thielemann, and G. Cescutti. r-process nucleosynthesis from compact binary mergers. In *Handbook of Gravitational Wave Astronomy*, pages 1–56. Springer Singapore, 2021. 2.3.2

[47] B.P. Abbott, R. Abbott, T.D. Abbott, S. Abraham, F. Acernese, K. Ackley, C. Adams, R.X. Adhikari, V.B. Adya, C. Affeldt, M. Agathos, K. Agatsuma, N. Aggarwal, and et al. Gwtc-1: A gravitational-wave transient catalog of compact binary mergers observed by ligo and virgo during the first and second observing runs. *Physical Review X*, 9(3), Sep 2019. **??**

[48] R. Abbott et al. Gwtc-2: Compact binary coalescences observed by ligo and virgo during the first half of the third observing run, 2020. **??**, **??**, **??**

[49] R. Abbott et al. GWTC-2.1: Deep Extended Catalog of Compact Binary Coalescences Observed by LIGO and Virgo During the First Half of the Third Observing Run. 8 2021. **??**

[50] R. Abbott et al. GWTC-3: Compact Binary Coalescences Observed by LIGO and Virgo During the Second Part of the Third Observing Run. 11 2021. **??**, **??**, **??**, **??**

[51] Richard Arnowitt, Stanley Deser, and Charles W. Misner. Republication of: The dynamics of general relativity. *General Relativity and Gravitation*, 40(9):1997–2027, Aug 2008. 2.4

[52] Andre Lichnerowicz. L'intégration des équations de la gravitation relativiste et le problème des n corps. *J. Math. Pures Appl. (9)*, 23:37–63, 1944. 2.4

[53] James W. York. Role of conformal three-geometry in the dynamics of gravitation. *Phys. Rev. Lett.*, 28:1082–1085, Apr 1972. 2.4

[54] Philippe Grandclément, Eric Gourgoulhon, and Silvano Bonazzola. Binary black holes in circular orbits. ii. numerical methods and first results. *Phys. Rev. D*, 65:044021, Jan 2002. 2.4

[55] A. Akmal, V. R. Pandharipande, and D. G. Ravenhall. Equation of state of nucleon matter and neutron star structure. *Phys. Rev. C*, 58:1804–1828, Sep 1998. 3.2.2, 5.4.1

[56] F. Douchin and P. Haensel. A unified equation of state of dense matter and neutron star structure. *Astronomy Astrophysics*, 380(1):151–167, Dec 2001. 3.2.2, 5.4.1

[57] Horst Müller and Brian D. Serot. Relativistic mean-field theory and the high-density nuclear equation of state. *Nuclear Physics A*, 606(3-4):508–537, Sep 1996. 3.2.2

[58] B. Friedman and V. R. Pandharipande. Hot and cold, nuclear and neutron matter. *Nucl. Phys. A*, 361:502–520, 1981. 4.2.1

[59] Thomas W. Baumgarte, Pedro J. Montero, Isabel Cordero-Carrión, and Ewald Müller. Numerical relativity in spherical polar coordinates: Evolution calculations with the bssn formulation. *Physical Review D*, 87(4), Feb 2013. 5.3.1

[60] Wolfgang Kastaun and Filippo Galeazzi. Properties of hypermassive neutron stars formed in mergers of spinning binaries. *Phys. Rev. D*, 91(6):064027, 2015. 5.4.1

[61] Zachariah B Etienne, Vasileios Paschalidis, Roland Haas, Philipp Mösta, and Stuart L Shapiro. Illinoisgrmhd: an open-source, user-friendly grmhd code for dynamical spacetimes. *Classical and Quantum Gravity*, 32(17):175009, Aug 2015. 5.4.1, 5.4.1

[62] Scott C. Noble, Charles F. Gammie, Jonathan C. McKinney, and Luca Del Zanna. Primitive variable solvers for conservative general relativistic magnetohydrodynamics. *The Astrophysical Journal*, 641(1):626–637, Apr 2006. 5.4.1, 5.4.1

Appendices

Appendix A

Mathematical Derivations

Taking equation 95 from [3]

$$\frac{d}{dX}(\nu + ln\Gamma) = \frac{d}{dX}(ln\Gamma_o) \tag{1.0.1}$$

$$\frac{d}{dX}(\xi + 0.5(ln|1 - \mu\lambda\Omega^2|)) = 0 \tag{1.0.2}$$

$$\xi'(1 - \mu\lambda\Omega^2) = 0.5(\mu'\lambda\Omega^2 + \mu\lambda'\Omega^2) \tag{1.0.3}$$

$$\xi' = 0.5(\mu'\lambda\Omega^2 + \mu\lambda'\Omega^2) + \mu\lambda\Omega^2\xi' \tag{1.0.4}$$

$$\frac{\xi'}{\frac{\Omega^2}{2}(\mu'\lambda + \mu\lambda') + \mu\lambda\xi'} = 1 \tag{1.0.5}$$

$$\frac{\xi'}{[\frac{1}{2}(\mu'\lambda + \mu\lambda') + \mu\lambda\xi']} = \Omega^2 \tag{1.0.6}$$

LORENE uses different variable names while calculating omega and are as follows:

$$\text{dnulg} = \frac{d}{dX}(\nu + ln\Gamma) = \xi \quad \text{asn2} = \frac{A^2}{N^2} = \mu \quad \text{dasn2} = \frac{d}{dX}\left[\frac{A^2}{N^2}\right] = \mu'$$

$$\text{bpb}_i = \frac{\lambda}{\Omega^2} \quad \text{cpc}_i = \frac{\lambda'}{2\Omega^2} \quad \text{andan}_i = (0.5\mu' + \mu\lambda') \tag{1.0.7}$$

Appendix B

Lorene parameter files and executables

B.1 Initial binary routine

The initial binary routine contained in the file init_bin.C sets up a superposition of two spherical NS, each with a specified EOS and central enthalpy, but does not account for the effects of the tidal interaction between them. All results published to date employ the same EOS model for both stars, as there is no compelling physical reason why it should be different for different NS.

The routine uses the following input parameter files:

- `par_eos1.d` and `par_eos2.d`: We can control the NS EOS using these two files. The typical `par_eos.d` files for the three different EOSs consist of the following input parameters:

  - **EOS: simple polytrope**

    Line 1: Type of EOS: Given by a number found at (`https://lorene.obspm.fr/Refguide/classLorene_1_1Eos.html`)

    Line 2: Star number → Specifies the star and takes either 1 or 2 as value

    Line 3: Adibatic index

    Line 4: This is the pressure coefficient k in $P = k\rho^\gamma$, measured in units such that $k = \frac{P}{\rho_{nuc}c^2}$, where $\rho_{nuc} = 1.66 \times 10^{14}\mathrm{g/cm}^2$ is Lorene's unit of nuclear density.

– **EOS: piecewise polytrope**

Line 1: Type of EOS: Given by a number found at (`https://lorene.obspm.fr/Refguide/classLorene_1_1Eos.html`)

Line 2: Star n ::- Specifies the star and takes either 1 or 2 as value

Line 3: N $\rightarrow$ Number of pieces of polytropes

Line 4 to N+3: Array of adiabatic index

Line N+4: Value of k at ρ_0 given in equation P = $k\rho^{\Gamma}$

Line N+5: $log(P_0)$

Line N+6 to 2N+4 =(N+6+(N-2)): array of the exponent of fiducial densities logRho

Line 2N+5 to 3N+3 =(2N+5+N-2) : array of percentage

– **EOS: Tabulated EOS**

Line 1: Type of EOS: Given by a number found at (`https://lorene.obspm.fr/Refguide/classLorene_1_1Eos.html`)

Line 2: Number representing the format of tabulated EOS 0 for standard format and 1 for CompOSE format

Line 3: Tabulated EoS Line 4: File path pointing to the tabulated EOS file

- `par_grid1.d` and `par_grid2.d`: These parameter files determine the size of the computational grid to be used by Lorene. The files are described as follows

Line 1: nz: total number of domains

Line 2: nzet: number of domains inside the star

Line 3: nt: number of points in theta (the same in each domain)

Line 4: np: number of points in phi (the same in each domain)

The next N number of lines specify the inner domain boundaries. We typically increase the radii in factors of 2. A typical `par_grid1.d` can be constructed as

5 nz: total number of domains

1 nzet: number of domains inside the star

17 nt: number of points in theta (the same in each domain)

16 np: number of points in phi (the same in each domain)

Number of points in r and (initial) inner boundary of each domain:

33 0. <- nr & min(r) in domain 0 (nucleus)

33 1. <- nr & min(r) in domain 1

33 2. <- nr & min(r) in domain 2

33 4. <- nr & min(r) in domain 2

33 8. <- nr & min(r) in domain 2

- `par_init.d`: This file contains information on both the stars such as central enthalpy and binary separation. The central enthalpy is given as log of enthalpy, $\log(h)$ as defined in Eq. 3.2.13. A typical `par_init.d` files consists of the following lines

  Line 1: factor defining the kind of computation, 1 for a relativistic computation, 0 for a Newtonian one

  Line 2: coordinate distance between the two stellar centers [km] for the initial setup

  Line 3: initial central enthalpy of star 1

  Line 4: rotational state of star 1 : 1 = irrotational, 0 = corotating

  Line 5: initial central enthalpy of star 2

  Line 6: rotational state of star 2 : 1 = irrotational, 0 = corotating

We use the parameter files to choose the mass and radius for the NSs. For polytropes, there is a scale freedom in the TOV equations, so as long as the central enthalpy remains fixed, varying kappa just changes the mass and radius linearly in relation to each other; for an EOS model with specified kappa values, the central enthalpy controls the mass and radius. In practice, We need to choose kappa properly to get the desired compactness for a given mass.

B.2 Coalescence routines

The routine found in `coal.C`, and various modifications we have made to it, reads in the binary configuration produced by `init_bin`, and iteratively applies the quasi-equilibrium field

equations to produce a relaxed configuration for two NS with specified EOS and baryon masses, at a specified binary separation as measured from the points of maximum enthalpy within the stars.

The coalescence routines make use of the EOS and grid files defined above, as well as the following:

- `parcoal_seq.d`: This file is used to run the coal_seq.d routine for different configurations. The main lines to change are the binary separation (`start_dist`), measured in km, number of steps for both the binary and mass separation, the amount of jump in the distance (`radius_step`), and the initial and final mass values for both stars. It consists of the following lines

  Line 1: File containing the initial conditions

  Line 2: start_dist : Factor by which the initial separation is multiplied at beginning (replaces fact_separ)

  Line 3: radius_step, step size used for the distance scanning sequence

  Line 4: nofsteps_radius, number of steps used in the distance scanning sequence

  Line 5: mbar_voulue_init[0], Initial Baryon mass required for star 1

  Line 6: mbar_voulue_init[1], Initial Baryon mass required for star 2

  Line 7: mbar_voulue_final[0], Final Baryon mass required for star 1

  Line 8: mbar_voulue_final[1], Final Baryon mass required for star 2

  Line 9: nofsteps_mass, Number of steps in which to let the baryon mass change

  Line 10: nmass_delay, how long after mer_masse steps to begin scanning mass

  Line 11: massscan_rstep, Radial step at which mass is scanned – from 1 to nofsteps_radius

  Line 12: mermax, Maximum number of steps in the main iteration

  Line 13: relax, Relaxation factor in the main iteration

  Line 14: mermax_eqb, Maximum number of steps in Etoile_bin::equilibrium

  Line 15: prompt, 1 if no pause during the computation

  Line 16: graph, 1 if graphical outputs during the computation

Line 17: seuil, Threshold on the enthalpy relative change for ending the computation

Line 18: fmer_stop, Step interval between pauses in the main iteration

Line 19: fmer_save, Step interval between safeguards of the whole configuration

Line 20: mermax_poisson, Maximum number of steps in Map_et :: poisson

Line 21: relax_poisson, Relaxation factor in Map_et::poisson

Line 22: mermax_potvit, Maximum number of steps in Map_radial::poisson_compact

Line 23: relax_potvit, Relaxation factor in Map_radial::poisson_compact

Line 24: mer_masse, Step from which the baryon mass is forced to converge

Line 25: aexp_masse, Exponent for the increase factor of the central enthalpy

Line 26: fmer_udp_met, Step interval between metric updates

Line 27: ind_rel_met, 1 if relaxation of the metric, 0 if not

Line 28: relax_met, Relaxation factor of the metric (used only if ind_rel_met=1)

Line 29: relax_omeg, Relaxation factor on Omega (orbital angular velocity)

Line 30: fact_omeg_min, fact_omeg_min * omega = low bound in the omega search

Line 31: fact_omeg_max, fact_omeg_max * omega = high bound in the omega search

Line 32: thres_adapt1, threshold on dH/dr for the adaptation of the mapping in star 1

Line 33: thres_adapt2, threshold on dH/dr for the adaptation of the mapping in star 2

Line 34: reduce_shift, factor by which the initial analytical shift is reduced

B.3 Executables

The following executables are required for running Lorene:- init_bin, coal/coal_seq_massscan. The initial code used for constructing the binaries is called init_bin.C and does the following steps

1. Reads the input values from par_eos and par_init.d
2. Maps each individual NSs onto the grid individually ready from par_grid.d
3. Constructs the binary, where the individual stars are placed at an initial distance
4. The binary configuration is saved to output files which are read by coalescence routine.

The second routine called as the coalescence routine is calculated using the code coal_seq_mass.C.

It conducts the following steps

1. Reading in all parameter values from the files mentioned above
2. Setting up 3-dimensional nested grid structures to describe each NS, and reading in the metric data from the `init_bin` routine.
3. A loop over gradually decreasing separations in which:
   (a) The binary separation (interpreted here as the offset between the centers of the two sets of domains) is reduced by a user-specified factor, typically 2.5 km.
   (b) The metric components from each star are re-interpolated into the domains of the other star
   (c) The typical `LORENE` relaxation step is computed, including calculation of the angular velocity and rotation axis, the computation of the enthalpy equation, and the determination of the new quasi-equilibrium state.
   (d) The change in central enthalpy of the NS is calculated, which is used as a stopping criterion for the loop.
4. Stellar data are saved *prior* to any increase in the stellar masses, as low-mass configurations are typically much more numerically stable than high-mass ones, especially when one changes the binary separation.